ABSTRACT

Title of dissertation: LASER ABLATION PROPULSION OF ASTEROIDS WITH A SUB-NANOSECOND PULSED LASER

Joshua Sloane
Doctor of Philosophy, 2019

Dissertation directed by: Associate Professor Raymond J. Sedwick
Department of Aerospace Engineering

With ablative laser propulsion, a laser is fired at a solid material. This material is converted to plasma and ejected from the material, generating thrust. This technology can be used to deflect an asteroid off of an Earth-impacting trajectory. Since the asteroid itself is used as the propellant, no additional propellant is needed for the deflection maneuver. Although laser propulsion has been proposed as a promising technology for asteroid mitigation in the literature, there has been relatively little experimental research on this application, specifically on ablation using pulsed lasers. In this thesis, ablative laser propulsion of asteroid analog materials using a pulsed laser is studied. A 1064 nm laser is used, with a 0.7 ns pulse width, 827 μJ per pulse, 40 kHz pulse repetition frequency, and 33 W average power. A time-of-flight mass spectrometer is used to characterize the plasma plume resulting from ablation of pyroxene rock. A 2D distribution of the ions is found as a function of speed and mass to charge ratio. From this, the specific impulse of the positive ions is found. The force over 500 ms of ablation is measured directly using a load

cell. Force measurements are conducted on aluminum, pyroxene, and high-fidelity simulants for CM, CR, and CI meteorites. The momentum coupling coefficient for the asteroid analogs was found to be several times greater than for aluminum. These samples are also weighed before and after ablation to determine the mass removal rate. The measured momentum coupling coefficient and mass removal rate are used to calculate the laser ablation efficiency and overall specific impulse of the ablation plume. As expected, the overall specific impulse is significantly lower than the specific impulse associated with the high-energy ions. The overall specific impulse of the meteorite simulants is even lower than for pyroxene, likely due to slow-moving large particles. Ablative laser propulsion was compared to a Hall thruster as an example electric propulsion technology. For a total thrust time greater than six months, laser ablation traded favorably, benefiting from not needing propellant aboard the spacecraft for the deflection maneuver.

LASER ABLATION PROPULSION OF ASTEROIDS WITH A SUB-NANOSECOND PULSED LASER

by

Joshua Sloane

Dissertation submitted to the Faculty of the Graduate School of the
University of Maryland, College Park in partial fulfillment
of the requirements for the degree of
Doctor of Philosophy
2019

Advisory Committee:
Professor Raymond J. Sedwick, Chair/Advisor
Professor David Akin
Professor Christine Hartzell
Professor Adil Hassam
Professor Kenneth Yu

Dedication

For my wife, Sonia.

Acknowledgments

This material is based upon work supported by the National Science Foundation Graduate Research Fellowship Program under Grant No. DGE 1322106. This research is also supported by the Air Force Office of Scientific Research (AFOSR) under Federal Award No. FA9550-16-1-0193. I would like to thank the Johns Hopkins University Applied Physics Laboratory for providing funding for my graduate education during my employment with the company.

I would like to thank my advisor Dr. Sedwick, without whom this thesis would not have been possible. Thank you for all of your guidance with my research, education, and career.

Thanks to my thesis committee: Drs. David Akin, Christine Hartzell, Adil Hassam, and Kenneth Yu. My knowledge of engineering and physics is built on the courses you taught me, so it is an honor to have you on my committee.

Thanks to my labmate Eric Smith, with whom I have worked on the laser ablation research since I started on the project. Thanks to the interns and students who have worked on this project with me. Thanks to all of my labmates at the Space Power and Propulsion Lab. They have always been there to help me with coursework, experiments, and most importantly have been great friends this whole time. Our lab's motto is "It builds character!," and I have never met another group of people with more character, hard-work, and determination.

Thanks to my family, who have supported me all my life. Whether I had an exam coming up, a broken experiment, or a late night writing a paper, they were

always there to help (and/or listen to me kvetch).

Last but not least, I would like to thank my wife, Sonia. I can't imagine how I would have managed to get through graduate school without her constant love and support.

Table of Contents

List of Tables

List of Figures

List of Abbreviations

AFOSR	Air Force Office of Scientific Research
ALP	Ablative Laser Propulsion
ARM	Asteroid Redirect Mission
BF_4	Tetrafluoroborate
COTS	Commercial Off-the-Shelf
CW	Continuous Wave
DART	Double Asteroid Redirection Test
DE-STAR	Directed Energy System for Targeting of Asteroids and exploRation
EMI	1-Ethyl-3-methylimidazolium
EMP	Electromagnetic Pulse
EP	Electric Propulsion
FPS	First Pulse Suppression
FWHM	Full Width at Half Maximum
LAMS	Laser Ablation Mass Spectrometer
LAP	Laser Ablation Propulsion
LAT	Laser Ablation Tug
LaWS	Navy Laser Weapon System
LITA	Laser-Driven In-Tube Accelerator
MIRACL	Mid-Infrared Advanced Chemical Laser
MOID	Minimum Orbit Intersection Distance
MS	Mass Spectrometer
NEA	Near Earth Asteroid
NED	Nuclear Explosive Device
NEO	Near Earth Object
NEOCam	Near Earth Object Camera
PHA	Potentially Hazardous Asteroid
PHO	Potentially Hazardous Object
PMT	Photomultiplier
RMS	Root Mean Square
SEM	Scanning Electron Microscope
SPPL	Space Power and Propulsion Laboratory
TOF	Time-of-Flight
TOF-MS	Time-of-Flight Mass Spectrometry/Spectrometer
TRL	Technology Readiness Level
UMD	University of Maryland

List of Symbols

C_m	Momentum coupling coefficient
C_p	Parasitic capacitance
d	Distance
D	Asteroid diameter; Distance
E	Energy
$\mathbf{E}$	Electric field
$\tilde{E}$	Particle energy-per-charge
f	Focal length of lens
f_i	Ablation plume ionization fraction
$f()$	Distribution function
F	Thrust force
g_0	Standard gravity on Earth ($9.81\ m \cdot s^{-1}$)
$g()$	Gaussian function
I	Current; constant of integration for MS
I_{sp}	Specific impulse
J	Jacobian determinant
ℓ	Distance from optimal focus along laser path
L	Length
N	Number of asteroids
m	Mass
$\dot{m}$	Mass flow rate; mass removal rate
$\tilde{m}$	mass-per-charge
M	Number of particles measured at the detector
P	Power
q	Particle charge
r	Laser radius at ℓ
R	Resistance; laser radius at lens
$R_\oplus$	Earth radius
t	Time
v	Velocity
V	Voltage
X, Y, Z	Coordinates of the sample position in the vacuum chamber
Y	Secondary electron yield
$\delta()$	Dirac Delta function
Δv	Change in velocity
Δx	Total deflection distance
η	Laser ablation efficiency; efficiency; non-dimensionalized particle E/q
η_0	Non-dimensionalized E/q of particles selected by TOF-MS
θ	Angle

τ	Total thrust time; time-of-flight
Φ	Laser fluence
Φ_{thresh}	Laser threshold fluence

Chapter 1: Introduction

1.1 Overview and Motivation

Asteroids pose a risk to Earth, with even a relatively small asteroid (> 10 m diameter) containing sufficient energy to cause local devastation. Fortunately, if an asteroid on an Earth-impacting trajectory is detected with sufficient lead time, a small change to its orbital velocity (∼1-10 cm/s) is sufficient to nudge the asteroid away from hitting Earth.

Ablative laser propulsion (ALP) is a promising technology for asteroid mitigation. With this technology, a laser is fired at a small spot on the asteroid. This converts the asteroid material from a solid directly to a plasma. The plasma plume is ejected from the asteroid, generating thrust. Since material from the asteroid itself is used as propellant, additional propellant is not needed for the deflection maneuver.

Despite the promise of ALP for asteroid mitigation, there has been relatively little experimental research in the literature on ALP of asteroid materials. The research which has been conducted typically uses continuous wave (CW) lasers, and analyzes only the ions in the ablation plume. With CW lasers, the laser heats and vaporizes the asteroid material, as opposed to ablating the material. For pulsed laser

ablation, the momentum-coupling-coefficient C_m (thrust-per-power) is dependent on the laser pulse width, fluence Φ (energy/laser spot area), and material properties of the target to be ablated. Using a pulsed laser delivers significantly higher peak laser intensity (power/area), and may have higher performance. Measuring the force directly is the most reliable method of determining propulsion parameters for ALP.

In this thesis, a 1064 nm laser is used, with a 0.7 ns pulse width, 40 kHz pulse repetition frequency, and 33 W average laser power. Pyroxene is ablated, and a time-of-flight mass spectrometer (TOF-MS) is used to characterize the two-dimensional distribution of the plasma ions as a function of both velocity and mass-per-charge. A deci-Newton load cell is also used to measure the force vs. time over 500 ms of ablation. In addition to pyroxene and aluminum, high-fidelity asteroid simulants are ablated for the direct force measurements, adding confidence that the results will be representative to real-world applications.

1.2 Outline of Dissertation

- In chapter 2, the background of ALP is discussed, including a literature review.
- In chapter 3, the design of a custom-built time-of-flight mass spectrometer (TOF-MS) is introduced. Using this design, the two-dimensional distribution of the ablation plasma as a function of both velocity and mass-per-charge can be found.
- In chapter 4, the TOF-MS hardware is tested. An ionic liquid ion source generates particles of known energy-per-charge, and is used to validate that

the TOF-MS design works as expected.

- In chapter 5, the TOF-MS is used to analyze the plasma plume resulting from pulsed laser ablation of pyroxene rock, a material common in asteroids. From this, the specific impulse of the ions in the ablation plume is found.

- In chapter 6, a load cell is used to measure the force due to ablation on several asteroid analog materials. This has the benefit of analyzing the entire ablation plume at once, rather than just the high-energy ions as is done by the TOF-MS. The mass flow rate is also measured, and the overall specific impulse is calculated. This is compared to the specific impulse of the high-energy ions.

- In chapter 7, the force measurements from the previous chapter are used for several high-level trade studies. The required force and thrust time needed to deflect an asteroid off of an Earth-impacting trajectory are calculated. In addition, the performance for asteroid mitigation of ALP is compared to a Hall thruster, which is a more traditional electric propulsion technology.

1.3 Contributions

A summary of the contributions of this dissertation are as follows:

1. A **time-of-flight mass spectrometer** (TOF-MS) has been designed, fabricated, and validated. This spectrometer is capable of characterizing a two-dimensional distribution of ablation plasma as a function of velocity and mass-per-charge.

2. The ions generated from **pulsed laser ablation** of pyroxene are analyzed using the TOF-MS to get the two-dimensional distribution. The average particle speed, weighted by the mass-per-charge, is calculated to find the **specific impulse** of the ions.

3. **Force due to ablation** of asteroid analogs, including **high-fidelity simulants**, is measured. A load cell is used to measure the force over 500 ms. This is used in conjunction with the measured **mass removal rate** to calculate the overall specific impulse of the ablation plume. This is then compared to the specific impulse of the high-energy ions found using the TOF-MS.

Chapter 2: Background and Literature Review

2.1 Asteroid Threat

Asteroids impact Earth on a daily basis. Most are small enough to either burn up in the atmosphere, or are as small as dust and slowly fall to the surface [1]. However, in Earth's history, larger asteroids are credited with local damage up to extinction-level events. Craters on the lunar surface, which are undisturbed by atmosphere or geological activity, also reveal the frequency of impact events. The cumulative distribution of the number of asteroids N as a function of the asteroid diameter D follows a power law, where $N(> D) \propto D^{-1.95}$ [2]. This means that larger asteroids impact Earth less frequently than smaller asteroids.

Even so, such large impacts have occurred in Earth's history. The Chicxulub asteroid had an estimated diameter of 5-81 km [3], roughly the size of New York City. This impacted Earth ∼65.5 million years ago, leading to a mass extinction event and the end of the dinosaurs [4]. More recently, Tunguska Russia was hit in 1908 with a ∼30 m asteroid, destroying 2000 km^2 of forested area. In 2013, Russia was again hit. The 17 m meteor detonated over Chelyabinsk [1], with energy more than 30x the Little Boy atomic bomb dropped on Hiroshima. Fortunately, the meteor entered Earth's atmosphere at a shallow angle, otherwise it could have

caused significantly more damage. This size asteroid is estimated to impact Earth at an average rate of once every 150 years or so. This shows that it is not a question of if a meteor will strike Earth again, but when, and what can be done about the threat.

One way of quantifying the risk of an impact event is with the Torino Scale. This categorizes risk on an integer scale from 0 to 10, with 10 being the highest risk (certain collision and global impact) [5]. Note that the Chelyabinsk impact is considered category 0 on this scale, despite the relatively large damage that could have been done. The Torino Scale is easy to understand, and intended for communication with the public. For communication within the scientific community, the Palermo Technical Impact Hazard Scale is commonly used [6]. This is a logarithmic scale, which is a function of the asteroid's kinetic energy, impact probability, and time until impact.

Advanced detection is required in order to respond to an impending asteroid impact. A near-Earth object (NEO) is any object (asteroid or comet) with a perihelion distance of less than 1.3 AU. Larger asteroids have a smaller absolute magnitude, making them easier to detect. In 2007, NASA set a goal of identifying all Potentially Hazardous Objects (PHOs), which are NEOs greater than 140 m in diameter, and whose minimum orbit intersection distance (MOID) with Earth is less than 0.05 AU [7].

Most of the asteroid discoveries have been made with ground based telescopes [8]. It is estimated that almost all NEOS with >1 km diameter have already been detected [9]. Once the 140 m goal is met, then most of the asteroids capable of

causing global or regional damage will be identified. However, this still leaves a gap of asteroids large enough to cause local damage (city scale), but small enough to be difficult to detect. Space based telescope could help close this gap. The Near-Earth Object Camera (NEOCam) is proposed to be stationed at the L1 Lagrange Point, allowing for a stable and cold environment, and can detect asteroids as small as 10 m in diameter [10].

According to the Center for Near Earth object Studies database as of January 2019, there are only three known asteroids with an absolute magnitude ≤ 20 (diameter $> \sim$300 m), with a nominal close approach to Earth closer than the lunar distance between the Earth and the moon (LD) before 2200 CE. Asteroid 99942 Apophis has the closest approach at 0.1 AU. This asteroid briefly set the record for the largest Torino scale rating of 4 for a potential impact in 2029 [11]. There was also the possibility of a 2036 impact. However, by 2013, both of these possible impact events have been ruled out [12]. With this ruled out, the chance of an asteroid impact large enough to cause global damage in the near future is low.

2.2 Asteroid Mitigation Techniques

The impulse required to deflect an asteroid off of an Earth impact is most strongly dependent on the asteroid mass (m), and the time (t) between when the impulse is applied and the close approach. Consider an instantaneous impulse applied at time t. For the simplest approximation, the change in velocity (Δv) required to deflect an asteroid by 1 Earth radius ($R_\oplus$) is

$$\Delta v \approx \frac{R_{\oplus}}{t} \approx \frac{20\ cm\ s^{-1}}{t\ [years]} \tag{2.1}$$

This highlights the importance of detecting an impending impact, and applying a deflection maneuver, as early as possible, to reduce the required Δv. Applying the Δv along the velocity vector of the asteroid has the added benefit of changing the period. This amplifies the total deflection by a factor of three [13], so

$$\Delta v \approx \frac{R_{\oplus}}{3t} \approx \frac{7\ cm\ s^{-1}}{t\ [years]} \tag{2.2}$$

The total impulse required is $m\Delta v$. For a spherical asteroid of constant density, the asteroid mass is proportional to the radius cubed.

Equation 2.2 provides a simple approximation, which is useful for preliminary mission planning and general analysis. Multiple studies in the literature have been conducted using high fidelity calculations of the required Δv. [14] minimized the required Δv for several asteroid orbit cases, modeled as an Earth-Sun 2-body problem. They found that the minimum Δv does not decrease monotonically with t, and has local minima when applied at perihelion. In [15], this work was built on to develop a mission design for several fictitious Earth-threatening asteroids. This analysis considered Earth perturbations and non-zero inclination orbits. [16] studied the problem of optimum control of asteroid deflection maneuvers, and considered both impulsive and continuous (i.e. low-thrust) deflection.

When an asteroid has a close approach with Earth, it may have a *resonant return*, where there will be another close approach years later due to orbital reso-

nance. In addition, there may be a *keyhole*, which is "a narrow linear slice of the uncertainty ellipse where the encounter can perturb the object onto a trajectory which returns for a later close approach" [17]. Since it cannot be predicted *a-priori* if an asteroid will fly through a keyhole, this can be a cause for concern. However, the Δv required to deflect an asteroid away from a keyhole can be significantly less than what is required to deflect by $R_{\oplus}$.

Once an asteroid on an Earth impacting trajectory is detected, it will still take a significant amount of time before a Δv maneuver can be applied. First, a spacecraft must be designed and launched, a process which typically takes at least 4 years. If the asteroid mitigation technology selected is at a low Technology Readiness Level (TRL), the development and testing of that technology can add to the total development time. If time permits, a precursor mission to the asteroid will be desired, to get a better understanding of the material properties, mass, shape, and orbit of the asteroid. Finally, the spacecraft must travel to the asteroid, which can take several years depending on the trajectory. Therefore, with current technology, we can assume a minimum of 5 years before the deflection maneuver can be applied. Depending on the risk of the asteroid, it is possible that the development time can be expedited somewhat. Research and development of asteroid mitigation technologies now, prior to the detection of an Earth threatening asteroid, will reduce development time for a mitigation mission should the need arise. Ideally, a planetary defense spacecraft can be assembled in advance, ready to be launched as needed, or even forward deployed in Earth orbit.

Figure 2.1 shows the different mitigation technologies available based on the

warning time and the diameter of the asteroid. Asteroids smaller than ∼10-25 m diameter are likely to burn up during atmospheric entry.

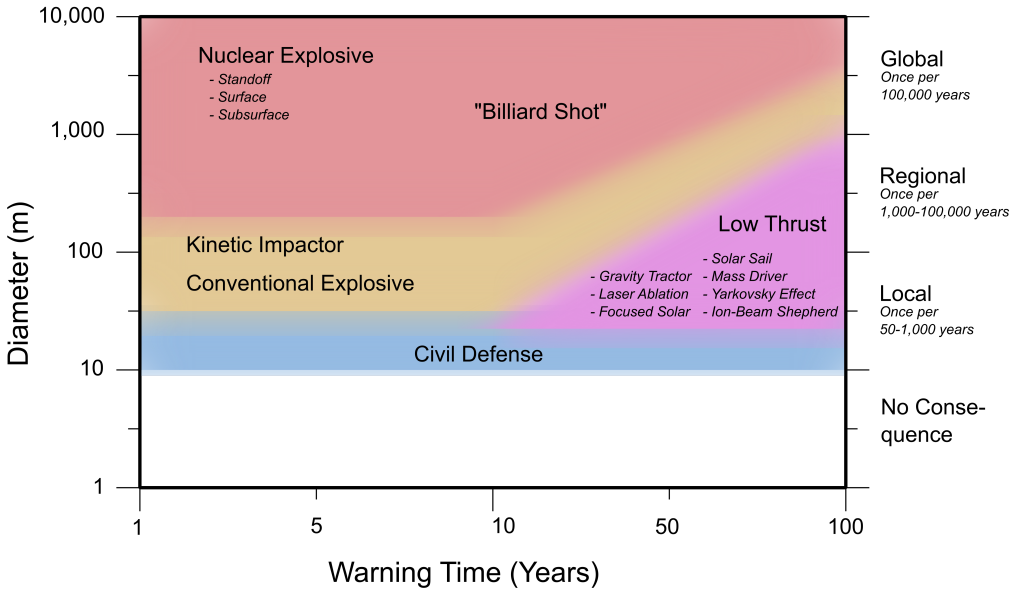

Figure 2.1: Asteroid mitigation technologies. Based on figures from [5, 18, 19].

For relatively small asteroids (∼10-50 m), civil defense measures may be sufficient. This includes warning the public, preparing evacuation, and constructing shelters. Since this size asteroid is difficult to detect, there may only be days or months of lead time, in which case civil defense is the only option. In addition, civil defense will be an important component of any asteroid mitigation plan [18]. The 2015 Planetary Defense Conference included an exercise focusing on a hypothetical asteroid impact scenario [20]. In this scenario, the uncertainty "risk corridor" starts as a long narrow band, driven by in-track uncertainty. As more observations are made, the uncertainty decreases, and the region likely to be effected becomes more clear. In this scenario, civil defense would be able to minimize loss of life due to an

impact event. Towns and cities along the risk corridor can be notified years in advance to begin making preparations and coordinate evacuation plans to neighboring regions not on the risk corridor. In the weeks leading up to the impact, the impact location will be fairly well-known, and the population can be evacuated.

For asteroids large enough to cause local devastation (∼50-500 m), the property damage from the asteroid, if it hits a city, can be multiple orders of magnitude greater than the cost of an asteroid redirection mission. In this case, the risk of impact must be traded with the cost and risk of a mitigation mission. Such a mission must be planned years in advance of the possible impact, at a time when there is still large uncertainty in the orbit. It likely will be unknown where on Earth the asteroid would impact, or if it is certain to impact at all. This may make it politically challenging to determine who would be responsible for funding and implementing such a mission. In addition, a failed redirection mission might deflect the asteroid to hit a different part of the Earth. Depending on the mitigation technique, if the asteroid is disrupted, there may still be several large chunks on a collision course, possibly more challenging to deal with than the initial asteroid. If the decision is made to pursue an active asteroid mitigation mission, there are several options to consider.

With the kinetic impactor technique, a spacecraft intercepts the asteroid at hyper-velocity speed, typically 10-30 km/s [21]. This imparts a significant amount of energy to the asteroid. Depending on the energy, as well as the asteroid's size and material properties, this may deflect or disrupt the asteroid. If the asteroid is disrupted, there is a risk that several large fragments may remain on a collision

course with Earth. The kinetic impactor is the most technologically mature mitigation technology [7]. Kinetic warheads used for ballistic missile defense make use of similar control algorithms. This was leveraged for the Deep Impact mission, where a spacecraft impacted a comet, and the resulting impact crater and particle ejection was measured [22]. An asteroid redirection mission will be more challenging, in part because the asteroid will be a smaller target. The upcoming NASA Double Asteroid Redirection Test (DART) mission will be the first demonstration mission of an asteroid mitigation technology. With this, the spacecraft will impact the smaller asteroid of a binary pair. This will result in a change to the orbital period of the pair, as well as a total Δv, measurable from Earth based telescopes [23].

For the largest asteroids, especially if there is little warning time, nuclear explosive devices (NEDs) are the most viable option. Even compared to kinetic impactors, NEDs have by far the highest energy density. One way of applying the energy is to have a standoff detonation, where the NED is detonated at some distance away from the asteroid. This can be done without needing to rendezvous with the asteroid, which would be required to place an NED on the surface. In addition, the chance of large fragments hitting Earth as a result of this detonation is relatively small [24]. The NASA report [7] assessed the standoff NED technique to be 10-100x more effective than the non-nuclear techniques considered. However, NEDs still have similar risks as kinetic impactors. It is difficult to predict the exact Δv in advance, there is only one shot (per spacecraft), and the resulting fragments may still pose a risk. In addition, NEDs face potential political challenges, both for implementing as well as testing in advance, and for posing a safety hazard if there

is a failure during launch.

One way to get energy comparable to an NED, without the safety or political ramifications, is with the "billiard-shot" concept. With this, a small asteroid is redirected to impact a larger asteroid. In [25], I conducted a hypothetical mission design based on this idea. In this mission design, a 10 m asteroid is captured and deflected using an ion engine onto a collision course with an Earth-threatening asteroid. Chemical rockets are used in the terminal guidance maneuver. Such an asteroid, impacting at 6 km/s, has a kinetic energy more than twice the yield of the TRINITY nuclear test [26]. [27] proposed a similar concept, except using a 230 kW laser to perform the deflection of a small 40 m asteroid to impact a larger asteroid.

If a sufficient lead time is available, and if the asteroid is not too large, low thrust deflection techniques can be used. Since thrust is applied over a long period of time, there is much more control of the trajectory compared to a single impact or explosion. There is also no risk of disrupting the asteroid. Some methods involve modifying the perturbing forces on the asteroid. For example, a portion of an asteroid can be painted to change its albedo, which amplifies the Yarkovsky effect [28]. Other techniques have an added benefit of not needing to directly contact an asteroid, simplifying operations. For example, a gravity tractor spacecraft is maintained in a station-keeping orbit near an asteroid, and the gravitational attraction pulls the asteroid towards the spacecraft. In the Asteroid Redirect Mission (ARM) (now canceled), the spacecraft first captures a boulder, dramatically increasing its mass and therefore the gravitational force, before performing a gravity tractor maneuver [29]. For the ion-beam shepherd method, an ion beam is directed at the asteroid, thereby

transferring momentum [30]. This requires the spacecraft to have a second thruster applying an equal and opposite force, to maintain the spacecraft's position.

Another contactless deflection technique is focused solar. For this, sunlight is focused onto a spot on the surface of the asteroid. This heats up material on the spot, causing it to vaporize. The vaporized material is ejected from the asteroid surface, generating thrust. By using the asteroid material itself as propellant, the spacecraft does not need to carry additional propellant for the deflection maneuver. Laser propulsion using a continuous wave (CW) laser operates in a similar manner [31]. Solar panels can be used to power the laser, or the laser diode can be pumped directly with sunlight. Nuclear power could also be used, allowing for a larger scale laser. If a pulsed laser is used, the asteroid material is ablated, and the asteroid material is converted directly from solid to plasma.

2.3 Ablative Laser Propulsion (ALP)

Ablative laser propulsion (ALP) is the process of removing material from the surface of a solid or fluid using a pulsed laser to generate thrust. With ALP, a fast, high-energy, and tightly focused pulse from the laser converts solid material directly into a plasma jet. Virtually any solid material can be used as a propellant, making laser ablation an ideal technology to be used for space propulsion.

Using continuous wave (CW) lasers, the laser is focused to a spot on a solid target, and held there for long enough for the spot to melt and then vaporize. The vapor is ejected from the solid, which imparts a small force on the solid. In a

seminal paper [32], Kantrowitz proposed using pulsed laser ablation as a propulsion mechanism, a concept feasible given the improvement in laser technology at the time. When the laser pulse has sufficient fluence Φ (energy/laser spot area), the laser-solid interaction operates in a different mode. In this case, the solid spot is ablated and converted directly to a plasma [33]. The plasma is ejected preferentially normal to the surface of the solid [34], and generates thrust. Lasers with femtosecond pulse width are achievable with modern technology [35].

Pulsed lasers have several advantages over CW lasers for thrust generation. A pulsed laser does not need to be pointed at a single spot for an extended period of time in order to generate thrust. In addition, individual pulses can be used for precise station-keeping maneuvers. Less of the laser energy heats up the surrounding solid, so there is less loss. For sub-nanosecond pulse times, the pulse duration is faster than the characteristic time of heat transfer [36], further reducing heat loss.

Of pivotal interest for space propulsion is the momentum coupling coefficient (C_m). C_m is the thrust from ablation divided by the laser power. This can also be thought as the impulse from ablation divided by the laser pulse energy. In general, C_m is dependent on the material being ablated, the pulse width, the wavelength, and the fluence [37]. For most systems, the fluence is easily modified, either by changing the focal spot size or the laser power. The threshold fluence Φ_{thresh} is the minimum fluence where plasma will be generated. The Sinko model predicts C_m in the plasma regime. Equation 14 from [38] is plotted in Figure 2.2, with the axes normalized. The parameter C for multiplicative energy losses from this equation is set to 1 in the plot. C_m is optimized when $\Phi \approx 4.2 \cdot \Phi_{thresh}$.

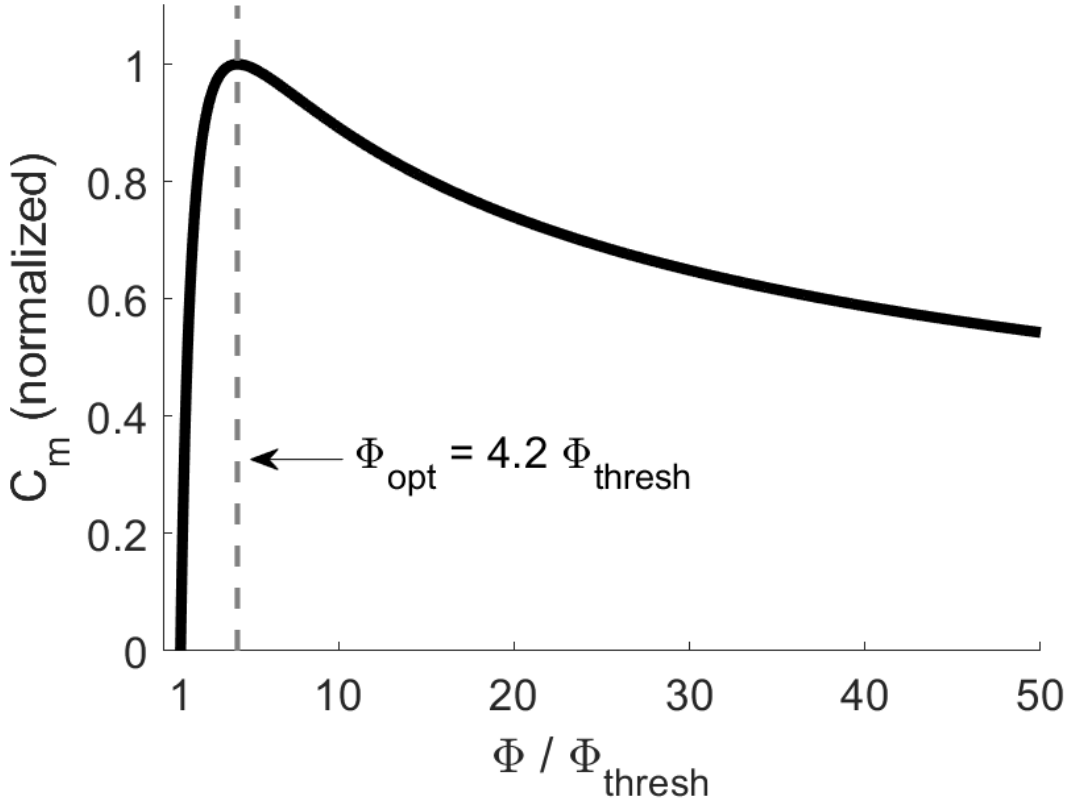

Figure 2.2: Sinko model for C_m from laser ablation in the plasma regime

Below Φ_{thresh}, ablation does not occur, and the material is instead vaporized. [38] includes a model which joins the vapor and plasma regimes, and that model is applicable over many orders of magnitude of fluence and pulse width. Increasing Φ above the optimum adds extra energy to the plasma. This increases the plasma plume's specific impulse (I_{sp}), at a cost of decreasing C_m, since the two are inversely proportional at constant efficiency. In many space propulsion applications, propellant is limited, and this trade is desirable. For asteroid deflection and orbital debris removal, however, the propellant mass is virtually limitless. This is because the object being moved is serving as the propellant, and there is no need to conserve

that propellant. The relation between C_m, Φ, and ablation efficiency η is discussed in more detail in chapter 6.

The most commonly tested materials for ablation targets are elemental metals. With elemental metals, only ions of a single element are present in the plasma, allowing for easier analysis of the fundamental physics taking place during the ablation process [39]. There has also been extensive research into engineered polymers designed for ablation propulsion [40]. The laser ablation efficiency η is defined as the kinetic energy of the ablation plume, divided by the laser energy. Polymers have been designed to include chemical energy which is released during ablation. With this additional energy, η can exceed unity.

Several spacecraft and propulsion designs have been proposed which use laser propulsion, spanning a wide range of power requirements. The lowest power application of ALP is for station-keeping of a spacecraft in orbit. This benefits from the small minimum impulse bit achievable from ALP when using a pulsed laser. A prototype of a micro-thruster has been developed, where a thin layer of material deposited on transparent tape is ablated using a ns-pulsed laser. The tape is on a reel, allowing for a fresh ablation spot for each pulse. This has a variable I_{sp} from 200 to 3600s [41], and a minimum impulse bit of 4E-5 $\mu N \cdot s$ [42].

In a laser-electromagnetic hybrid thruster, the ablation plume is further ionized and heated by an electrical discharge. The plume is then accelerated and directed by electric and magnetic fields [43], and an I_{sp} of 7200 s has been demonstrated [44].

ALP can also be used for larger Δv orbital maneuvers. One clear application is orbital debris removal. A spacecraft can be sent to de-spin and de-orbit large

orbital debris. Then, a small part of the satellite is broken off to use as propellant to go to the next debris target [45]. Therefore, the spacecraft does not need to bring additional propellant for these maneuvers.

In a laser-driven in-tube accelerator (LITA), a projectile (e.g. a small, sturdy spacecraft), is accelerated in a launch tube via laser ablation of propellant either on the projectile or in the launch tube [45, 46]. Research has mainly focused on achieving escape velocity on the ground, but it could also be used in space [46]. Another possibility is to accelerate a free-flying lightcraft to orbit using a ground-based laser. For this method, either the air below the lightcraft can be heated to produce a detonation wave [47], or material on the lightcraft can be ablated [48].

A feasibility study of a ground-based laser program ORION found that it would be able to remove all small orbital debris (1-10cm) in 2 years of operation, for a total cost of $100 million ($160 million in 2019 dollars) [49]. Recent research has looked into using a similar design to also de-orbit large objects (>10 cm), or move them to graveyard orbits [50]. Ground-based lasers must propagate in the atmosphere, and the nonlinearities associated with that provide their own challenges.

The Directed Energy System for Targeting of Asteroids and exploRation (DE-STAR) is a proposed space-based laser. At its largest scale, this system would be capable of completely evaporating a 500 m asteroid from 1 AU [51]. At smaller scales, DE-STAR would operate similar to a space-based ORION concept for orbital debris removal and asteroid mitigation. This system has also been proposed to propel wafer scale spacecraft to Alpha Centauri with 20 years of flight time [52]. Similar scale architectures have been proposed for space solar power. With these concepts,

solar power is collected with solar panels, and beamed to a collection point on Earth via directed energy (laser or microwave) [53, 54].

Multiple studies have been conducted for asteroid deflection missions using lasers or solar concentrators [27, 51, 55–57]. For example, the Laser Bees concept proposes using a small fleet of spacecraft, each equipped with a laser [58]. This has the benefit of being scalable, since the available solar power, as well as the laser size, may be limited for a single spacecraft. In addition, this concept has built-in redundancy.

There has been relatively little experimental research on ALP of asteroids. Gibbings uses a 90 W, 808 nm CW laser [59]. This was fired at olivine rock. The ejecta plume was monitored with a high speed camera, as well as with a spectrometer to infer the ablation plasma's temperature and speed. In addition, material from the plume was deposited on collection plates. This was analyzed to determine the contamination rate of the ablation plume on spacecraft laser optics and solar panels, as well as the plume's angular spread.

Lubin's laboratory has also conducted experiments on laser propulsion of asteroids. In [60], a 40 W, 808 nm CW laser is used. This was fired at basalt, and the force was measured using a torsion balance. The same laboratory also measured the mass ejection rate [51].

2.4 Space Weathering

Although laser ablation propulsion experiments on asteroid materials is not heavily researched, laser ablation is a common tool used in space weathering research. Space weathering is the effect that the space environment has on objects in space, such as planets, asteroids, and spacecraft. The largest contributors to space weathering are solar wind, solar radiation, and micrometeorite bombardment [61].

In the seminal 1955 paper [62], Gold asked the question of why the moon has two distinct surfaces: rocky surfaces and smooth darker surfaces. Gold posited that the smoother surfaces may be composed of dust, where micrometer bombardment caused erosion of the dust which caused it to be smoother, and mixing of the surface with micrometeors or solar radiation darkened the smoother region.

Experimental tests of these hypotheses were made possible by the 1969 Apollo 11 and subsequent lunar sample return missions. Initial analysis of these samples revealed that pulverized lunar rock has twice the albedo as lunar regolith of the same size [63]. The regolith is also redder than the pulverized rock [64]. Following this initial analysis, a significant number of experiments have been conducted testing the effects of simulated space weathering on lunar and asteroid materials or analogs to these materials [65–67].

For a typical sample preparation, rock is first ground with an agate mortar and pestle [66]. The powder is then sieved to the desired to the desired diameter, typically chosen between 2 μm [65] and 75 μm [68]. In some cases, the powder is tested loose. However, many experimenters find it convenient to press the powder

into thin pellets with a 1 cm diameter. This has the advantage of being able to easily mount the pellet in any orientation. However, this was found to decrease the amount of reddening that occurs from space weathering [63], so it is not a perfect analog.

One of the most commonly tested material is olivine [61, 65, 69, 70]. Other materials tested include lunar regolith simulant [61], SiO_2 [65], and pyroxene [68].

A common experiment on the powder samples is simulated micrometeorite bombardment. However, electrostatic dust accelerators require conductive materials which would contaminate optical measurements of reddening, and also cannot generate a sufficient amount of dust particles [68]. To simulate the effect of particle bombardment, instead pulsed lasers with comparable energy to high velocity (10 km/s) dust particles are used. The pulse duration is on the order of 10 ns, which is the same timescale that energy transfer from micrometeor bombardment occurs [68]. Techniques and lessons learned from space weathering experiments are applicable to the design of experiments for ALP of asteroids.

2.5 Directed Energy Weapons

For any ALP architecture to be successful, a high energy laser is required. For the laser to be deployed in space, it must be space-rated, vacuum compatible, high efficiency, and low mass. Laser technology has been developing rapidly in recent years, so ALP will be able to piggy-back on this development. One major application for high-energy lasers is directed energy weapons (DEW). These weapons

have similar requirements for low mass and high efficiency, so the technology will transfer well to ALP.

Perhaps the first example of a directed energy weapon in history is Archimedes' heat ray. A set of mirrors may have been used to focus the sun on Roman naval ships during the siege of Syracuse in 212 BCE, setting them ablaze. The existence and feasibility of this heat ray has been debated throughout history, with multiple attempts to replicate the weapon [71].

DEW is a common trope in science fiction, which is where most of the public is familiar with the concept. The Heat-Ray is a weapon in H.G. Wells' *The War of the Worlds*. Star Trek commonly uses DEWs such as particle beams and phasers. The most iconic DEW in science fiction is the Death Star in Star Wars. Although previously relegated to legend and fiction, DEW is now developing into a viable concept (albeit at a smaller scale than a Death Star).

The development of a DEW in modern history began with the development of the RADAR in the 1930's. Although RADAR uses directed energy to locate and track objects, as opposed to causing damage, it is a similar concept [72]. The full power of energy weapons was understood as a result of nuclear missile testing. During tests in 1963, it was discovered that the electromagnetic pulse (EMP) from a nuclear detonation can damage electrical components. Years later, it was realized that such an EMP, if detonated in the high atmosphere, could shut down the United States power grid, as well as communications [73].

Although DEW has faced some technical challenges during development since this time, the advantages are clear. DEW provides near instantaneous transmission

time. For missile defense, this is critical for applications such as destroying an incoming missile during boost phase. The cost-per-shot of the LaWS DEW is less than one dollar [74]. There is a virtually unlimited magazine, as the number of shots is only limited by the power available. This would turn the tables on asymmetric threats, such as a fleet of unmanned aerial vehicles, which would overwhelm current defense technologies. Precision targeting and variable lethality significantly add to the operational use of such weapons.

High energy laser weapons are a subset of DEWs, and of particular interest to this thesis. The Mid-Infrared Advanced Chemical Laser (MIRACL), first tested in 1980, was the first MW class continuous wave laser, designed for missile defense. In 1992, the Alpha laser demonstrated comparable power levels, but in a low-pressure environment, demonstrating that it can be suitable in space [75]. The Navy Laser Weapon System (LaWS) is a 33 kW laser, tested on USS Ponce in 2014 [76]. LaWS will also be installed on the guided missile destroyer USS Arleigh Burke in 2020 [77].

2.6 Time-of-Flight Mass Spectrometry (TOF-MS)

A time-of-flight mass spectrometer (TOF-MS) is particularly well suited for measuring the plasma plume resulting from pulsed laser ablation. A single laser pulse is fired, which simultaneously generates the ablation plasma, as well as marks the start of the time-of-flight (TOF). The particles travel a known distance, and are detected at the end of the mass spectrometer (MS). Based on the distance traveled and the flight time, the particle speed is determined. Typically, the particles will

also pass through electric or magnetic fields. Based on how the charged particles are deflected, their energy-per-charge can be determined. Combining the velocity and energy-per-charge measurements, the mass-per-charge of the particles is found.

There are several configuration designs for a TOF-MS. One of the most commonly used design configurations for a TOF-MS is a reflectron. In this design, the ions are first generated, then travel through a field-free drift region. They then enter into an ion reflector, which is an electrostatic grid that reflects the ions by approximately 180°. The ions then travel back through the field-free region until they reach the detector, located near the original ion source. Ions with higher mass-per-charge travel deeper into the reflector. As a result, all ions with the same mass-per-charge reach the detector at the same time, regardless of their initial speed, so the detector signal vs. time can be directly converted to a mass-per-charge distribution. This has a very high mass resolution, making it a popular technique [78]. However, this technique does not give a speed distribution for the ablation plasma. While this is not needed if one is only interested in the elemental distribution of a material, it is a critical measurement for ALP. In addition, since the ions must be completely turned around by the reflector, the maximum measurable ion energy is less than the voltage of the reflecting grid.

Another design is an orthogonal acceleration TOF-MS. With this design, the ions are accelerated orthogonally to their initial direction of motion by an electric field. Because the acceleration is orthogonal, the in-line velocity component is not modified, so the ion velocity can still be measured. The total deflection is dependent on the ion energy-per-charge ratio. Therefore, the location for where the ion hits

the detector at the end of the TOF-MS determines its energy-per-charge. Typically, a microchannel plate detector is used, since it provides both a spatial and temporal measurement of the detection [79]. Microchannel plates must be stored in vacuum, which can add to complexity of their operational use.

Another method of detecting ions is the Daly detector, first proposed in [80]. Ions enter into this detector, and then are accelerated by a high voltage. They then impact an aluminum plate, releasing secondary electrons. Following that, the secondary electrons are accelerated into scintillator. When the electrons impact the scintillator, it emits photons. These photons then are amplified by a photomultiplier. This device is a relatively simple design, but capable of measuring very small currents.

For many applications, the material properties of a sample are unknown, and the TOF-MS is used to determine the elemental distribution. In this case, laser ablation is a tool to assist with this measurement, rather than the physical process of interest. One application like this of particular relevance to ALP of asteroids is the use of TOF-MS on space missions to conduct *in-situ* spectrometry measurements. Although the application is different, this still a laser used in a space environment, and fired at a rocky surface. In addition, the plasma plume must travel in a vacuum, which is naturally present in many space environments, and also allows for a spacecraft to make the measurement without needing to contact the asteroid directly. The Laser Ablation Mass Spectrometer (LAMS) has been designed for such missions [81]. Experimental results from this device, including the effect of the shot number on the element distribution, as well as the ion energy, are directly applicable

to asteroid redirection applications of laser ablation.

TOF-MS is also a popular technique for studying the physical processes associated with laser ablation. It can be used to quantify the effect of repeated ablation shots on the resulting plasma, and can analyze multiple ion species simultaneously [39]. It has also been used to study the effect of pulse width on the plasma plume [82]. It has also been used to characterize the ions in laser propulsion experiments, and to determine the specific impulse [44].

2.7 Force Measurements

Knowledge of the force generated from laser ablation is critical to plan asteroid deflection missions. The momentum coupling coefficient C_m is typically reported, defined as the force from ablation divided by the laser power.

The ablation plume can be analyzed to indirectly determine C_m. C_m can be calculated using the mass removal rate $\dot{m}$ and specific impulse I_{sp}. $\dot{m}$ is relatively straightforward to measure. A sample is ablated for a known amount of time, and weighted before and after the ablation event to get the change in mass. An alternative method is to analyze the crater from an ablation event with a scanning electron microscope (SEM), and estimate the volume of the crater.

The speed of the high-energy ions can be found using a time-of-flight measurement, as described in the previous section. The plume expansion can also been observed using a high-speed camera [83]. Finally, the plume temperature can be measured based on its emission spectrum, and the particle speed estimated from

that [31]. However, these techniques all measure the speed of only the energetic ions, and not slower moving neutrals, or larger particles. As discussed in [84], this can significantly over-estimate the overall specific impulse. Therefore, a direct measurement of the force is preferable, since it does not have this issue.

[85] discusses the recommended practices for measuring thrust from electric propulsion (EP) systems. In most cases, the force generated from EP is much less than the weight of the system, making the use of a load cell impractical. Instead, it is recommended to use a thrust stand, as either a torsional, hanging, or inverted pendulum. The equations of motion of these thrust stands are that of a spring-mass-damper system. The deflection of a pendulum can be measured with a laser interferometer, capacitive sensor, or similar sensor. For most EP systems, the steady-state deflection of the pendulum is found, which gives the average thrust.

There are some unique aspects of ALP which must be considered when making thrust measurements. Repeated ablation to the same spot on a material results in a degraded force response, making steady state measurements of force challenging. Also, the sample material being ablated can be attached to the force pendulum, while the heavy laser can be mounted external to the pendulum. Because of this, the impulse response of a pendulum to a laser pulse is often measured (as done in [86]), rather than a steady-state deflection. The pulse width of the laser should be significantly shorter than the pendulum's period, otherwise additional effort will be needed to account for a time-varying fluence. This requires a sufficiently high impulse from a single laser pulse to be detectable by the thrust pendulum.

Because the laser does not need to be physically attached to the material being

ablated, the issue of low thrust per weight associated with EP systems is significantly reduced. This allows for the use of a load cell to measure the force. In chapter 6, ALP experiments using a load cell are discussed.

Chapter 3: Design of a Time-of-Flight Mass Spectrometer for Characterization of Laser Ablation Plasma

Sloane, J., "Design of a time-of-flight mass spectrometer for characterization of laser ablation plasma," 2016.

The following chapter has not previously been published. This chapter was previously submitted to the University of Maryland Department of Aerospace Engineering in partial fulfillment of the requirements for the degree of Masters of Science.

3.1 Abstract

Laser ablation is a method of generating low-thrust propulsion in space. In addition, the ablation plasma contains particles ranging in size from individual ions to nanoparticles, which can be used in plume impingement studies to simulate the space environment. In this paper, the design and construction of a time-of-flight mass spectrometer (TOF-MS) to characterize a laser ablation plasma is discussed.

3.2 Nomenclature

η	Non-dimensionalized particle energy-to-charge ratio
η_0	Non-dimensionalized energy-per-charge of a particle which passes through the energy gate initially moving in the x-axis
θ	Entry angle of a particle to the energy gates
v_0	A particle's initial velocity
τ	Time for a particle to traverse the first energy gate
D	Distance between the ground and deflection plates in the energy gate
d	Distance in the y-axis between the entry and exit aperture
d_{accel}	Distance between the accelerator plates
$d_{aperture}$	Gate aperture diameter
$d_{detector}$	Distance in the x-axis between the start and the end of the detector
E	Particle energy
$\mathbf{E}$	Average electric field in the energy gate
$\boldsymbol{E_{cap}}$	Electric field in a parallel plate capacitor
LAT	Laser Ablation Tug
$L_{detector}$	Distance in the y-axis between the secondary particle release and the scintillator in the detector
$L_{field-free}$	Length of the field-free region
L_{plate}	Length of the ground and deflection plates in the energy gate

m	Particle mass
PMT	Photomultiplier
q	Particle charge
t_d	Time that the primary particle spends in the accelerator grids and detector
t_f	Time when oscilloscope measures detection
t_{pulse}	Laser pulse time
t_s	Secondary particle flight time
t_{TOF}	Time-of-flight
t_0	Time when ablation occurs
TOF-MS	Time-of-Flight Mass Spectrometer
V	Voltage on energy grid deflection plates

3.3 Introduction

One of the most ubiquitous challenges in aerospace engineering is "the tyranny of the rocket equation" [87]. A consequence of the Tsiolovsky rocket equation, this states that the mass ratio between the vehicle's dry mass and total mass is exponentially dependent on the delta-v which is to be performed. Typically, all of a vehicle's propellant to be used during a mission must is included in the initial launch from Earth, so additional propellant is needed get this to Earth orbit. If propellant can be instead harvested *in-situ* while in space, the spacecraft's launch mass can be decreased, and the mission life can be extended.

First proposed by Kantrowitz in 1972 [32], laser propulsion is the process of removing material from the surface of a solid or fluid using a laser to generate thrust. With laser ablation propulsion, a fast, high-energy, and tightly focused pulse from the laser converts solid material directly into a plasma jet. Virtually any solid material can be used as a propellant, making laser ablation an ideal technology to be used for space propulsion. For example, a Laser Ablation Tug (LAT) is a proposed mission design for orbital debris removal [45]. In this design, the orbital debris itself is used as the propellant for ablation, allowing the tug to deorbit multiple debris objects without needing to bring additional propellant with it during launch. Laser propulsion has also been proposed for asteroid mitigation [49, 51].

Another application of laser ablation is its ability to generate energetic particles. Other research currently being conducted in the Space Power and Propulsion Lab uses a Xenon and Argon ion source to analyze the effect of particle bombard-

ment on spacecraft [88]. The laser ablation facility extends this capability, since the particles range in size from individual ions to nanoparticles.

For both applications, it is critical to have a well-characterized ablation plume. Heavier particles moving at lower speeds correspond to a decrease of specific impulse [89]. A mass and velocity distribution can be integrated to determine the force generated due to ablation. In addition, the distribution can be used to determine the inefficiencies associated with polydispersity, which is when the particles in an exhaust stream are at different speeds [90]. For plume impingement studies, knowledge of the impacting particles is important to determine that they are properly simulating the desired conditions.

In this paper, the design of a Time-of-Flight Mass Spectrometer (TOF-MS) is discussed, which will be used to characterize an ablation plume's velocity, mass, and charge distributions. TOF-MS is well suited for laser ablation spectrometry, since the fast ablation pulse marks the start of the TOF measurement, so no additional gating is needed, and the ablation plume is already directional. TOF-MS is a relatively low-budget spectrometry technique, and does not require breaking vacuum to conduct measurements.

3.4 Hardware

The facility is composed of a laser, an optics enclosure, a vacuum chamber where laser ablation occurs, and a spectrometer to characterize the ablation plume. Figure 3.1 shows a schematic of the hardware, and Figure 3.2 shows a picture of the

facility.

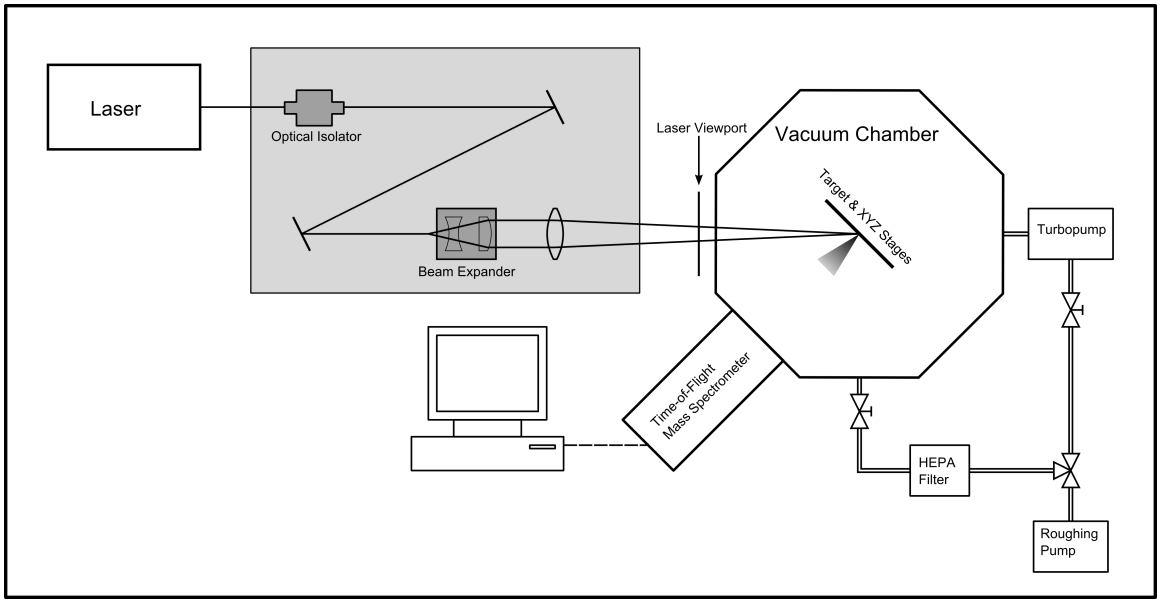

Figure 3.1: Schematic of hardware.

Figure 3.2: Laser ablation facility.

The laser first enters the optics enclosure. An optical isolator prevents reflected laser light from damaging the laser. Following two mirrors, the laser is expanded

and then focused to a small spot via a 20x beam expander and 3" lens with 0.5 m focal length. This allows the laser beam to enter the vacuum chamber through the laser viewport at a large diameter, with the focal spot near the center of the chamber. The chamber is large enough for the laser to be sufficiently diffuse by the time it reaches the chamber walls for it to be absorbed as heat, without damaging the walls.

An interlock is wired to the laser, so it can only fire when the optics enclosure and chamber are sealed. Using this interlock, the laser facility is considered to be Class I, allowing for use without additional eyewear or other laser safety equipment.

A turbo pump backed by a dry roots pump maintains the chamber pressure below 1e-4 mbar. A pair of ball valves allows the turbo pump to be switched for a HEPA filter in the pump line. The HEPA filter is used at the beginning of pumpdown and while bringing the chamber back to atmosphere in order to collect nanoparticles generated during ablation.

The laser is a Q-Switched Nd-Y2SO4 from Photonics Industries (model SN-40-1064). It emits pulses of about 0.7 ns (FWHM) duration and up to 827 μJ pulse energy at a wavelength of 1064 nm. The pulse repetition rate can be varied from 40 kHz to 90 kHz and the average power from 0 to about 36 W. Using the laser's external gating control, an individual pulse, or a train of pulses at the pulse repetition rate, can be picked out. A light sensitive diode in the optics enclosure detects stray light from the laser to determine when a laser pulse occurs. This diode is monitored by a high-speed oscilloscope, which is connected to a computer for data capture.

A target plate to be ablated is placed at the laser focal spot. The target is oriented so the normal of its plane is at a 45° angle with respect to the incoming laser. The ablation plume is a directed plume, which moves in the direction normal to the surface of the target, and has a cosine dependence [89]. A custom built mass spectrometer is aligned with the ablation plume. Multiple laser pulses at the same spot would drill into the target, which creates a nozzle directing the plume back towards the laser [91]. This is undesirable, since the plume would be directed away from the spectrometer, and towards the laser viewport which could be damaged by the plume. In addition, repeated pulses to the same spot degrade the ablation response [89]. In order to maintain a fresh ablation spot, the target is attached to XYZ translational stages. The stages are also used to fine tune the focus of the laser.

3.5 Mass Spectrometer

3.5.1 Overview

A time-of-flight mass spectrometer (TOF-MS) is used to characterize the velocity, charge, and mass of the particles in the ablation plume. Since the spectrometry is being performed in vacuum, and the particles range from individual ions to nanoparticles, a custom spectrometer was designed. A schematic of the mass spectrometer is shown in Figure 3.3. The ablation plume is generated at the target from a single laser pulse. The spectrometry measurement begins with a single laser pulse, which generates ablation and marks the start of the TOF. After traversing through

a field-free region, the particles reach the energy gates, which filter particles by their energy-to-charge ratio (E/q).

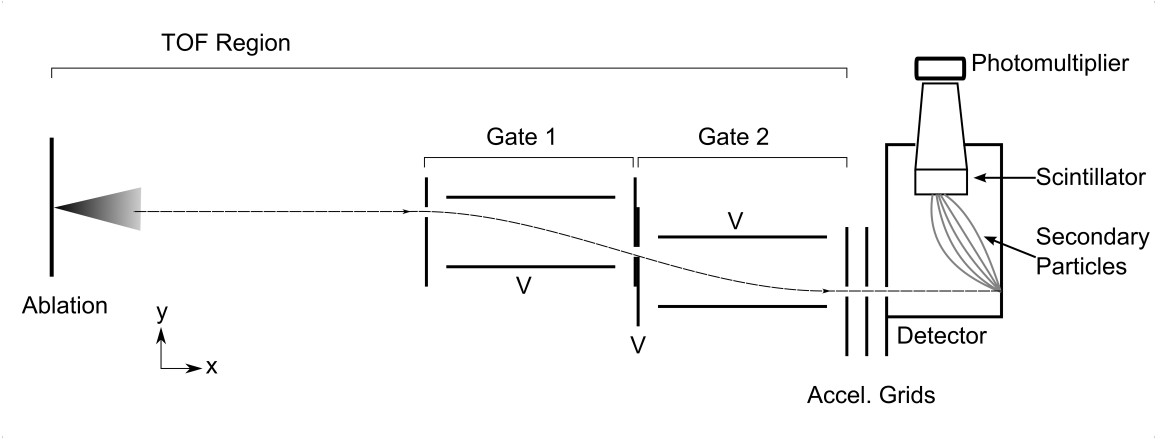

Figure 3.3: Schematic of mass spectrometer.

A particle of the correct E/q is then accelerated and collides with the back wall of the detector, releasing secondary particles. The number of secondary particles released is a function of the energy of the primary ablation particle. The secondary particles are accelerated to the scintillator, which generates light when it collides. This signal is amplified by the photomultiplier, which is in turn measured by the oscilloscope. The time between the ablation pulse occurring and the photomultiplier signal corresponds to the time of flight of a particle.

Since the distance between the ablation spot is known, the particle velocity v can be calculated using the TOF measurement. The particle's E/q is known from the energy gates. Finally, the particle's energy is determined from the number of secondary particles emitted. From $E = \frac{1}{2}mv^2$, the mass and charge of the particle are determined.

3.5.2 Magnetic Shielding

In order to minimize the effect of the Earth's magnetic field on the particle motion, the mass spectrometer is placed in a high permeability cylindrical magnetic mu-shield. The ends of the cylinder have removable caps to allow access to inside the cylinder from both sides. The cap in the chamber side of the magnetic shield has an aperture to allow particles to travel through without significantly degrading the shielding from the magnetic field. There is also a hole in the mu-shield for a high-voltage feedthrough port, and a hole for wires to go into the chamber.

The magnetic shield is a cylinder with a 7.6 in outer diameter, and 21.1 in length, selected to fit inside the chamber extension. This provides a constraint on the size of the spectrometer, which must fit inside this cylinder. The thickness of the shield was selected to be 0.062 in to ensure that the magnetic field is less than 1% of the Earth's ambient magnetic field. The effectiveness of the shielding was verified using a simulation conducted with COMSOL Multiphysics v4.4, and with a magnetic field sensor.

3.5.3 Energy Gates

3.5.3.1 Design Overview

The energy gates allow only particles of a specific E/q to pass. Figure 3.4 shows a schematic of the first energy gate. The top plate (ground plate) is at ground, and the bottom plate (deflection plate) is at a set voltage V, which generates a

uniform electric field in the y-axis. The MS is aligned with the ablation target such that particles enter the first energy gate traveling along the x-axis, and through an aperture in the first plate (entry aperture plate). A second aperture plate (exit aperture plate) is located at the end of the energy gate. Particles in the gate follow a parabolic trajectory, and at some V, only particles of a specific E/q reach the exit aperture. A particle's kinetic energy-to-charge ratio can be non-dimensionalized by dividing it by V, so the non-dimensionalized energy-to-charge η is defined as

$$\eta = \left(\frac{1/2\ mv^2}{qV} \right) \tag{3.1}$$

The value of η for particles which can pass through the energy gate is fixed by the gate's geometry, and is not dependent on V. The second gate has a similar design, but with the top plate at V instead. Therefore, the particles exit the second gate parallel to the x-axis, which is convenient for construction.

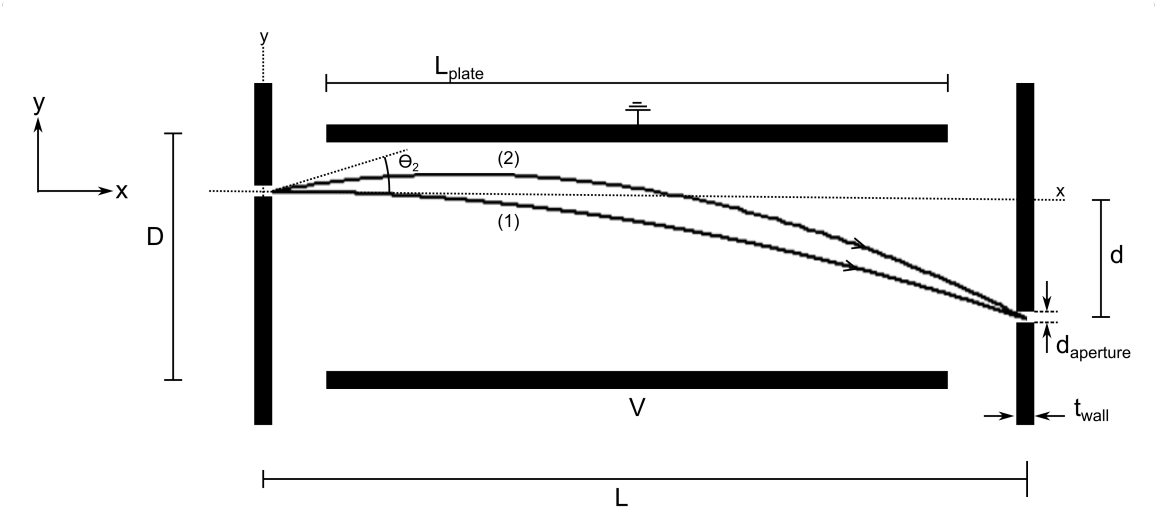

Figure 3.4: Schematic of Energy Gate. Trajectories of particles which can make it through the first energy gate are shown. (1) Desired particle trajectory. (2) Trajectory of a particle entering at a non-zero angle.

3.5.3.2 Uncertainty Analysis

Analysis of time-of-flight mass spectrometers of various geometries have been conducted previously in the literature [92], so here we will focus on the geometry used for our specific design. The energy gates only allow particles of a specific η to get through, assuming particles enter the first gate with the velocity only in the x-axis. If a particle enters the gate at some angle θ, it requires a different value of η to pass through the gate. Therefore, an uncertainty in θ corresponds to an uncertainty in η of the particles. Let us derive an equation for $\eta(\theta)$ for particles that can pass through the energy gate.

Figure 3.4 shows a schematic diagram of the energy gate. The origin is set at the entry aperture, and the exit aperture is located at $(D\hat{x} - d\hat{y})$ where D is the distance between the ground and deflection plate, and d is the distance in the y-axis between the entry and exit aperture. For an ideal parallel plate capacitor, the voltage between the ground and deflection plate creates a uniform electric field of $\boldsymbol{E_{cap}} = (V/D)\hat{y}$. Assuming a field of $\boldsymbol{E_{cap}}$ in the region between the ground and deflection plate and no field between the aperture plate and deflection plate, the average electric field is $\boldsymbol{E} = (L_{plate}/L)\boldsymbol{E_{cap}}$. L_{plate} is the length of the ground and deflection plate, and L is the distance between the aperture plates. For this analysis, we will assume a uniform electric field E inside the gate. The equations of motion for a particle in the gate are

$$m\ddot{x} = 0 \tag{3.2}$$

$$m\ddot{y} = \left(\frac{L_{plate}}{L}\right)\frac{qV}{D} \tag{3.3}$$

Since there are no forces in the x-axis, $x = \dot{x} = const$. Therefore, the time τ to traverse the gate is $\tau = L/\dot{x_0}$. Equation 3.3 is integrated twice, noting that the initial position in the y-axis is zero.

$$y(t) = \frac{1}{2}\left(\frac{L_{plate}}{L}\right)\frac{qV}{mD}t^2 + \dot{y}_0 t \tag{3.4}$$

At τ, the particle is at the exit aperture, so $y(\tau) = -d$. Substituting in for τ, this gives

$$-d = \frac{1}{2}\left(\frac{L_{plate}}{L}\right)\frac{qV}{mD}\left(\frac{L}{\dot{x}_0}\right)^2 + \dot{y}_0\left(\frac{L}{\dot{x}_0}\right) \tag{3.5}$$

Substituting $\tan(\theta) = \dot{y}_0/\dot{x}_0$, this can be rearranged to give

$$\frac{\frac{1}{2}m\dot{x}_0^2}{qV} = -\frac{\frac{1}{4}\left(\frac{L_{plate}}{L}\right)\frac{L^2}{D}}{d + L\tan(\theta)} \tag{3.6}$$

This can be rewritten in terms of initial kinetic energy, since

$$\begin{aligned} v_0^2 &= \dot{x}_0^2 + \dot{y}_0^2 \\ &= \dot{x}_0^2\left(1 + tan^2\left(\theta\right)\right) \\ &= \dot{x}_0^2\ sec^2\left(\theta\right) \end{aligned} \tag{3.7}$$

Therefore,

$$\eta(\theta) = \frac{\frac{1}{2}mv_0^2}{qV} = -\frac{\frac{1}{4}\left(\frac{L_{plate}}{L}\right)\frac{L^2}{D}}{d + L\tan(\theta)}\sec^2(\theta) \tag{3.8}$$

Let us define $\eta_0 \triangleq \eta(0)$. We therefore see that

$$\eta_0 = \frac{1}{4}\left(\frac{L_{gate}}{L}\right)\frac{L^2}{dD} \tag{3.9}$$

Expanding Equation 3.8 for small angles, we get

$$\eta(\theta) \approx \eta_0\left(1 - \frac{L}{d}\theta\right) \tag{3.10}$$

with θ in radians. Considering that D is on the same order as d, we see that η_0 scales as $(L/d)^2$. The maximum voltage that can be applied to the energy gate is constrained, so to increase the maximum particle energy that the gate can allow through, a large L/d is desired. However, Equation 3.10 shows that uncertainties in θ are amplified by a factor L/d when determining the uncertainty in η. This system is designed to allow for a large range of particle energies, ranging from ions to nanoparticles, to get through, so a high maximum energy is desired. In addition, a high precision of η would decrease the fluence of particles which get through the energy gates. Finally, a larger L/d fits better in the cylindrical chamber extension. For these reasons, a relatively large L/d was selected for the spectrometer design. Table 3.1 shows the values of the design parameters which were ultimately used for the gate design. With these parameters, the gate has a value of η_0 = -3.73 found using Equation 3.9. Note that the negative sign shows that the voltage must be biased to the opposite polarity of the particle charge.

To determine the uncertainty in η, we must first determine the uncertainty in θ. The spectrometer is able to be aligned with an uncertainty of approximately 2

Table 3.1: Energy gate design parameters.

Parameter	Value (mm)
L_{plate}	76.2
L	100
d	17
D	30
$d_{aperture}$	0.75

mm in the y-axis direction. The length of the field-free region between the ablation spot and the first gate is $L_{field-free} \approx 40$ cm. This corresponds to a σ_θ of 5 mrad. Using Equation 3.10, this corresponds to a 3% uncertainty in η.

Another source of uncertainty in the particle's energy comes from the size of the aperture. In the previous derivation, it was assumed that the particles entered and exited through the center of the apertures, traveling a distance d in the y-axis for one of the gates. This distance traveled could be off by as much as $d_{aperture}$, which corresponds to the uncertainty $\sigma_d = d_{aperture}$. This effect is determined by error propagation.

$$\left.\frac{\partial \eta}{\partial d}\right|_{\theta=0} = \eta_0 \left(-\frac{1}{d}\right) \tag{3.11}$$

Therefore, the fractional uncertainty due to the aperture diameter is $(d_{aperture}/d)$, which corresponds to a 4.4% uncertainty in η. As expected, a smaller aperture diameter reduces the uncertainty in η. This calculation can also be done for the effect of θ, similar to what was done in the Taylor expansion earlier.

$$\left.\frac{\partial \eta}{\partial \theta}\right|_{\theta=0} = \eta_0 \left(-\frac{L}{d}\right) \tag{3.12}$$

The root-mean-square (RMS) fractional uncertainty in η due to θ and d can be found by

$$\left(\frac{\sigma_\eta}{\eta_0}\right)^2 = \left(\frac{L}{d}\sigma_\theta\right)^2 + \left(\frac{1}{d}\sigma_d\right)^2 \tag{3.13}$$

Including the uncertainty due to θ, the RMS uncertainty of η is 5.3%.

3.5.3.3 Fringe Fields

To reduce the effect of non-ideal fringe fields, the gates are a modified Herzog shunt design [93–95]. In a typical Herzog shunt gate design, the entry and exit aperture plates are both at the potential which is the average of the top and bottom charged plates. In addition, the entry and exit apertures are both centered at the center of the aperture plates, and the apertures themselves are often large.

In our design, the apertures are located close to the charged plates. This allows for the electric field to be maximized for a given d. As seen in Figure 3.5, visualizations of the potential distribution found with a 2D COMSOL simulation showed that the electric field is more uniform along the particle trajectory if the aperture plates are at the same potential as the charged plate closest to the aperture. Using this model, the energy-to-charge that the gates allow through was found to be η_0 = -3.48. This provides a better estimate for η_0 than what was found in the previous section. The effect of θ predicted by Equation 3.10 should still be a

reasonable approximation.

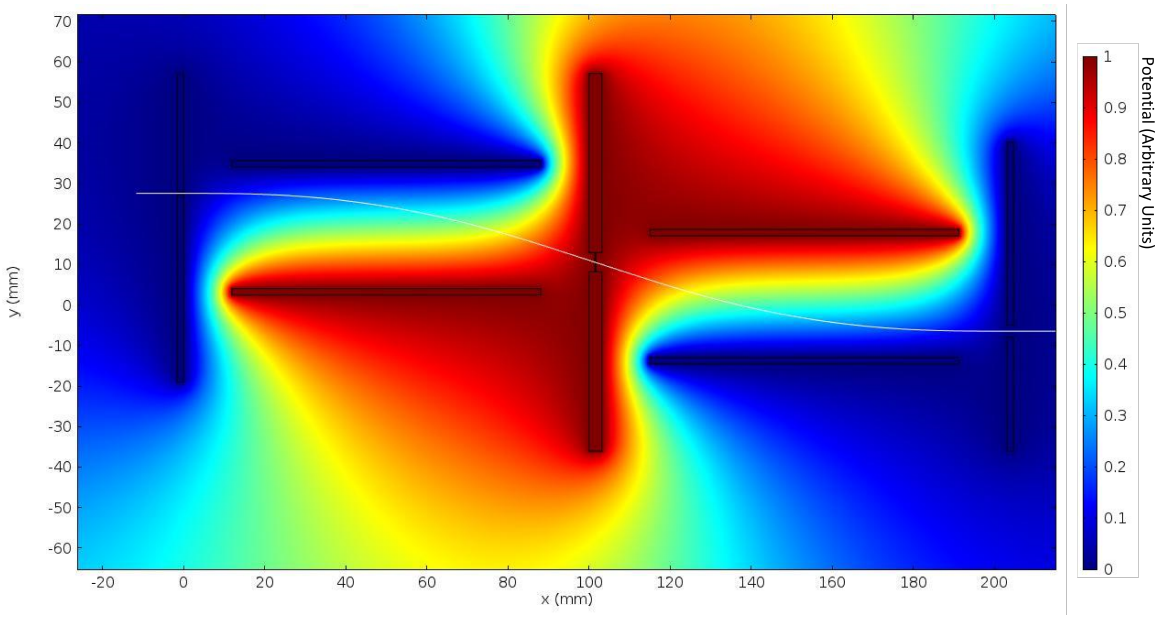

Figure 3.5: Potential for energy gates. White: trajectory of a particle going through the energy gates.

3.5.4 Detector

Following the gates, accelerator grids accelerate the charged particles into the back wall of the detector, which is at high voltage. In order for this to accelerate the incoming primary particles, it is set to -5 kV for detecting positive particles, and +5 kV for negative particles. These high energy particles collide with an aluminum wall at the back of the detector, releasing secondary electrons and secondary Al^+ ions. A polyvinyltoluene scintillator is biased to be ± 5 kV with respect to the detector potential, which accelerates either the secondary electrons or ions to it. When a secondary particle hits the scintillator, the scintillator releases photons. The photons are directed to a photomultiplier (PMT) by a conical light guide. The PMT amplifies the number of photons by a factor of $2 \cdot 10^6$, and outputs a current

proportional to the amplified light. The PMT output is connected to ground through a resistor. The oscilloscope measures the voltage drop over the resistor, and the current is found from Ohm's Law ($V = IR$).

As shown in Figure 3.6, there are three accelerator grid plates. d_{accel} is 11.6 mm, $d_{detector}$ is 23.8 mm, and $L_{detector}$ is 20 mm. The accelerator plate 1 is the same plate as the gate 2 exit aperture plate. The third plate is the same as the detector entry aperture plate. All three accelerator plates have a 3 mm aperture. As discussed previously, the first accelerator grid is always set to $V_1 = 0$ V, and the third grid is at $V_3 = \pm 5$ kV. The acceleration grids compose a three-aperture electrostatic immersion lens. The trajectory of a charged particle can be determined using Equations 1.14 and 1.41 of [94]. Using these equations, an intermediate voltage V_2 between V_1 and V_3 is found such that the particles are focused and stay within the accelerator apertures. Since the particle trajectory is a function of the particle's energy-per-charge selected by the energy gates, an acceptable value of V_2 is dependent on the particle's energy per charge.

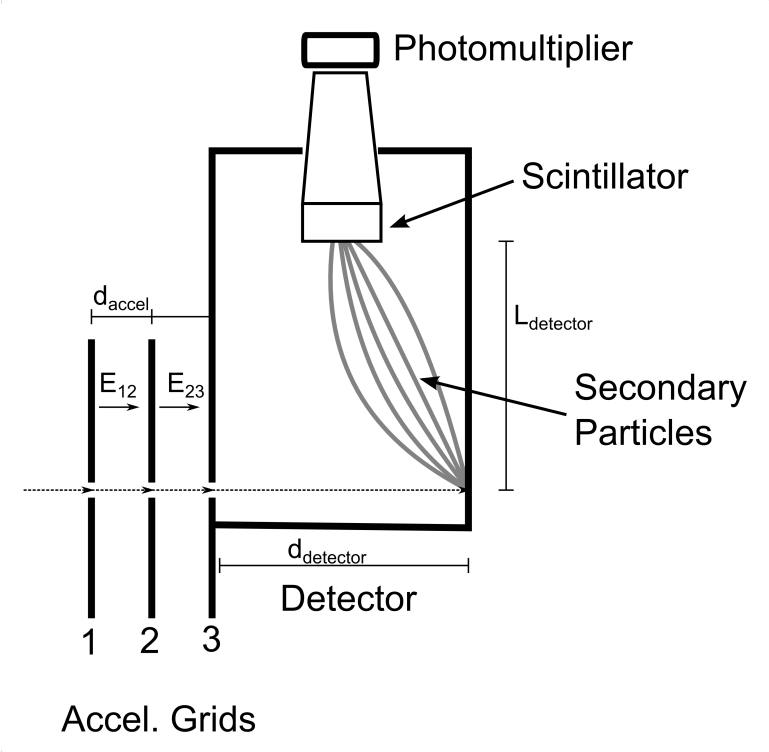

Figure 3.6: Schematic diagram of accelerator and detector.

We wish to determine the contribution the detector has on the total measured flight time. A particle in the accelerator regions is undergoing constant acceleration. The electric field between the first and second grid is $E_{12} = \frac{-(V_2 - V_1)}{d_{accel}}$. The particle enters the first aperture grid at $v_1 = v_0$. Similar to what was done in Equations 3.2-3.8, the equation of motion for the particle is integrated twice, and the time Δt_{12} to travel the distance d_{accel} is solved for. This is found to be

$$\Delta t_{12} = \frac{-v_1 + \sqrt{v_1^2 + \frac{2q(V_2 - V_1)}{m}}}{\frac{q(V_2 - V_1)}{m\ d_{accel}}} \tag{3.14}$$

The velocity at the start of the second accelerator plate is then found to be

$$v_2 = v_1 + \frac{qE_{12}}{m}\Delta t_{12} \tag{3.15}$$

The time spent between grids 2 and 3 (Δt_{23}), and the velocity at the third grid (v_3) is found using Equation 3.14 and Equation 3.15, and incrementing the indices. Following the accelerator grids, the primary particle travels through the detector at roughly constant velocity, so the time spent by the particle in the detector region is $d_{detector}/v_3$. The total time t_d that the primary particle spends in the accelerator grids and detector is therefore

$$t_d = \Delta t_{12} + \Delta t_{23} + \frac{d_{detector}}{v_3} \tag{3.16}$$

Note that t_d is a function of the particle's initial velocity v_0 and energy-per-charge ratio.

A 3D COMSOL model of the detector and scintillator was used to determine the time t_s for the secondary particles to reach the scintillator. The particle was released at rest at the back of the detector, and the time to reach the scintillator was found to be 3.7 ns for secondary electrons, and 830 ns for the heavier secondary ions.

The t_s for secondary ions is significant, so we wish to determine an uncertainty for it. This is found by releasing the secondary particles as a Gaussian distribution. Figure 3.7 shows a representative case, where the ions are initially at a temperature of 3 eV. For this case, the average t_s for the secondary ions was 800 ns, and the standard deviation was 100 ns.

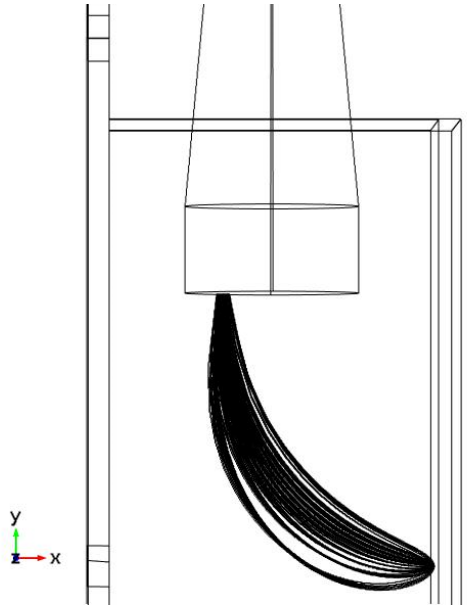

Figure 3.7: Secondary ions in detector. Aluminum secondary ions initially at 3 eV. 2D projection of trajectory.

The number of secondary particles released at the detector is in general a function of the energy of the primary particle. For future work, we wish to incorporate this relation into our analysis. Since the mass-to-charge ratio of the primary is known, an independent measurement of the particle's energy will allow the mass and charge to be determined, and not just the ratio of the two.

3.5.5 Time-of-Flight Measurement

The laser pulse begins at t = 0 and lasts for the pulse time $t_{pulse} = 0.7$ ns. For nanosecond laser pulses, the pulse time is much larger than both the material's electron cooling time and lattice heating time [36]. As such, the ablation process occurs during the ablation pulse time. A high-speed diode placed in the optics enclosure detects scattered light from the laser which marks the start of the TOF measure-

ment. Timing measurements are recorded with the PicoScope 5444A oscilloscope at a 125 MHz sampling rate, and therefore an 8 ns resolution.

For this discussion, we will consider the detection of a single particle. The particle travels through a field-free region between the ablation point and the start of the spectrometer (a distance of $L_{field-free}$ and time $t_{field-free}$). Then, the particle goes through the energy gates in time t_{gates}. The total length of the two gates, including the aperture plate thicknesses, is L_{gates}. In both the field-free region and the gates, there is no field in the x-axis, so the x-component of the velocity is constant. Therefore, we define the actual time of flight as $t_{TOF} = t_{field-free} + t_{gates}$. The particle's initial velocity is then found by

$$v_0 = \frac{L_{field-free} + L_{gates}}{t_{TOF}} \tag{3.17}$$

assuming the velocity is initially in the x-axis. t_f occurs when the Picoscope starts measuring the results from the photomultplier. The apparent time-of-flight, as seen by the Picoscope, is $t_f - t_0$. Accounting for the time spent by the primary and secondary particles in the detector, the actual time of flight is

$$t_{TOF} = (t_f - t_0) - (t_d + t_s) \tag{3.18}$$

Table 3.2 shows the approximate values of the times which are not dependent on the particle's initial velocity. From this table, we see that the combined delays associated with the photodiode, scintillator, and photomultiplier are less than two time steps measurable by the Picoscope. For simplicity, we will not account for

these values in the calculation for t_{TOF}, and instead treat these as contributions to the timing uncertainty.

Table 3.2: Timing values.

Photodiode*	5 ns	
Secondary e^-	3.7 ± 1 ns	
Secondary ions	800 ± 100 ns	
Scintillator†	0.9 ns	Rise time
	2.5 ns	Pulse FWHM
	2.1 ns	Decay time
PMT‡	0.57 ns	Rise time
	2.7 ns	Transit time
Picoscope§	125 MHz	Sampling rate
	8 ns	Resolution

* Rise time for SFH 203 silicon PIN photodiode

†Eljen EJ-200 Polyvinyltoluene Scintillator

‡Hamamatsu Photomultiplier Tube R9880U-210

§PicoScope 5444A with 4 channels enabled in 14 bit mode

The flight time in the accelerator plate and detector t_d is in general a function of v_0, the mass-to-charge ratio, and the energy-to charge ratio, as discussed in Equations 3.14-3.16. However, the measurement for v_0 is dependent on t_D, by Equations 3.17-3.18. Finally, m/q is related to v_0 by Equation 3.1, where η is the value of η_0 previously found for the gates, V is the potential set on the charged gate plates, and v is v_0. Equations 3.14-3.18 can be numerically solved for simultaneously to determine t_d, m/q, v_0, and t_{TOF}.

To simplify uncertainty propagation, let us now use the approximation that

$t_d \ll t_{TOF}$, in which case $t_{TOF} \approx t_f - t_0$. When the detector is in secondary electron mode, the uncertainty $\sigma_{t_{TOF}} \approx 2t_{res} = 16$ ns. This conveniently encapsulates all of the timing values in Table 2. In secondary ion mode, the uncertainty is dominated by $\sigma_{t_{TOF}} = \sigma_{t_s} = 100$ ns. Applying uncertainty propagation on Equation 3.17, we find

$$\left(\frac{\sigma_{v_0}}{v_0}\right)^2 = \frac{\sigma^2_{L_{field-free}} + \sigma^2_{L_{gates}}}{\left(L_{field-free} + L_{gates}\right)^2} + \left(\frac{\sigma_{t_{TOF}}}{t_{TOF}}\right)^2 \tag{3.19}$$

$\sigma_{L_{field-free}} \approx 1$ cm since it is difficult to measure the distance between the ablation point and the start of the spectrometer. L_{gates} can be measured much more accurately with a micrometer, so this does not contribute much to the uncertainty. Therefore, $\frac{\sigma_{L,TOF}}{L_{TOF}} = 1.7\%$. At low speeds, this dominates the uncertainty. At higher speeds, t_{TOF} is smaller while $\sigma_{t_{TOF}}$ is constant, so the contribution from this term dominates. The two terms are equal at $v_0 = 6.4 \cdot 10^5$ $(1.0 \cdot 10^5)$ m/s for secondary electron (ion) mode.

Equation 3.1 can be rearranged to solve for m/q

$$\frac{m}{q} = \frac{\eta V}{v_0^2} \tag{3.20}$$

Using error propagation, we see

$$\left(\frac{\sigma_{m/q}}{m/q}\right)^2 = \left(\frac{\sigma_{v_0}}{v_0}\right)^2 + \left(\frac{\sigma_\eta}{\eta}\right)^2 \tag{3.21}$$

Therefore, the uncertainty in the mass-to-charge ratio is greater than 5.6%, and is dependent on the particle's initial velocity.

3.5.6 3D Model

Based on the dimensions used in the 2D model, a 3D CAD model of the spectrometer was created using Autodesk Inventor, shown in Figure 3.8. The corners of the charged plates are rounded to reduce the amount of high electric fields at sharp corners. The components of the spectrometer are attached to a 3D printed base. This provides the necessary precision for the spectrometer components, and also insulates the components. The 3D printed material was tested to handle high voltages. The 3D printed base is then mounted to two strut channels, which provide additional structural support as well as assist in placing the spectrometer in the vacuum chamber.

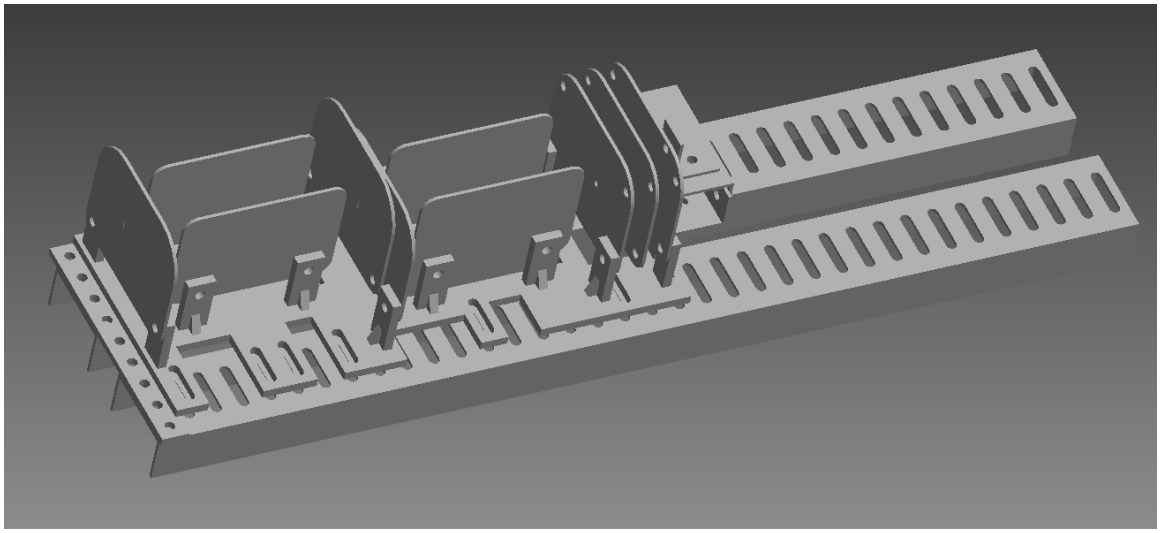

Figure 3.8: Mass spectrometer CAD model.

Figure 3.9: Assembled mass spectrometer.

As discussed in section 3.5, a small aperture diameter is required to have high precision for η, in the 2D case. The electric field is not strongly dependent on the position in the z-axis (normal to the particle path), so the requirement for a small aperture diameter is not applicable in this direction. To increase the fluence of particles without effecting the uncertainty in η, the apertures are actually slits with a 3 mm length in the z-axis, and still with a 0.75 mm diameter in the XY plane.

The CAD model was then imported into COMSOL to confirm the results of the 2D model. In this model, the strut channels are grounded, as is the cylindrical magnetic shield (not shown). Figure 3.10(a) shows the case where the charged gate plates are at -10 V, and the detector is at -5 kV. At this relatively low voltage on the charged gate plates, the field inside the second gate is distorted. The section cut normal to the particle plane of motion shows that the potential from the accelerator

grids and detector is coming over the gate 2 exit aperture plate, and the results are shown in Figure 3.10(a-b). The grounded strut-channels help keep the field from coming from under the aperture plate.

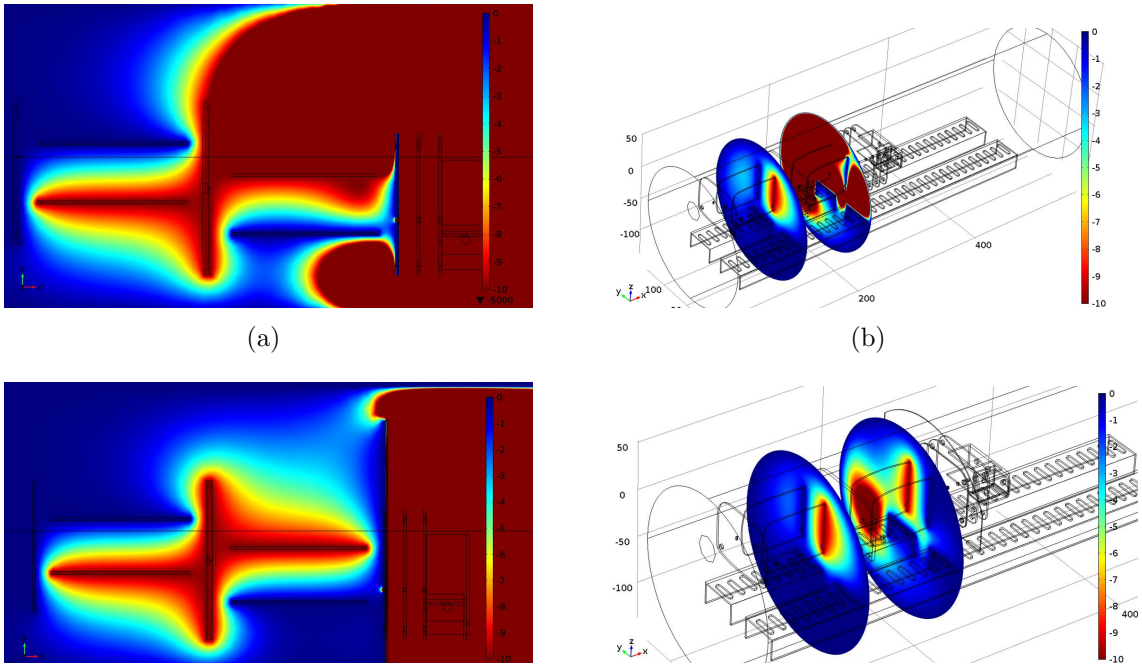

(a) (b)

(c) (d)

Figure 3.10: Potential distribution of 3D mass spectrometer model. The cylindrical mu-shield and struts are grounded. The charged gate plates are at -10 V. The accelerator plates and detector are at -5 kV. The scale of the potential is between -10 V and 0 V for ease of visualization. In (a, b), the high voltage from the detector distorts the field in the second gate. In (c, d), grounded shielding is added to the gate 2 exit aperture plate, which reduces the effect of the high voltage detector on the gate potential.

To counteract the effect of the high voltage, additional shielding is provided by extending the grounded gate 2 exit aperture plate. The results are shown in Figure 3.10(c-d). With this updated 3D model, the value of η_0 for the gates was found to be -3.48, which agrees with the 2D model. With a complete 3D model, the spectrometer was constructed, and is shown in Figure 3.9.

3.6 Future Work

3.6.1 Mass Spectrometer Calibration

Before using the mass spectrometer to characterize the laser ablation plasma, we first need to calibrate the spectrometer with an ion source which generates previously well-characterized ions. To accomplish this, we are currently working on incorporating an ionic liquid ion source developed at the MIT Space Propulsion Laboratory [96, 97]. The referenced papers include details of the design and fabrication of this device, so we will discuss it here only as a brief overview.

Ionic liquids have virtually no offgassing making them very stable in vacuum operation [97]. They are also molten salts which are liquid at room temperature, and are highly conductive and composed of ions and anions. In this setup, a drop of ionic liquid is placed on the distal contact electrode, and this drop is the reservoir. This provides an electrical connection between the contact electrode and the sharp-tipped needle. Capillary action draws the liquid to the tip of the needle. A voltage bias V_0 of about 1 kV is applied to the needle with respect to the grounded extractor. This forms a strong electric field at the needle tip, which extracts ions directly from the liquid. The ions are then accelerated and exit the extractor. These particles are monoenergetic, with an energy of V_0 [90]. Depending on the polarity of V_0, either positive or negative ions are extracted. One commonly used ionic liquid which we plan on using for our future tests is EMI-BF_4, whose monomers are EMI^+ and BF_4^-. In addition to these monomers, heavier ions are also present which include

combinations of the positive and negative monomers.

This ion source is mounted to the XYZ translational stages in our chamber. The ion source emits a constant current of approximately 100 nA, so additional gating is needed after the extractor plate to pulse the particles. Ionic liquid ions are significantly heavier than individual aluminum ions. Because of this, they can be used to test the relation between particle mass and velocity to secondary emission in the detector for heavier particles.

3.6.2 Laser Ablation Plume

Following the completion of the calibration tests, the mass spectrometer will be used to characterize the laser ablation plume's velocity, charge, and mass distributions. For particle bombardment studies, it is critical to know the properties of the particles which are bombarding, which is why the ablation plume will be characterized with the spectrometer. In addition, the mass spectrometer can be used to filter the bombardment particles. In this configuration, the detector of the spectrometer can be replaced with a material to be bombarded. Then, the energy gates will filter out particles of a specific energy-per-charge. The charged gate plates can be pulsed with some delay with respect to the ablation pulse to further filter by velocity. The mass-to-charge ratio distribution is likely a function of the energy-to-charge, which will have been found with the spectrometer characterization. Finally, the accelerator plates can be used to adjust the energy-to-charge of the particles before they bombard the sample.

3.7 Conclusion

In this paper, we have discussed the design of a time-of-flight mass spectrometer developed to characterize a plasma plume generated by laser ablation. Uncertainty analysis was conducted on the spectrometer design. The energy gates were found to be able to determine a particle's energy-to-charge ratio to 5%. At low speeds, the particle's velocity can be found with a 2% uncertainty, and the uncertainty increases with increasing particle velocity. The particle's mass-to-charge ratio can be found with a 6% uncertainty. These uncertainty calculations did not consider the effect of particle interaction, both during initial plasma formation and also in the field-free region. Future tests with an ionic liquid ion source will experimentally validate the spectrometer design using particles of known mass, charge, and energy. Additional research is also needed to relate the number of secondary particles emitted at the detector to the energy of the incident particles.

3.8 Acknowledgments

I would like to thank Catherine Miller and her advisor Dr. Paulo Lozano at the MIT Space Propulsion Laboratory for providing and helping set up the ionic liquid ion source. I would also like to thank my advisor Dr. Sedwick, and Eric Smith. This material is based upon work supported by the National Science Foundation Graduate Research Fellowship Program under Grant No. DGE 1322106. This research is also supported by the Air Force Office of Scientific Research (AFOSR).

Chapter 4: Validation of a Time-of-Flight Mass Spectrometer Using an Ionic Liquid Ion Source

The following chapter is a pre-print of a journal article. The published version of this journal article is:

[98] Sloane, J., Smith, E., and Sedwick, R., "Validation of a time-of-flight mass spectrometer using an ionic liquid ion source," *International Journal of Mass Spectrometry*, vol. 432, 2018, pp. 36-43.

4.1 Abstract

A low-cost time-of-flight mass spectrometer has been developed to characterize the plasma plume resulting from pulsed laser ablation. In this paper, an ionic liquid ion source using EMI-BF_4 is used to experimentally validate the spectrometer, as well as a model of the spectrometer. The mass spectrometer is shown to experimentally measure the energy-per-charge distribution of the ion source, and match with literature. In addition, a relation between alignment error and measurement error predicted by theory is confirmed, further validating the model. Now that it has been validated, the spectrometer can confidently be used to determine the two-dimensional distribution of speed and energy-per-charge of a pulsed laser ablation plasma, or other pulsed plasma sources.

4.2 Introduction

A sub-nanosecond pulsed laser fired at a target material generates an ablation plasma plume of ions, ion clusters, and nanoparticles [99,100]. This paper introduces the design of a time-of-flight mass spectrometer (TOF-MS) to use for characterizing the plasma plume generated by laser ablation, developed by the authors at the University of Maryland College Park Space Power and Propulsion Laboratory (SPPL). Multiple configurations and designs for TOF-MS systems are discussed in literature [79, 83, 92, 101, 102]. The mass spectrometer in this paper is designed to

measure charged particles with energies up to 30 keV, so particles ranging from ions to clusters and nanoparticles can be detected. The energy range of this design, combined with the ease of fabrication, makes this spectrometer design very useful. This paper focuses on simulations and validation experiments conducted in order to properly process the raw output of the TOF-MS. The validation experiments are conducted using an ionic liquid ion source. This ion source generates large ions of a known mass and energy, so the TOF-MS measurements can be compared to the expected values.

Research is currently being conducted at SPPL using a Xenon and Argon ion source to analyze the effect of particle bombardment on spacecraft material [88], such as solar panels, as would be exposed in the space environment. A laser ablation plasma source extends this capability by increasing the sizes of energetic particles that can be generated. Before being used to conduct satellite impingement tests, the plasma plume must first be well characterized.

In addition, laser ablation can be used to generate thrust for space propulsion [33, 45]. This is particularly well suited for deorbiting orbital debris [45, 49, 103], or deflecting asteroids from a collision with Earth [15, 51, 104], since the objects to be moved can be used as the propellant. Characterization of the plasma plume's mass, energy, and velocity distributions with the TOF-MS can be used to calculate the propulsion parameters associated with ablation.

4.3 Hardware Overview

4.3.1 Laser Ablation Facility

Figure 4.1 shows a schematic diagram of the laser ablation facility. The laser is a Q-Switched Nd-Y2SO4 (Photonics Industries model SN-1064-40). It emits pulses of 0.7 ns (FWHM) duration at a wavelength of 1064 nm. The laser is operated at 40 kHz, with a maximum pulse energy of 827 μJ. Inside an optics enclosure, the laser is expanded by a beam expander, and then focused to a point in the vacuum chamber. The target material to be ablated is mounted on XYZ translational stages to allow it to be moved and maintain a fresh ablation spot. The ablation plume has a cosine dependence with the center of the plume normal to the target surface [89], and is oriented to go towards the TOF-MS.

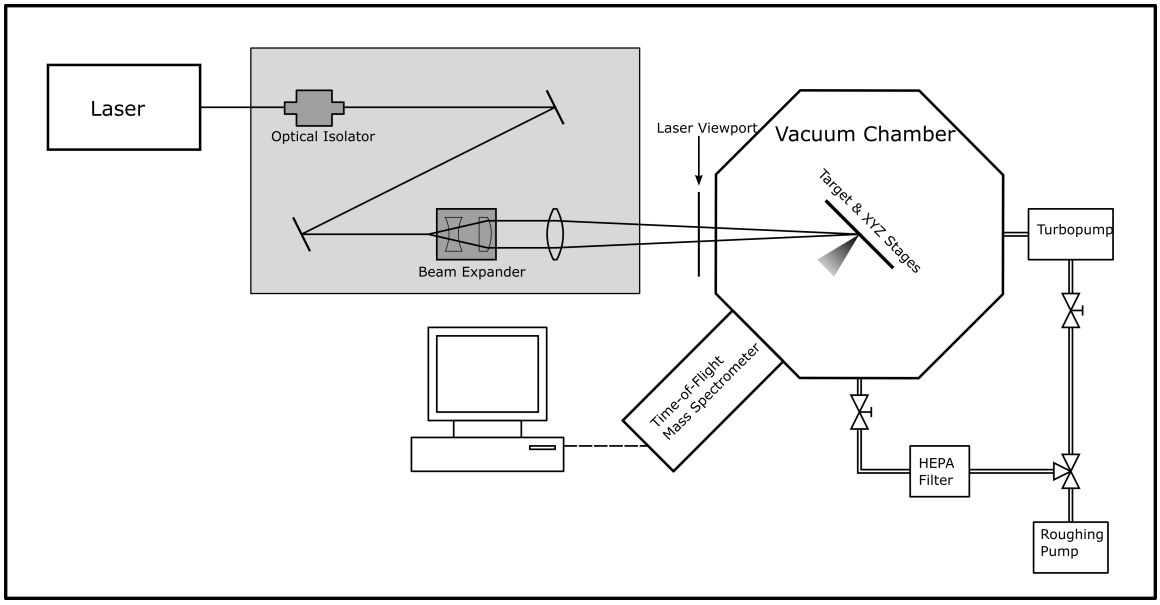

Figure 4.1: Schematic of hardware.

4.3.2 Time-of-Flight Mass Spectrometer

Figure 4.2 shows a schematic diagram of the TOF-MS. The spectrometry measurement begins with a single laser pulse, which generates a plasma ablation plume and marks the start of the TOF. After traversing through a field-free region, the particles reach the energy gates, which filter particles by their energy-to-charge ratio $\widetilde{E}$ by setting the center plates to a voltage V. Throughout this paper, the $\sim$ accent is used to denote variables that are per-charge.

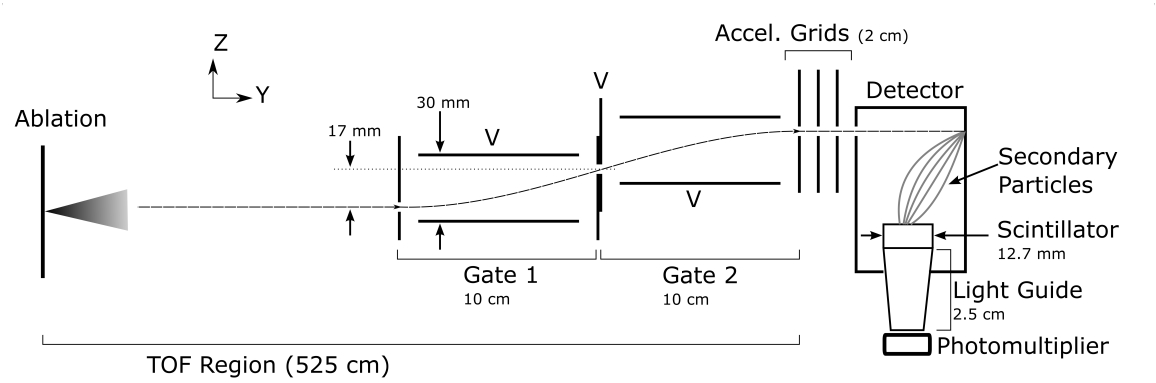

Figure 4.2: Schematic of time-of-flight mass spectrometer.

A particle of the correct $\widetilde{E}$ is then accelerated and collides with the back wall of the detector, releasing secondary particles. The number of secondary particles released is a function of the kinetic energy of the primary ablation particle. The secondary particles are accelerated to the scintillator, which generates light when it is hit with the particles. This signal is amplified by the photomultiplier, which is in turn measured by the oscilloscope. The time between the ablation pulse occurring and the photomultiplier signal corresponds to the time of flight of a particle.

Since the distance between the ablation spot and detector is known, the par-

ticle velocity v can be calculated using the TOF measurement. The particle's $\widetilde{E}$ is known from the energy gates. Finally, the particle's kinetic energy is determined from the number of secondary particles emitted. From $E = \frac{1}{2}mv^2$, the mass and charge of the particle are determined. Analysis relating primary particle kinetic energy with the number of secondary particles emitted is left for future work.

4.3.3 Ionic Liquid Ion Source

Before characterizing a plasma plume of unknown distribution, the spectrometer is validated using well-characterized ions. This was done using an ionic liquid ion source developed at the MIT Space Propulsion Laboratory [96, 97], which was borrowed for these experiments. The referenced papers include details of the design and fabrication of this device. A diagram of the ion source is shown in Figure 4.3.

Ionic liquids are molten salts which are liquid at room temperature, highly conductive, and composed of both positive and negative ions. Ionic liquids have virtually no off-gassing, making them very stable in vacuum operation [105]. Ionic liquid ion sources have been analyzed with TOF-MS previously in literature [97, 106, 107]. In the setup discussed in this paper, a drop of ionic liquid is placed on a reservoir attached to the distal contact electrode. The liquid provides an electrical connection between the contact electrode and the sharp-tipped needle. Capillary action draws the liquid to the tip of the needle. A voltage bias V_0 of 1-2 kV is applied to the needle with respect to the grounded extractor. The strong electric field at the needle tip forms a Taylor cone [108], from which ions are emitted directly from

the liquid. Most of these particles are monoenergetic [90], with an energy slightly less than V_0. Depending on the polarity of V_0, either positive or negative ions are extracted. In this paper EMI-BF_4, whose monomers are EMI^+ and BF_4^-, is used. In addition to these monomers, combinations of monomers called dimers are present, such as (EMI-BF_4)-BF_4^-. If a dimer splits into a monomer and neutral after being emitted, it will have an energy V_{min} based on the relative mass of the monomer to the dimer [90]. If this split occurs between the needle and the extractor plate, the monomer will have an energy between V_{min} and V_0.

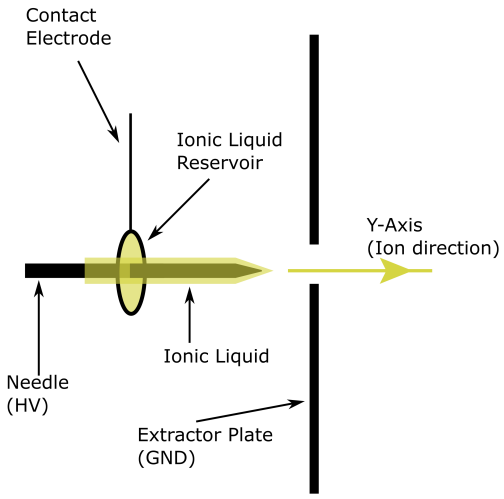

(a)

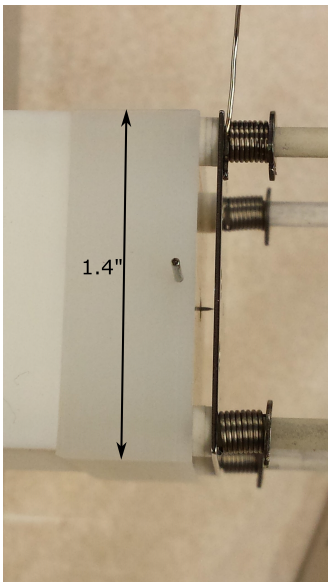

(b)

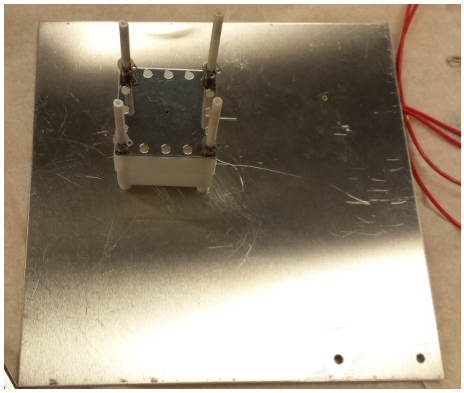

(c)

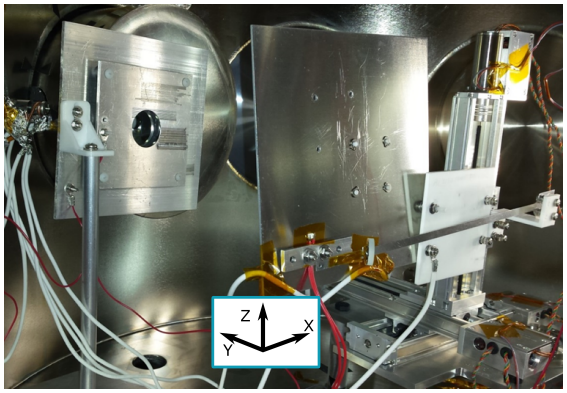

(d)

Figure 4.3: Diagram onf an ionic liquid ion source. (a) Schematic, (b) ion source, (c) ion source on grounded back plate, (d) ion source and back plate mounted on XYZ translation stages in the vacuum chamber.

This ion source is mounted to the XYZ translational stages in the vacuum chamber. The needle tip's nominal position is at the laser focal spot, so the alignment with the TOF-MS is the same for the ion source as it is for ablation. The ion source emits a constant current of approximately 100 nA. Since the current is not pulsed, there are no measurements of the particle's velocity, and the output signal is proportional to the energy-per-charge distribution (see Equation 4.2). Due to the low particle flow rate at the detector, the current from the photomultiplier is very low.

The setup and alignment of the ion source is done with the following methodology. To change the ionic liquid, the ion source is first completely disassembled, and each component cleaned in an ultrasonic bath. The ion source is then reassembled. The needle is aligned to be centered at the extractor plate, and the distance between the needle and the extractor plate is set by eye to be approximately 0.5 mm, assisted by a magnifying glass. The liquid is placed in the vacuum chamber at rouging pump pressure for at least a half hour to outgas. A drop of ionic liquid is then placed on the reservoir between the needle and the contact electrode. The reservoir is slid up and down to coat the tip of the needle. In vacuum, the current emitted by the ion source is measured, along with the alignment. If needed, the stage and mounting plate orientations are adjusted to correct for alignment issues. If the ion source is not emitting as desired, this procedure is repeated.

Using this setup, an energy sweep is conducted. Before the sweep begins, the XYZ stages move the ion source to a specified position. The accelerator plate, detector, scintillator, and needle are all set to constant voltages. This current hitting

the spectrometer front aperture plate is amplified by an inverting op-amp circuit, which is measured by an Arduino. Secondary electron emission is likely occurring when ions hit the aperture plate, which will increase the apparent current measured. Nonetheless, this current is still useful to normalize the spectrometer signal, which helps mitigate the effect of variance in the ion source's output current. In order for ions to be emitted, a sufficiently strong voltage must be applied between the needle and the extractor plate [97], referred to here as the turn-on voltage. During operation, the turn-on voltage for this ion source ranged from 1-2 kV. This voltage was found to be different on different experiment days, and sometimes even between tests. In addition, the current emitted by the ion source varied substantially between days, ranging from 50 nA to 2 mA. This range is due in part because of the sensitivity in the distance between the needle and the extractor plate, which can change during alignment. To help mitigate the ion source's inconsistencies, only experiments performed on the same test day are compared to each other, and data collected while the ion source is operating inconsistently are discarded.

The photomultiplier current is monitored by a Keithley 6485 Picoammeter. In addition, the voltage on the gate deflection plate is set by a Keithley 2410 SourceMeter.

To perform the energy sweep, the gate is set to a voltage V. The current at the photomultiplier is measured, and recorded as the average value of 5 measurements taken over 0.2 s. In addition, the Arduino reports the current hitting the front aperture plate. Then, the gate voltage is incremented. To speed up data collection, if little current is detected from the photomultiplier, a larger step size is used. The

energy sweep is then repeated, typically 3-7 times, to give more statistical data and to confirm that the ion source was stable through multiple sweeps.

4.4 Time-of-Flight Mass Spectrometer Model

The TOF-MS can be analyzed analytically with a simple model, with constant electric fields in the z-axis within the gates, constant fields in the y-axis between the acceleration grids, and field-free everywhere else. For a more accurate model, COMSOL Multiphysics v4.4 is used to calculate the electric field due to the three-dimensional geometry of the spectrometer in the vacuum chamber. Charged particle tracing, ignoring particle-particle interactions, is used to determine the particle trajectories. In this section, the COMSOL model is used to relate the time dependent flow of particles at the detector with the plasma's energy-per-charge distribution function.

With the energy gate set to a voltage of V, the spectrometer will let in particles with energy-per-charge near $\widetilde{E}_0$, where $\widetilde{E}_0 = \eta_0 V$. The maximum voltage that can be safely applied to the gates in this setup is 8.5 kV. η_0 is a constant based on the geometry of the energy gates, and was found to be -3.48 using COMSOL. This value is negative because the gate's polarity is opposite to the polarity of the charge that passes through the gate. The maximum voltage that can be safely applied to the gates in this setup is 8.5 kV, so particles with energy less than 30 keV can be detected, since $\widetilde{E}_{0,max} = \eta_0 V_{max}$. The photomultiplier provides a time-resolved signal based on the rate that particles hit the end of the detector.

Consider an ablation plume with an energy-per-charge distribution $f_{\widetilde{E}}(\widetilde{E})$ that we wish to characterize. Let $f_{\widetilde{E}}(\widetilde{E})$ be normalized such that $\int f_{\widetilde{E}}(\widetilde{E})d\widetilde{E}$ is 1. With the energy gate set to a voltage V, the number of primary particles measured at the detector is $M(\widetilde{E}_0)$. Particles are modelled as being emitted at a point at the ablation spot. Therefore, particles that pass through the entry aperture of the gates have a range of positions, angles, and energies, which all effect whether a particle passes through the energy gates. Let us define $g(\widetilde{E}, \widetilde{E}_0)$ as the fraction of particles with energy $\widetilde{E}$ that reach the detector, when the gates are set to V. Therefore,

$$M(\widetilde{E}_0) = \int_0^\infty f_{\widetilde{E}}(\widetilde{E})\ g(\widetilde{E}, \widetilde{E}_0)d\widetilde{E} \tag{4.1}$$

It will be shown later that g is a Gaussian function centered at $\widetilde{E} = \widetilde{E}_0$. Approximating $f_{\widetilde{E}}$ as a constant near $\widetilde{E}_0$ (since this is where g is not small),

$$f_{\widetilde{E}}(\widetilde{E}_0) = \frac{M\left(\widetilde{E}_0\right)}{\int_0^\infty g(\widetilde{E}, \widetilde{E}_0)d\widetilde{E}} \tag{4.2}$$

In order to complete the relation between f and M, we must characterize g. To do this, consider the response to the impulse energy distribution function

$$f_I(\widetilde{E}) = \delta(\widetilde{E} - \widetilde{E}^*) \tag{4.3}$$

This corresponds to a normalized energy distribution, with all particles at energy $\widetilde{E}^*$. The measured impulse response M_I is

$$M_I(\widetilde{E} = \widetilde{E}^*, \tilde{E}_0) = \int_0^\infty \delta(\widetilde{E} - \widetilde{E}^*)\ g(\widetilde{E}, \widetilde{E}_0)d\widetilde{E} \tag{4.4}$$

By the definition of the Dirac Delta function,

$$M_I(\widetilde{E}^*, \widetilde{E}_0) = g(\widetilde{E}^*, \tilde{E}_0) \tag{4.5}$$

Therefore, by finding M_I at various values of $\widetilde{E}^*$ and $\widetilde{E}_0$, we can determine g. A group of particles of identical mass, charge, and initial energy-per-charge $\widetilde{E}$ are released in COMSOL 43 cm to the left of the entry aperture and in line with the aperture. The particles have a random angle in the y-z plane for initial velocity, with a maximum angle selected to be large enough that some particles do not make it past the entry aperture. The detector and accelerator plates are set to -5 kV. Defocusing in the accelerator region may prevent some particles from reaching the detector at low gate voltages. To check for this effect, gate voltages of (0.2, 0.4, 0.6, 0.8, 1) kV were considered. For each gate voltage, 7 values of $\widetilde{E}^*$ were tested. For each combination of $\left(\widetilde{E}^*, \widetilde{E}_0\right)$, the number of particles that reach the end of the detector divided by the number of particles that get through the entry aperture is calculated, to give $M_I(\widetilde{E}^*, \widetilde{E}_0)$ which equals $g(\widetilde{E}^*, \widetilde{E}_0)$.

Let us normalize the energy-per-charge by $\widetilde{E}_0$, so the normalized energy-per-charge $x = \widetilde{E}/\widetilde{E}_0$, and $g_x(x, \widetilde{E}_0) = g(\widetilde{E}, \widetilde{E}_0)$. With the non-dimensionalized variables, we fit a Gaussian to each curve.

$$g_{x,fit}(x, \widetilde{E}_0) = a \cdot \exp\left(-\frac{(x-b)^2}{2c^2}\right) \tag{4.6}$$

Since $x = \widetilde{E}/\widetilde{E}_0$, $dx = d\widetilde{E}/\widetilde{E}_0$, and

$$g_x(x, \widetilde{E}_0)dx = g(\widetilde{E}, \widetilde{E}_0)\ \widetilde{E}_0\ d\widetilde{E} \tag{4.7}$$

The results of the COMSOL simulation, as well as the Gaussian fits, are shown in Figure 4.4. The Gaussian fit parameters are summarized in Table 4.1.

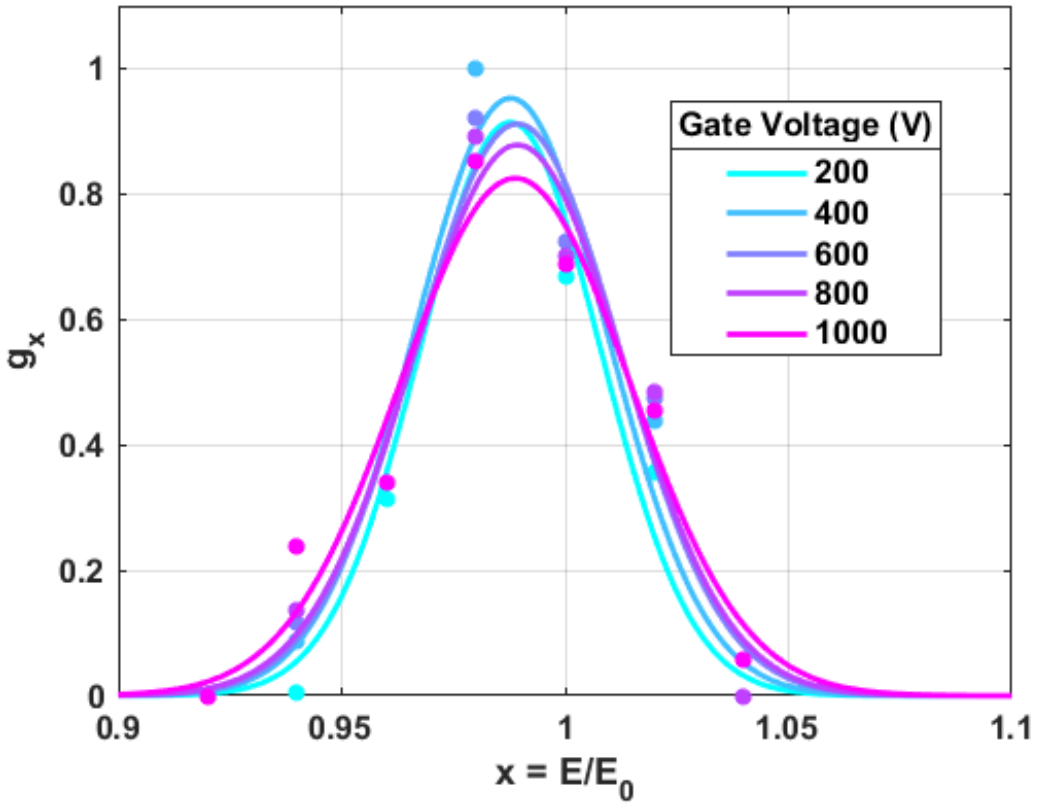

Figure 4.4: Fraction of particles that pass through the spectrometer energy gates as a function of the particle energy.

Table 4.1: Gaussian fit parameters.

V (Volts)	a	b	c	$I = \int g_{x,fit}(x, \widetilde{E}_0)dx$
200	0.9144	0.9877	0.0202	0.0462
400	0.9528	0.9878	0.0216	0.0517
600	0.9118	0.9893	0.0229	0.0524
800	0.8782	0.9894	0.0236	0.0520
1000	0.8251	0.9888	0.0257	0.0531

From Table 4.1, we see that b is close to one. This agrees with the previously identified value of η_0, which was chosen so particles with $\widetilde{E} = \widetilde{E}_0$ go through the center of the apertures. There is also a small drop in the integral of $g_{x,fit}$ at 200 V as a result of defocusing, and above that it is roughly constant at $I = 0.0523$. c corresponds to the standard deviation of the Gaussian, and shows that the energy gate lets particles through with energies within 2.5% of $\widetilde{E}_0$. This can be thought of as the energy-per-charge uncertainty associated with the gate Gaussian bandpass filter.

The detector on the TOF-MS does not measure the total number of particles at a certain energy $M(\widetilde{E}_0)$, but instead measures the rate of particles per time hitting the detector $M_t(t, \widetilde{E}_0)$. This allows us to characterize the particle distribution by energy-to-charge ratio and by velocity, instead of just by energy-to-charge ratio. Consider particles emitted instantaneously from the ablation spot. The distance from the ablation spot to the detector is the total time-of-flight (TOF) distance L. Assuming no charged particle interactions, the time to reach the detector is found

by

$$\frac{1}{2}\frac{m}{q}v^2 = \widetilde{E} \tag{4.8}$$

$$vt = L \tag{4.9}$$

$$t = L\sqrt{\frac{m/q}{2\widetilde{E}}} \tag{4.10}$$

Consider the normalized particle speed distribution $f_v(v)$, which corresponds to the fraction of particles with speed between v and $v + dv$. A 2-dimensional distribution, which is a function of both energy-per-charge and particle speed is given by $f_{\widetilde{E},v}(\widetilde{E}, v)$. This more general distribution can be used to obtain $f_{\widetilde{E}}$ by

$$f_{\widetilde{E}} = \int f_{\widetilde{E},v}(\widetilde{E}, v)dv \tag{4.11}$$

This is normalized such that the double integral of $f_{\widetilde{E},v}$ is one. This can be converted to a distribution of energy-per-charge and time-of-flight by using Equation 4.9 and its partial derivative.

$$f_{\widetilde{E},t}(\widetilde{E}, t)\ d\widetilde{E}\ dt = f_{\widetilde{E},v}(\widetilde{E}, L/t)\ d\widetilde{E}\ dv \cdot \left(\frac{L}{t^2}\right) \tag{4.12}$$

With the energy gates set to $\widetilde{E}_0$, the particle flow rate at the detector $M_t(\widetilde{E}_0, t)$ is related to this distribution by

$$M_t(\widetilde{E}_0, t) = \int f_{\widetilde{E},t}(\widetilde{E}, t)\ g(\widetilde{E}, \widetilde{E}_0)\ d\widetilde{E} \tag{4.13}$$

This can be used to calculate M

$$M(\widetilde{E}) = \int M_t(\widetilde{E}, t)dt \tag{4.14}$$

Again, we can approximate $f_{\widetilde{E},t}(\widetilde{E}, t) \approx f_{\widetilde{E},t}(\widetilde{E}_0, t)$. Therefore,

$$f_{\widetilde{E},t}(\widetilde{E}_0, t) = \frac{M_t(\widetilde{E}_0, t)}{\int g(\widetilde{E}, \widetilde{E}_0)d\widetilde{E}} \tag{4.15}$$

Substituting the results from Table 4.1, we get

$$f_{\widetilde{E},t}(\widetilde{E}_0, t) = \frac{M_t(\widetilde{E}_0, t)}{\widetilde{E}_0 \cdot I} \tag{4.16}$$

This is then converted back to $f_{\widetilde{E},v}$ by Equation 4.12.

$$f_{\widetilde{E},v}(\widetilde{E}_0, v) = \frac{M_t(\widetilde{E}_0, \frac{L}{v}) \cdot \frac{L}{v^2}}{\widetilde{E}_0 \cdot I} \tag{4.17}$$

By experimentally measuring $M_t(t)$ at various values of $\widetilde{E}_0$, the 2D distribution function $f_{\widetilde{E},v}$ can be found. This gives us a combined energy-to-charge and speed distribution function for the ablation plume.

Consider an energy distribution $f_{\widetilde{E}}(\widetilde{E})$ for particles with a single mass-to-charge ratio $\widetilde{m}$. The associated $f_{\widetilde{E},v}$ distribution is $f_{\widetilde{E}}(\widetilde{E})\ \delta(\widetilde{E} - \frac{1}{2}\widetilde{m}v^2)$. It can be shown using the equations above, without approximating $f_{\widetilde{E},v}$ as constant, that the distribution measured by the spectrometer is $f_{\widetilde{E}}(\widetilde{E})\ g_{x,fit}\left(\frac{\frac{1}{2}\widetilde{m}v^2}{\widetilde{E}_0}\right) \cdot \frac{1}{I}$. This shows that the delta function in the actual distribution appears to the spectrometer as a Gaussian. If multiple Gaussians are present in M_t, and are associated with ions (or clusters of ions) with unambiguous mass-to-charge ratios, we can first split up

the M_t into distinct Gaussians. Then, Equations 4.2 and 4.14 can be used on each Gaussian to get the energy-to-charge distributions for each mass-to-charge ratio. This is more accurate than approximating f as constant, and should be done when possible.

Since $t \propto \frac{1}{\sqrt{\widetilde{E}}}$, and the uncertainty of $\widetilde{E}$ for particles that reach the detector is about 3%, the uncertainty in t due to uncertainty in $\widetilde{E}$ is very small.

4.5 Results and Discussion

4.5.1 Varying Ion Source Vertical Position

When particles enter the TOF-MS along the y-axis, the energy gates select particles with energy-to-charge $\widetilde{E}_0 = \eta_0 V$. If the TOF-MS is not aligned properly, particles may enter with some small angle θ in the YZ plane. Assuming small angles, and a uniform field in the energy gate, the correction for η is given by

$$\eta(\theta) \approx \eta_0 \left(1 - \frac{L}{d}\theta\right) \tag{4.18}$$

where L (100 mm) is the distance in the y-axis from the start to the end an energy gate, d (17 mm) is the distance in the Z-axis between the entry and exit aperture of an energy gate, and θ is in radians. Equation 4.18 is used to relate the uncertainty in the TOF-MS alignment with the corresponding uncertainty in the particle energy-per-charge. While the laser focal spot is fixed in space by the optics, the ionic liquid ion source can be moved via the XYZ translation stages. Because of this, the ion source is used to experimentally confirm this effect.

For this set of tests, energy sweeps are measured with the ion source at several positions in the vertical Z-axis. The ion source is 26.8 cm from the entry aperture in the horizontal Y-axis, so the ions enter the MS with an angle $\theta = \tan^{-1}\left(\frac{-\Delta Z}{26.8\ \text{cm}}\right)$. For these tests, V_{neelde} = 1453 V, $V_{detector}$ = -4984 V, and $V_{scintillator}$ = GND. EMI-BF_4 was used as the ionic liquid. Before starting these tests, the current emitted by the ion source was measured, and found to be outputting a consistent 130 nA. Since the needle is at a positive bias, positive ions from the ion source are emitted. Since the scintillator is at a higher voltage than the detector, secondary electrons are measured. The normalized energy-per-charge is found by dividing the measured energy-per-charge $\widetilde{E}$ by the needle voltage V_{needle}. When the ion source is properly aligned, we expect to see the largest energy peak occur when the normalized energy is slightly less than one, and no particles having larger energy than this. The normalized photomultiplier current is the magnitude of the current measured by the photomultiplier, divided by the current at the front aperture plate.

Figure 4.5 shows the resulting energy sweeps. The peak for $\Delta Z = 0$ cm occurs at a normalized energy slightly greater than one. This is likely because the ion source was not perfectly aligned in the nominal position. Aside from this offset, the energy distribution is as expected from literature, with the main peak at V_0, and one or two smaller peaks at lower energy corresponding to broken dimers. In addition, the width of the main Gaussian matches closely with Figure 4.4, as expected for monoenergetic particles. This provides experimental validation for the COMSOL model, as well as the operation of the TOF-MS.

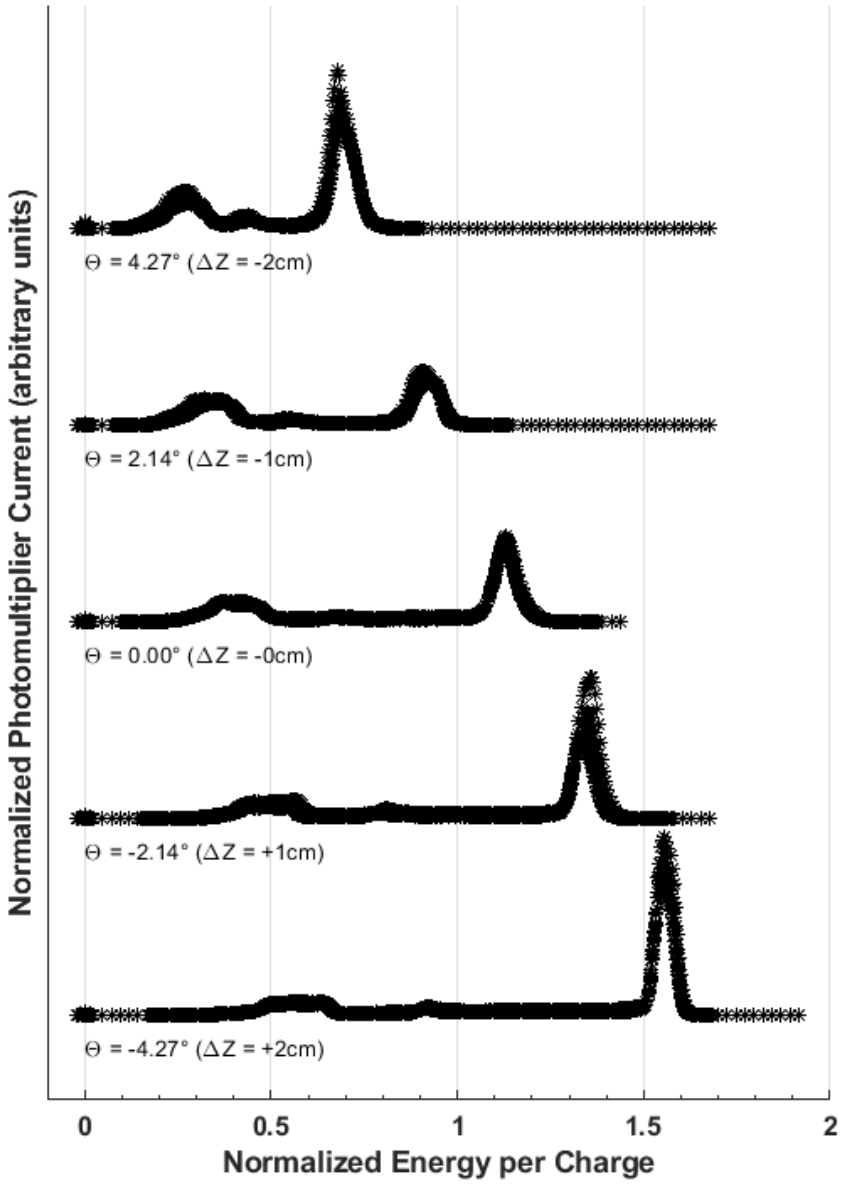

Figure 4.5: Ion source energy sweeps - varying top stage position.

A plot of the normalized energy at the peak signal vs. entry angle to the spectrometer is shown in Figure 4.6. From Equation 4.18, the expected slope is $-\frac{L}{d} \cdot \frac{\pi}{180^\circ}$, which is -0.103 deg^{-1}. This agrees well with the slope found in Figure 4.6, further validating the model. This result shows that the ion source had a 1.25° error in top stage position, corresponds to a 5.6 mm position error and a 12% error in measured energy. Precise alignment of the ion source to the laser focal spot was challenging, and a 5 mm alignment error is reasonable. The techniques used to align the spectrometer to the laser spot are more precise, with an error of less than 1 mm, corresponding to a 2.2% energy uncertainty.

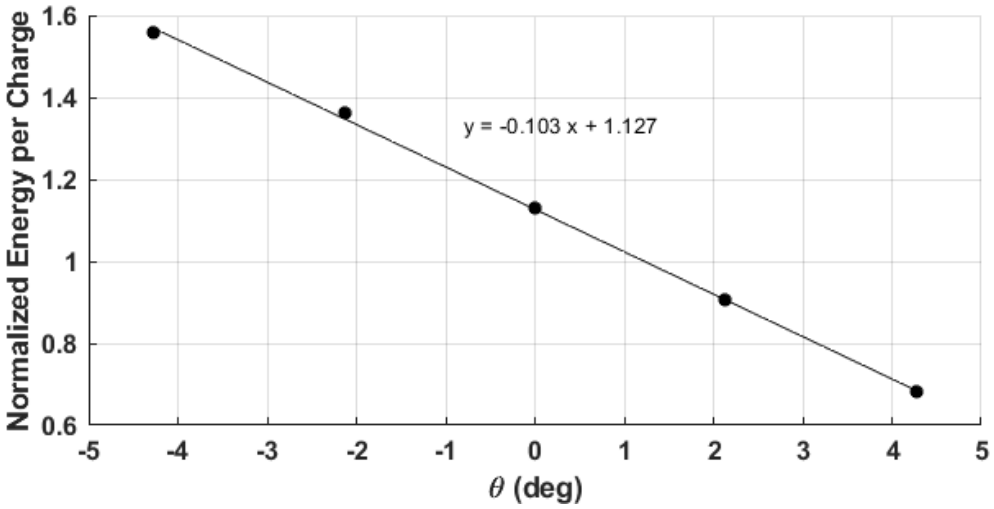

Figure 4.6: Effect of top stage position on measured ion source peak energy.

4.5.2 Varying Distance of Ion Source to the Spectrometer

The effect of varying the distance of the ion source to the MS is also tested. By changing the total distance the ions travel, the amount of time that particle-particle interaction occurs changes. Particle-particle interaction can lead to a thermalization

of the monoenergetic particles, which would be seen as a widening of the Gaussians in the energy distribution. In addition, the number of dimers that split will increase with a longer flight time. We are interested in seeing if either of these effects have a noticeable impact on the measured energy-per-charge distribution.

For this set of tests, the middle stage is set to different positions in the y-axis, with a larger middle stage position corresponding to the ion source being closer to the MS. For each middle stage position, the top and bottom stages are moved to maximize the current detected by the photomultiplier, while V_{gate} is at a constant 400 V. This process changes the top stage alignment, leading to the measured energy to be off by some constant multiple. This is not a major concern for these tests because the comparisons done are relative. Figure 4.7 shows the energy sweep results for different middle stage positions. The ratio between the height of the small peaks and the large peak did not change significantly between cases. In addition, the width of the large peak did not change significantly either. Therefore, the effects tested here are not of sufficient concern for our interest to warrant further investigation with the ion source. For laser ablation, beam spreading may still be an issue, since the particles are released in a bunch instead of continuously, and the charge density is greater.

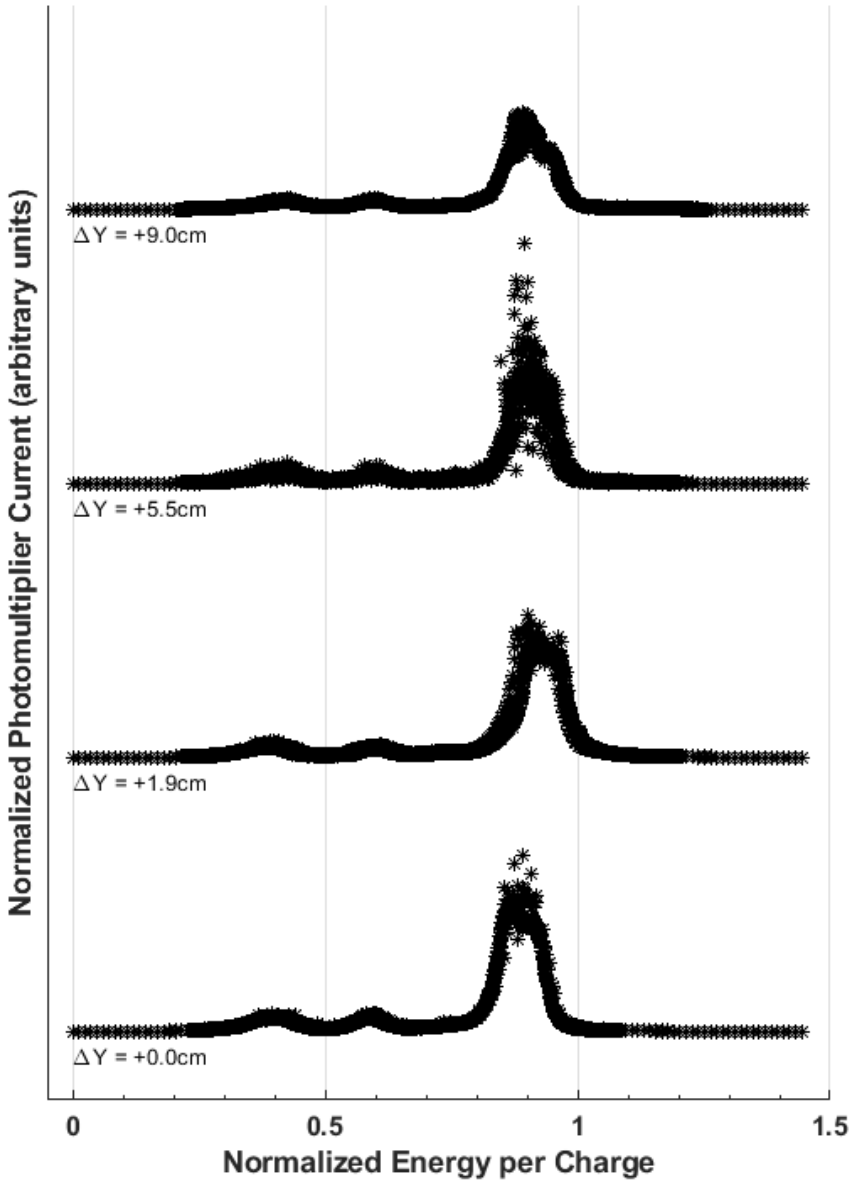

Figure 4.7: Ion source energy sweeps – varying middle stage position.

4.6 Conclusion

In this paper, experiments were conducted to validate a model for a custom-built TOF-MS. Equations were derived to calculate the plasma's energy-to-charge distribution based on the time-resolved particle flow rate into the detector. An ionic liquid ion source was used to experimentally validate the effect of misalignment of the TOF-MS in the vertical Z-axis. The experimental results agreed well with the theory, and show that the relation between error in the particle entry angle θ and the corresponding error in the measured energy-to-charge is -0.103 deg^{-1}. The effect of moving the ion source along the TOF-MS Y-axis on the energy distribution was also tested, and no apparent effect was seen on the width of the distribution.

4.7 Acknowledgments

The authors would like to thank Catherine Miller and her advisor Dr. Paulo Lozano at the MIT Space Propulsion Laboratory for providing and helping set up the ionic liquid ion source. This material is based upon work supported by the National Science Foundation Graduate Research Fellowship Program under Grant No. DGE 1322106. This research is also supported by the Air Force Office of Scientific Research (AFOSR).

Chapter 5: Time-of-Flight Mass Spectrometry Analysis of Pulsed Laser Ablation of Pyroxene

The following chapter is a pre-print of a journal article. The published version of this journal article is:

[109] Sloane, J., Smith, E., and Sedwick, R., "Time-of-flight mass spectrometry analysis of pulsed laser ablation of pyroxene," AIP Advances, vol. 9, 025019 (2019). https://doi.org/10.1063/1.5085461.

5.1 Abstract

Pulsed laser ablation experiments on pyroxene rock have been conducted. A 1064 nm laser with a 0.7 ns pulse width is used to generate ablation in vacuum. The resulting plasma plume is characterized with a time-of-flight mass spectrometer. Pyroxene is a mineral commonly found in S-Type asteroids. Laser ablation generates thrust, and can be used to move an asteroid off of an Earth impacting trajectory, or to a more favorable orbit for *in-situ* resource utilization. In addition, time-of-flight mass spectrometry can be used for *in-situ* analysis of asteroids. From the data collected in this experiment, a two-dimensional distribution of the positive ions is found as a function of speed and mass per charge. From the distribution, the specific impulse of the positive ions is found to be 6920 s. This is an overestimate of the overall efficiency, since it does not consider efficiency losses or the speed of neutrals and larger particles.

5.2 Introduction

In 2013, a 20 meter diameter Near-Earth Asteroid (NEA) exploded over Chelyabinsk, Russia. This injured over 1,600 people, and Planetary Defense Officer Lindley Johnson described the event as "a cosmic wake-up call" [110]. Numerous approaches have been proposed for deflecting or destroying asteroids on a collision course for Earth, ranging in energy from gravity tractors to nuclear-tipped impactors [25, 29, 30, 111].

While low energy techniques require months to years to apply an impulse, they do not have the risk of fragmenting the asteroid.

Laser ablation propulsion (LAP) is a promising low-thrust technology for asteroid mitigation. A laser is fired at a spot on the asteroid, which generates a directed high-energy plasma plume, generating thrust. The laser can be used to de-spin the asteroid before capturing, or maintain a standoff distance while firing the laser and never needing to mechanically interact with the potentially tumbling asteroid [112]. Since the asteroid itself is used as a propellant, there is no need to carry additional propellant for the deflection maneuver of the asteroid. It has also been proposed to scale up the laser power, so an asteroid deflection system can be stationed as far as 1 AU from the impending asteroid [51]. With LAP, an asteroid can also be moved to a more favorable orbit for *in-situ* resource utilization. Similarly, asteroid rocks can be extracted and used as propellant for interplanetary spacecraft missions.

Laser ablation has been studied extensively in various similar areas of research. LAP has been studied for orbital debris removal [45], since it also benefits from using the debris itself as the propellant. Elemental targets are often used when studying LAP [84], which simplifies analysis of the fundamental physics. Another application of LAP is for station-keeping, with a major benefit being the small minimum-impulse-bit achievable. For this application, custom made polymers are often used, with high ablation efficiency [42]. Thrust stands [85], time-of-flight mass spectrometry [39], and high-speed images of the plume [58] are some of the most commonly used techniques to analyze LAP.

Time-of-flight mass spectrometers have been analyzed for *in-situ* analysis of

planets and small bodies [81, 113]. In addition, laser ablation has been used to simulate the space weathering effect on moon regolith, since the timescale and energy of a 10 ns laser pulse are comparable to that of a micrometeoroid impact [68].

However, relatively little experimental research has been conducted focusing on LAP of asteroid materials. Of the ongoing research [31, 60], no experiments have been conducted using a pulsed laser to the author's knowledge. In this paper, ablation of augite pyroxene (commonly found in silicaceous S-Type asteroids [114]), using a sub-nanosecond pulsed laser is analyzed. A time-of-flight mass spectrometer developed by the authors is used to characterize the two-dimensional distribution of the ions in the plasma plume as a function of speed and mass-per-charge. For more a more detailed discussion about the design and theory of the spectrometer used, see [98, 115]. From the distribution, the specific impulse (I_{sp}) is calculated. A two-dimensional distribution allows for a more accurate calculation of I_{sp}, as well as provides more insight about which ions are most contributing to the I_{sp}.

5.3 Experiment Setup

The Photonics Industries model SN-1064-40 laser is used, which has a 0.7 ns pulse width and 1064 nm wavelength. The pulse rate is set to 40 kHz, with each pulse having energy of 827 μJ, corresponding to 33 W average power. Ablation of aluminum at optimal focus was examined using a scanning electron microscope, and the diameter of the ablation spot was found to be 50 μm. From this, the peak fluence of the laser is found to be 42 J/cm^2. Individual pulses are fired by activating an

opto-electric shutter. The laser pulse, as observed by a fast photodiode, marks the start of the flight time. The laser is then focused to the center of a vacuum chamber (1 mPa nominal operating pressure), where the pyroxene target is held in place by an aluminum mounting bracket. This bracket is connected to XYZ translational stages using a Macor slab, to insulate the stages.

The pyroxene sample was procured from Wards Science (item #470015-436), and was custom cut to a 50x50x4 mm slab. It was then sanded using T414 fine-grid sandpaper. Even after sanding, the surface had clear macroscopic imperfections. The focused laser spot is on the order of 0.1 mm, so the imperfections may affect the resulting ablation plume. After sanding, the target is cleaned with isopropyl alcohol, then placed in an ultrasonic water bath for 5 minutes, and allowed to dry for at least 24 hours. Figure 5.1 shows the pyroxene in the chamber.

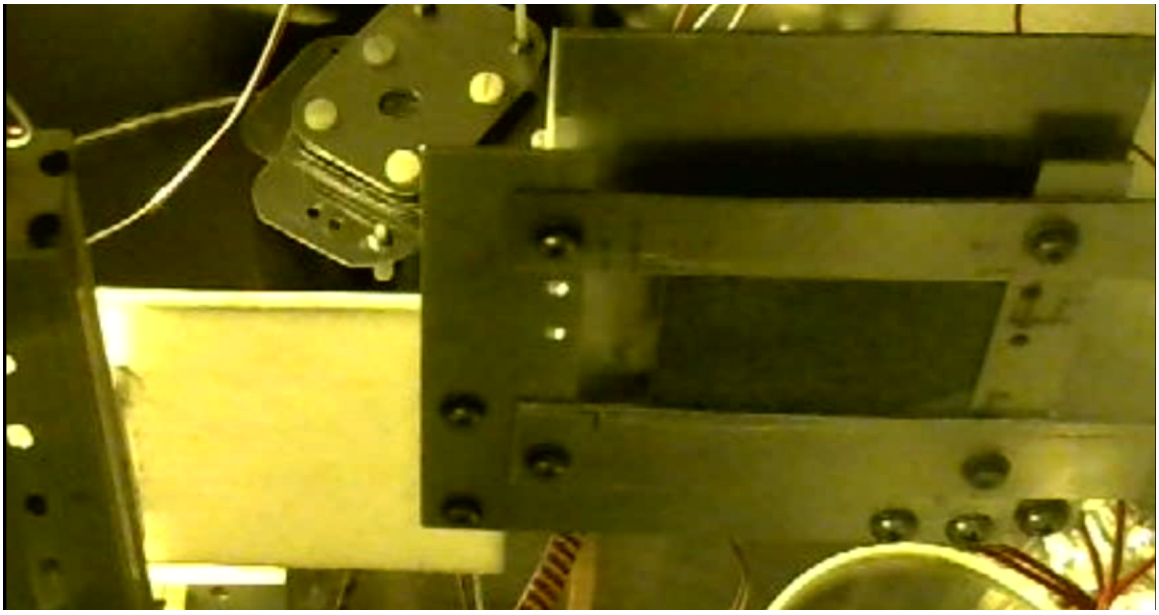

(a)

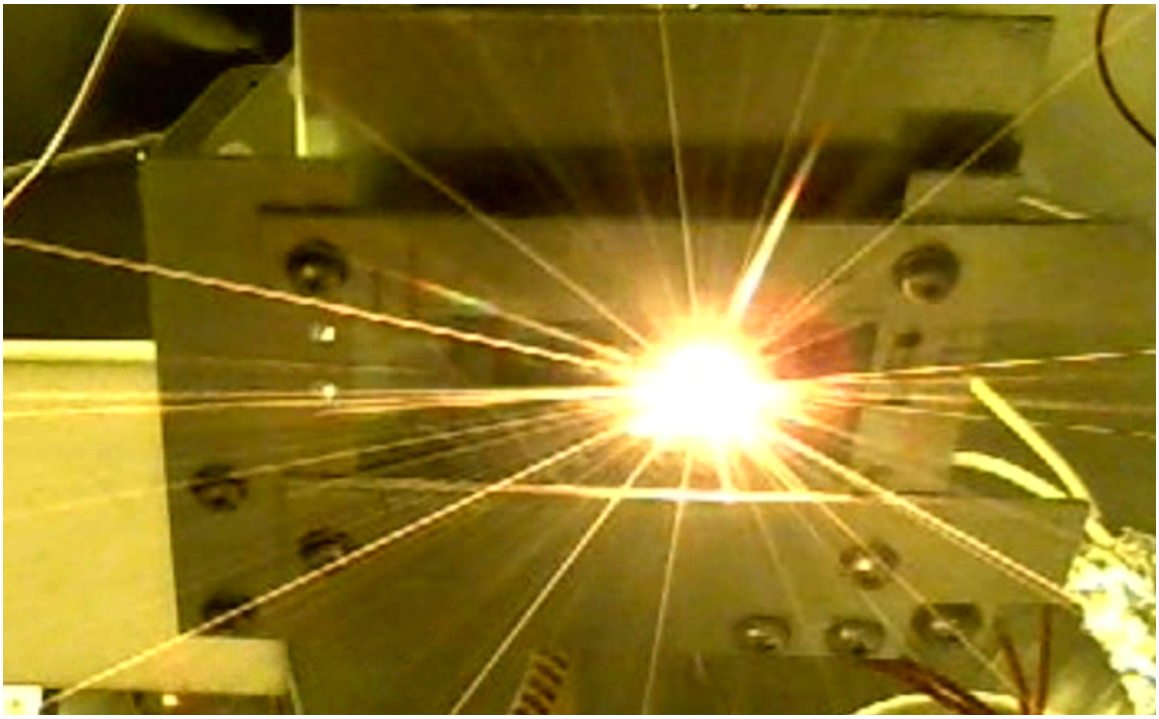

(b)

Figure 5.1: Pyroxene target mounted in vacuum chamber. (a) Pyroxene with laser off; (b) Pyroxene with the laser firing at 40 kHz, and the target moving from the right to the left at 2 mm/s.

The laser hits the target at a 45° angle, and the target is oriented so the normal to its surface is in-line with the TOF-MS. It has been found that plumes resulting from ablation of metal are directional with a $cos^n(\theta)$ dependence, where $\theta = 0$ is normal to the surface [39, 116]. Multiple pulses at the same ablation spot will tunnel into the material, which directs the plume back towards the laser. The authors have seen clearly directed plumes in previous work using aluminum, and have also seen the plume direction be dependent on the target speed. As seen in Figure 5.1, the ablation event is very strong, and too bright to clearly determine an angular dependence. This may be due in part to the coarseness of the pyroxene target, as well as the lower conductivity, which may lead to more melting of the surrounding region.

According to literature, ablation of aluminum begins to degrade by pulse 40 at the same spot [89]. The authors have seen this effect when analyzing aluminum. Preliminary TOF-MS analysis of pyroxene showed no noticeable change in signal strength over the first 500 pulses.

After the laser is fired, the ablation particles travel through a field-free region before entering the TOF-MS (see Figure 5.2). The particles then enter an energy gate, which contains an electric field normal to the particle motion. Based on the gate voltage V, only particles of the selected energy/charge of $-3.48 \cdot V$ will get through the energy gate [98], where the minus sign denotes the opposite polarity between the gate voltage and the particle charge. A second gate deflects the particles to be back in-line. The particles are then accelerated by 4 kV, where they hit an aluminum plate at the back of the detector box. The impact releases secondary

electrons, which are accelerated into a scintillator (+4 kV relative to detector), to produce light. The light is amplified by a photomultiplier (PMT), which in turn outputs a current.

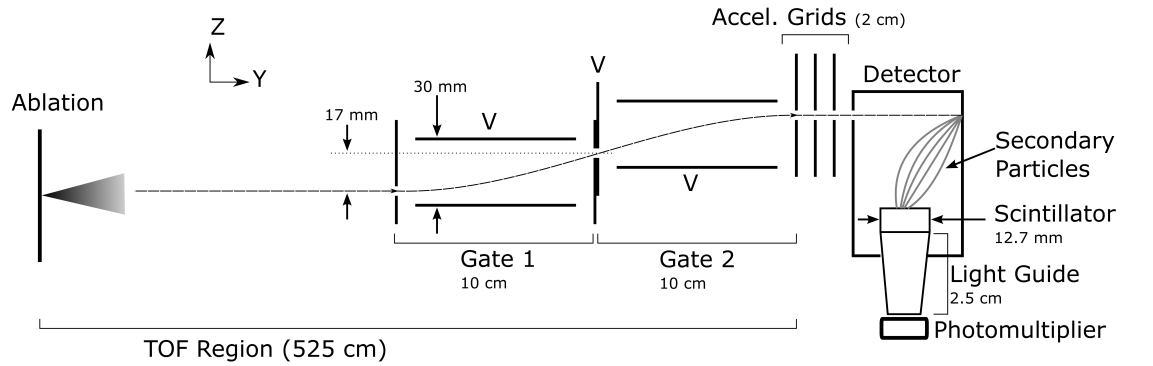

Figure 5.2: Schematic of time-of-flight mass spectrometer. Reproduced with permission from [98]: Sloane, J., Smith, E., and Sedwick, R., "Validation of a time-of-flight mass spectrometer using an ionic liquid ion source," *International Journal of Mass Spectrometry*, vol. 432, 2018, pp. 36-43. Copyright 2018, Elsevier.

At each ablation spot, the gate voltage V is set, a laser pulse is fired, and the PMT signal measured over time is recorded. This is repeated for 200 pulses and a single gate voltage. Then, the target is moved so the ablation spot is fresh, and the gate voltage is incremented by 2.5 V. These steps are repeated until the full energy sweep is complete. For consistency, and simplicity of analysis, only pulse 7 is discussed in this paper. This pulse number was selected to allow for any surface contamination to be cleaned off by the first several pulses. Due to small step sizes in the energy gate voltage, the single pulse number provided sufficient data, so averaging over multiple pulses was not needed. Preliminary analysis of pulse 20, as well pulse 7 captured from a different energy sweep, showed similar results.

5.4 Results and Discussion

5.4.1 Raw Photomultiplier Signal

The PMT output current is grounded over a 2.5 kΩ resistor. The voltage over the resistor is monitored using PicoScope 5444A oscilloscope. An example of the raw output data is shown in Figure 5.3 for pulse 7. Figures 5.3(a) and 5.3(b) each correspond to a single laser pulse.

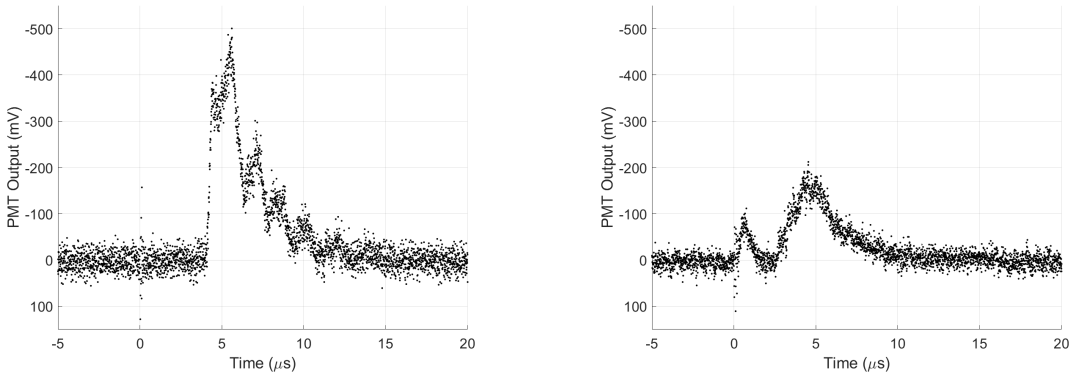

(a) (b)

Figure 5.3: Sample time-of-flight mass spectrometer (TOF-MS) raw photomultiplier (PMT) output. (a) Positive primary ions with energy/charge = 400 V; (b) Negative primary ions with energy/charge = -400 V.

The energy sweep of the positive ions was conducted first. Before starting the negative ion sweep, the high-voltage electronics were temporarily turned off so the detector and scintillator biases could be re-wired for different voltages. In addition, the code driving the experiment needed to be reset in the middle of the negative ion sweep at particle energy/charge of -922 V. The energy sweep was re-started from this energy, but the PMT current did not taper off over time as quickly after

re-starting.

For both the positive and negative ions, a signal spike is seen immediately at $t = 0$. This signal is likely electrical noise due to RF ringing from the laser firing.

5.4.2 Photomultiplier Current

The PMT current flows through a resistor to ground, and the voltage is recorded by the oscilloscope. There is a parasitic capacitance C_p of 125 pF [115]. Therefore, this can be modeled as an RC circuit, and current output from the PMT can be calculated from the measured voltage from

$$I(t) = \frac{V(t)}{R} + C_p \frac{dV(t)}{dt} \tag{5.1}$$

The standard deviation of the voltage before the laser is pulsed is calculated. Dividing this by R (and ignoring the effect of C_p) the noise in the PMT current is calculated to be 7.6 μA.

Equation 5.1 requires the voltage derivative. The voltage is smoothed using the Savitzky-Golay filter (Matlab built-in function sgolay) with a 5% span before calculating its derivative. The current $I(t)$ is calculated using Equation 5.1 using the raw voltage and the smooth voltage derivative. This current is then smoothed using the Savitzky-Golay filter with a 2.5% span. Values of the smoothed current above -2σ noise are set to zero. Figure 5.4 shows the resulting PMT output current for the energies shown in Figure 5.3. Figure 5.5 shows the PMT output vs. time for the entire energy sweep. Each vertical line in the 2d plot corresponds to a single

laser pulse, noting that the energy filter is constant for each pulse.

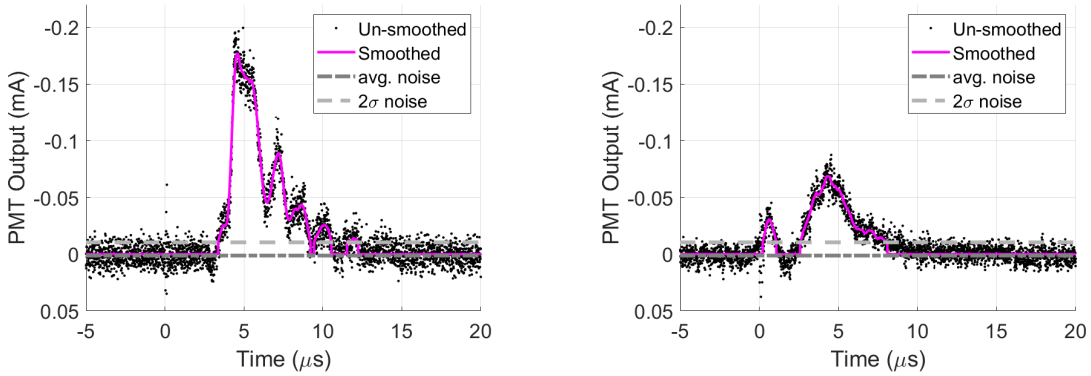

Figure 5.4: Sample photomultiplier output current. The raw PMT voltage is first converted to a current (black dots). Then, the data is smoothed using a 2.5% span Savitzky-Golay filter (magenta solid line). (a) Positive primary ions with energy/charge = 400 V; (b) Negative primary ions with energy/charge = -400 V.

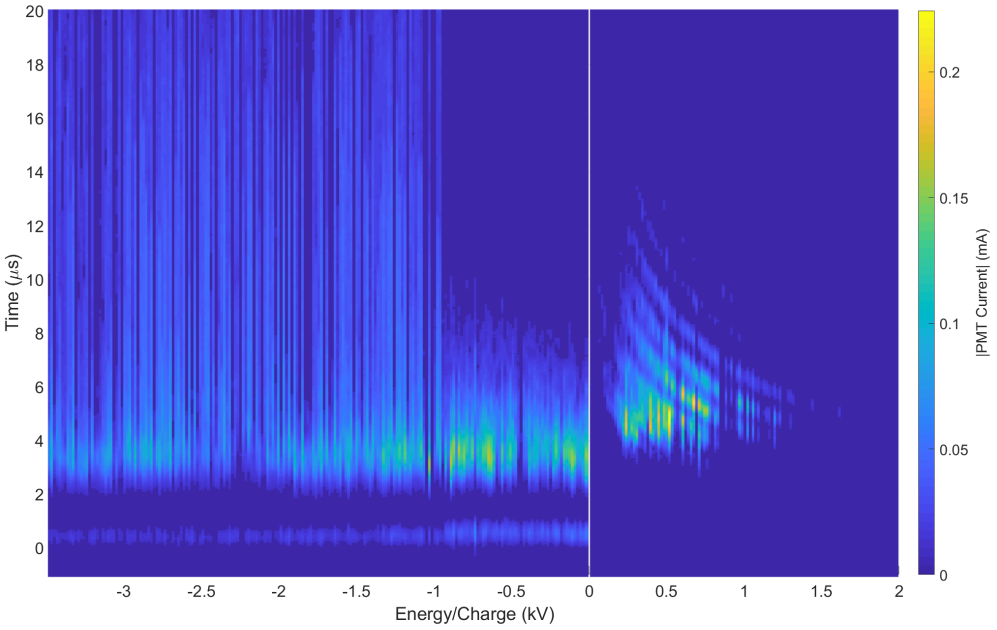

Figure 5.5: Photomultiplier output current vs. time for all energy sweeps. This plot shows the data after the 2.5% span Savitzky-Golay filter was applied.

The speed of the ions can be calculated from the flight time t_{tof}, and knowing

that the distance traveled L_{TOF} is 525 cm.

$$L_{TOF} = v\ t_{TOF} \tag{5.2}$$

In this paper, the $\sim$ symbol corresponds to variables that are per charge. Since the particle energy/charge $\widetilde{E}$ is known from the energy gate voltage and the particle speed is found from Equation 5.2, the mass/charge $\widetilde{m}$ is found from

$$\widetilde{E} = \frac{1}{2}\widetilde{m}v^2 \tag{5.3}$$

From this, the flight time of an ion of mass/charge $\widetilde{m}$ is a function of $\widetilde{E}$

$$t_{TOF} = L_{TOF}\sqrt{\frac{\widetilde{m}}{2\widetilde{E}}} \tag{5.4}$$

The decreasing concave up curves seen in Figure 5.5 therefore corresponds to constant mass/charge.

5.4.3 TOF-MS Signal vs. Mass/Charge

Augite pyroxene has a generic molecular formula (Ca,Na)(Mg,Fe,Al,Ti)(Si,Al)$_2$O$_6$ [117]. This can be composed of different combinations of atoms, such as $CaMgSi_2O_6$ or $NaFeSi_2O_6$. A variety of ions at various charge states get generated during ablation, so there is not enough information to reliably identify what ions are present.

The smoothed PMT output current is plotted vs. the ion mass/charge in Figure 5.6. Ions with mass/charge close to the peaks are shown, but this is not sufficient to conclude that the ions are accurately identified. From Figure 5.5 and

Figure 5.6, we see that the positive ion distribution has peaks at several mass/charge values, which is expected. The negative distribution had peaks at specific times as opposed to mass/charge values, the signal was not strongly dependent on the energy gate setting, and the signal took a long time to go to zero. Because the negative ion signal was poorly behaved, the remainder of this paper will analyze only the positive ions.

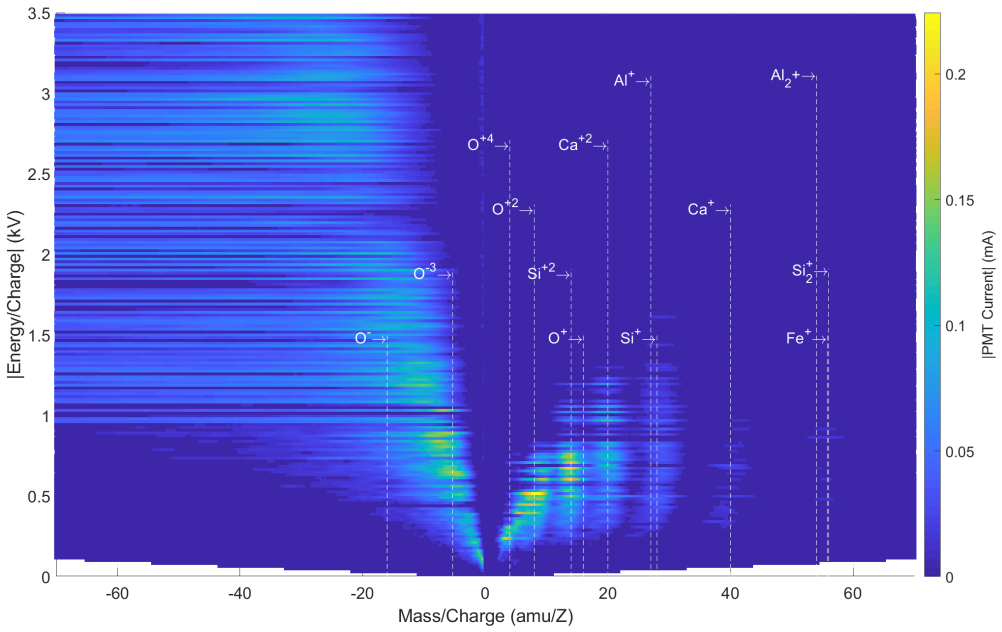

Figure 5.6: Photomultiplier output vs. energy/charge and mass/charge. Ions which may be present in the distribution are noted, but there is insufficient information to fully resolve the ion composition.

5.4.4 Integrated Photomultiplier Output

The smoothed currents (see Figure 5.4 for an example) are integrated over time for all positive energies to give the total PMT output charge as a function of particle energy/charge. This is shown in Figure 5.7. The peak energy in the positive

ions occurs at 505 V.

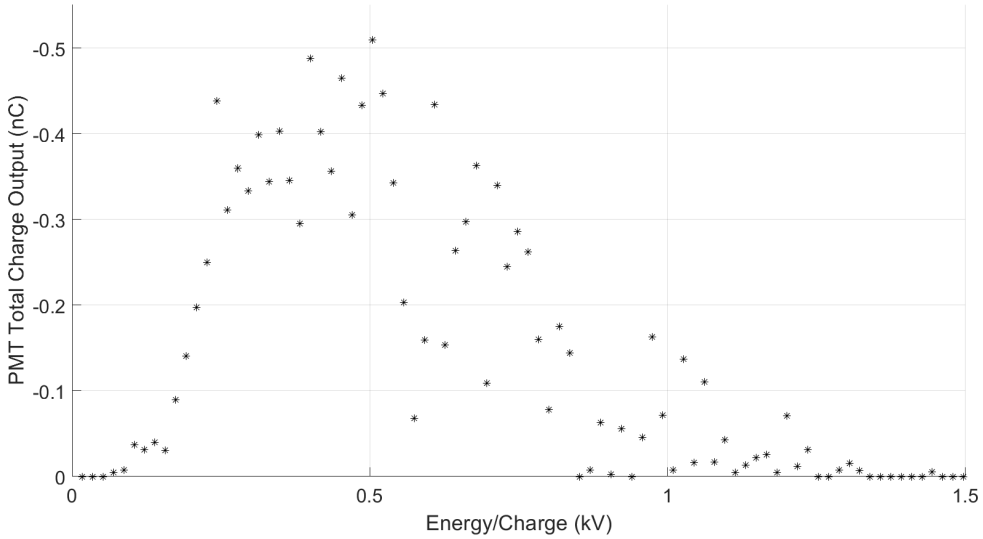

Figure 5.7: Total photomultiplier output charge vs. primary particle energy/charge.

5.4.5 2D Distribution Function vs. Mass/Charge and Speed

While Figure 5.6 provides an easy-to-understand view of the TOF-MS data, more care is required to properly calculate the distribution function. Consider the energy gates set to select particles of energy/charge $\widetilde{E}_0$. Let $M_t(\widetilde{E}_0, t)$ be the fraction of particles that enter the first energy gate who also reach the detector. When the pyroxene ions hit the aluminum wall on the detector, the detector emits secondary electrons. The secondary electron yield Y is the number of secondary electrons emitted per primary ion. It is dependent on the ion mass and velocity, as well as the interaction between the materials of the ion and the detector. The yield for ions present in pyroxene impinging on aluminum has not been analyzed by the authors, and even if this was done it would be difficult to uniquely identify which ions are present at each energy. In addition, the spectrometer is only able to resolve mass-

per-charge. The following functions for Y are considered in this paper as reasonable possibilities for the yield.

$$\begin{aligned} Proportional \qquad & Y \propto 1 \\ Momentum/Charge \qquad & Y \propto \widetilde{m}v \\ Energy/Charge \qquad & Y \propto \frac{1}{2}\widetilde{m}v^2 \end{aligned} \tag{5.5}$$

Since the distribution function will be reported in arbitrary units, the constants of proportionality in Equation 5.5 can be ignored. Additional constants of proportionality are similarly not needed, including the number of photons generated by scintillations per secondary electron, the amplification factor of the PMT, and the relation between the photon flow generated by the PMT and its output current. The effects of space charge within the spectrometer, as well as defocusing in the accelerator grid, are not considered in this paper, and left for future work.

As discussed in previous work [98], the 2D distribution function of the ions vs. energy/charge and flight time is given by

$$f_{\widetilde{E},t}(\widetilde{E}_0, t) = \frac{M_t(\widetilde{E}_0, t)}{\widetilde{E}_0 \cdot I} \cdot Y \tag{5.6}$$

where $I = 0.0523$ is a constant for this spectrometer. The secondary electron yield Y has been added here. By experimentally measuring M_t with the gate set to select a sweep of energies, the full 2D distribution $f_{\widetilde{E},t}$ is found.

We are now interested in calculating the 2D distribution as a function of mass/charge and speed, $f_{\widetilde{m},v}(\widetilde{m}, v)$. This is found by starting with the distribution

$f_{\widetilde{E},t}\ d\widetilde{E}\ dt$, and converting the differential elements.

$$f_{\widetilde{E},t}\left(\frac{1}{2}\widetilde{m}v^2, \frac{L_{TOF}}{v}\right) \cdot J \cdot d\widetilde{m}\ dv = f_{\widetilde{m},v}(\widetilde{m}, v)\ d\widetilde{m}\ dv \tag{5.7}$$

where J is the Jacobian determinant. J is calculated below, and the partial derivatives are calculated from Equations 5.2 and 5.3.

$$J = \begin{vmatrix} \frac{\partial \widetilde{E}}{\partial \widetilde{m}} & \frac{\partial \widetilde{E}}{\partial v} \\ \frac{\partial t}{\partial \widetilde{m}} & \frac{\partial t}{\partial v} \end{vmatrix} = \begin{vmatrix} \frac{1}{2}v^2 & \widetilde{m}v \\ 0 & -\frac{L_{TOF}}{v^2} \end{vmatrix} = \frac{L_{TOF}}{2} \tag{5.8}$$

Conveniently, the Jacobian determinant is found to be constant. For simplicity, let us normalize $f_{\widetilde{m},v}$ from Equation 5.7 to arbitrary units, define as $f^*_{\widetilde{m},v}\left(\widetilde{m}\left[\frac{amu}{Z}\right], v\left[\frac{km}{s}\right]\right)$. A scatter plot of $f^*_{\widetilde{m},v}$ calculated from the smoothed PMT data is shown in Figure 5.8(a). Each line in the scatter data corresponds to a single laser pulse, with the energy gate at a constant voltage.

The scatter data must now be converted to a mesh grid in order to be used for statistical analysis. The mesh grid is defined to have uniform boxes of size (0.5 amu x 1 km/s). For each box containing at least one data point from the scatter plot, the average value is used. The value used in boxes containing no data points are calculated using Matlab's built-in griddata() function, with cubic interpolation. Boxes outside the interpolation region are set to zero. The mesh grid data is shown in Figures 5.8b-d for the three functions for Y considered in Equation 5.5. Using the equations for Y proportional to the momentum or energy per charge weights the bottom-left region of the mesh grid. However, this does not appear to have a strong effect on the overall distribution.

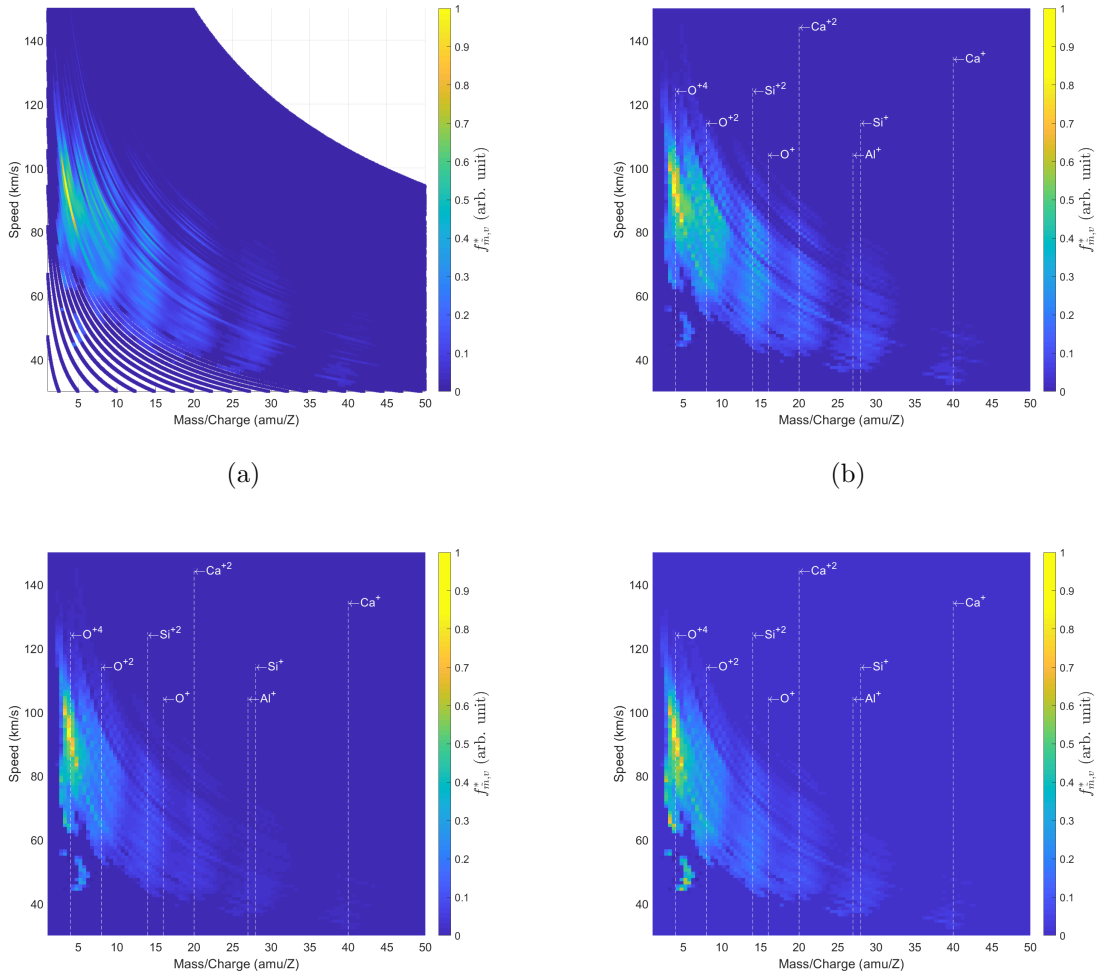

(a) (b)

(c) (d)

Figure 5.8: Normalized 2d distribution function of pyroxene positive primary ions. Several functions for secondary electron yield Y are considered. (a) Scatter plot ($Y = 1$); (b) Mesh grid ($Y = 1$); (c) Mesh grid ($Y = \widetilde{m}v$); (b) Mesh grid $\left(Y = \frac{1}{2}\widetilde{m}v^2\right)$.

5.4.6 Analysis of Distribution Function

The average velocity, weighted by $\widetilde{m}$, is given by

$$v_w = \frac{\langle \widetilde{m} v \rangle}{\langle \widetilde{m} \rangle} \tag{5.9}$$

Ideally, this would be weighted by m, but the mass is not fully resolved with this spectrometer. By dividing v_w by gravity on Earth, we get the specific impulse I_{sp}. Recall that this value is based only on the light, high-speed ions. As discussed in Pakhomov et al. [84], the I_{sp} found with TOF measurements is significantly higher than what is found using direct force measurements. This is because the TOF does not consider neutrals or nanoparticles.

These average values are calculated in Table 5.1. We see good agreement between the functions of Y used.

Table 5.1: Average values of mass/charge, speed, and specific impulse, for the pyroxene plasma distribution. Several functions for secondary electron yield (Y) are used in the calculation.

	$\langle \widetilde{m} \rangle$ (amu/Z)	v_w (km/s)	I_{sp} (s)
$Y = 1$	10.0	67.9	6920
$Y = \widetilde{m}v$	8.0	71.2	7260
$Y = \frac{1}{2}\widetilde{m}v^2$	9.0	66.5	6780

5.5 Conclusion

In this paper, a time-of-flight mass spectrometer (TOF-MS) was used to characterize the plasma plume resulting from pulsed laser ablation of pyroxene. The 2D distribution as a function of mass/charge and speed was found for the positive ions. From this, the specific impulse was found to be 6920 s. The overall specific impulse, considering losses from efficiency and slow moving macro-particles, is left for future work.

5.6 Acknowledgments

This material is based upon work supported by the National Science Foundation Graduate Research Fellowship Program under Grant No. DGE 1322106. This research is also supported by the Air Force Office of Scientific Research (AFOSR) under Federal Award No. FA9550-16-1-0193.

Chapter 6: Direct Force Measurements of Pulsed Laser Ablation of Asteroid Simulants

Sloane, J., and Sedwick, R., "Direct force measurement of pulsed laser ablation of asteroid simulants," *preprint*, 2019.

The following article is a pre-print. It has been submitted for consideration of publication to AIAA Journal of Propulsion and Power.

6.1 Abstract

Sub-nanosecond laser ablation of asteroid simulants has been studied, and direct force measurements were made. A 0.7 ns pulsed laser was used, with a 40 kHz pulse repetition frequency, 1064 nm wavelength, and 33 W average power. High fidelity simulants for carbonaceous chondrite meteorites of types CM, CR, and CI, as well as pyroxene rock and 6061 aluminum were ablated. The force response over 500 ms of ablation was measured using a load cell. In addition, the samples were weighed before and after ablation to determine the mass removal rate. Based on these measurements, the momentum coupling coefficient, specific impulse, and ablation efficiency were calculated. The asteroid analog materials were found to have a modestly higher momentum coupling coefficient than aluminum, although the specific impulse and efficiency were much lower. For asteroid mitigation missions, the asteroid itself is used as the propellant, so a low specific impulse poses no problem.

6.2 Nomenclature

C_m	Momentum coupling coefficient [mN·kW^{-1}]
f	Focal length of lens [m]
f_i	Ablation plume ionization fraction

F	Thrust from ablation [mN]
g_0	Standard gravity on Earth [9.81 m·s^{-2}]
ℓ	Distance from optimal focus along laser path [mm]
I_{sp}	Specific impulse [s]
k	Mechanical stiffness [N·m^{-1}]
m	Mass of sample [g]
$\dot{m}$	Mass removal rate [mg·s^{-1}]
P	Laser average power [W]
r, r_x, r_y	Laser radius at ℓ, magnitude, and x, z components [mm]
R	Laser radius at lens [mm]
t	Time since the beginning of the first laser pulse in a pulse train [ms]
v_e	Ablation plume average exhaust velocity [m·s^{-1}]
v_i	Average velocity of ions in the ablation plume [m·s^{-1}]
v_n	Average velocity of non-ions in the ablation plume [m·s^{-1}]
x, y, z	Sample position X, Y, Z components [mm]
η	Ablation efficiency. Ratio of ablation plume kinetic energy to deposited laser energy
η_p	Fraction of efficiency due to polydispersive
η_o	Efficiency, other than polydispersive
Φ	Laser fluence [J·cm^{-2}]

Φ_{thresh} Threshold fluence for ablation [J·cm^{-2}]

6.3 Introduction

The risk of an asteroid impacting Earth poses a unique threat. Like other natural disasters, an asteroid impact can cause significant loss of life and property damage. However, an asteroid on a collision course with Earth can be detected years or even decades before impact. This presents the opportunity to launch a spacecraft to deflect the asteroid off of an Earth threatening trajectory. If there is little time before a potential Earth impact (less than ∼5-10 years), then a high energy technique is required. If more time is available, low-thrust techniques can be utilized. These have the advantage of a potentially cheaper spacecraft, as well as more control of the final trajectory. Multiple low-thrust techniques have been proposed, including a gravity tug [30] and an ion-beam shepherd [118]. One particularly interesting technique is laser ablation. With this, a laser is fired at an asteroid from a nearby spacecraft. The asteroid material at the laser spot is ablated, which generates a directed plasma plume, thereby generating thrust. By ablating the asteroid material, propellant need not be launched with the spacecraft. Although some studies have been conducted on laser ablation of asteroids [51, 119], this is still a relatively open area of research. To this authors' knowledge, no force experiments have been conducted on asteroid materials using a pulsed laser, nor has the transient force response vs. time been measured. This paper reports direct force measurements of ablation from a 0.7 ns pulsed laser, conducted on high-fidelity CM, CR, and CI

asteroid simulants, as well as pyroxene rock and aluminum. Knowledge of the force response is critical to appropriately plan an asteroid deflection mission using laser ablation, in order to determine the size and required power of the laser.

Measuring thrust for electric propulsion techniques is challenging, because the thrust generated is small, especially compared to the weight of the thruster. For laser ablation, however, the laser does not need to be physically attached to the material being ablated. This reduces the mass that must be attached to a force measurement device, making the measurement easier. Several techniques have been used in the literature to determine thrust from ablation. Thrust can be inferred based on the speed of the ions in the plasma. The ion speed has been measured based on plasma temperature determined by emission spectra [31], high-speed camera measurements of plume expansion [83], and time-of-flight mass spectrometry (TOF-MS) [102,120–122]. However, these methods do not capture the effect of slow moving neutrals or other particles.

A more accurate approach is to take a direct force measurement. The most common method for electric propulsion is to use a pendulum or torque thrust stand [30]. This is also a common technique used in laser ablation [123], and has been used to measure the impulse bit from a single laser pulse [86,124]. The impulse of a single laser pulse must be large enough to be detectable, and the pulse width must be much shorter than the period of the pendulum. Continued ablation to the same spot on a sample degrades the force, making steady-state force measurements challenging. Another approach for measuring force generation is to use a piezo sensor [84].

In this paper, a commercial off-the-shelf (COTS) deci-Newton load cell is used

to measure the force from laser ablation. Although not sensitive enough to detect the impulse from a single pulse from the laser used in this paper, it can measure the force response over 500 ms of ablation. Another major benefit over impulse pendula is the ease of implementation of the measurement. The experimental setup presented herein also allows for multiple force measurements without needing to break vacuum. Technical challenges, including heating of the force sensor and alignment of the laser, are addressed.

6.4 Theory

The momentum coupling coefficient C_m is the thrust F generated by ablation divided by the average incident laser power P. For a single laser pulse, C_m is in general dependent on the material properties, the laser wavelength, the laser pulse width, and the laser fluence (energy per area) [33]. The overall ablation efficiency is η (Equation 6.2), $\dot{m}$ is the mass removal rate, and v_e is the average exhaust velocity. It is convenient to express the mass removal rate as a quantity per laser power $\left(\frac{\dot{m}}{P}\right)$ in the following equations. Normalizing the thrust equation by power gives

$$C_m = \left(\frac{\dot{m}}{P}\right) v_e \tag{6.1}$$

The ablation efficiency is defined as the particle plume power divided by the average laser power.

$$\eta = \frac{1}{2}\left(\frac{\dot{m}}{P}\right) v_e^2 \tag{6.2}$$

Noting that $v_e = I_{sp} g_0$ (where g_0 is gravity at the surface of the Earth), I_{sp} can be found by

$$I_{sp} = \frac{2\eta}{g_0 C_m} \tag{6.3}$$

There is therefore an inverse relationship between C_m and I_{sp} for a fixed ablation efficiency. For asteroid deflection, there is a virtually limitless amount of propellant available (namely, the asteroid itself), so a low I_{sp} is not a major concern, and C_m should be maximized. The fluence Φ is the energy of the laser pulse per area on the ablated surface. C_m is maximized when Φ is slightly above the ablation threshold Φ_{thresh} for a material [33]. Above this, additional fluence accelerates the plasma particles, increasing I_{sp} but reducing C_m. In this paper, C_m and $\dot{m}$ are determined experimentally. From the above equations, we find relations for η and v_e in terms of C_m and $\dot{m}$:

$$\eta = \frac{C_m^2}{2}\left(\frac{P}{\dot{m}}\right) \tag{6.4}$$

$$v_e = C_m\left(\frac{P}{\dot{m}}\right) \tag{6.5}$$

6.5 Experiment Setup

6.5.1 Laser

The laser ablation facility used for these experiments has previously been used for TOF-MS analysis of aluminum [98, 115] and pyroxene [109]. A 1064 nm laser (Photonics Industries model SN-1064-40) is used, which has a pulse width of 0.7 ns, energy of 827 μJ/pulse, 40 kHz pulse repetition frequency, and 33 W average power. The laser passes through an expander, after which it has a beam radius of approximately 15 mm. After this, it is focused by a lens to a point in the center of a vacuum chamber. The vacuum chamber has an operating pressure of 5 Torr. A diagram of the facility is shown in Figure 6.1.

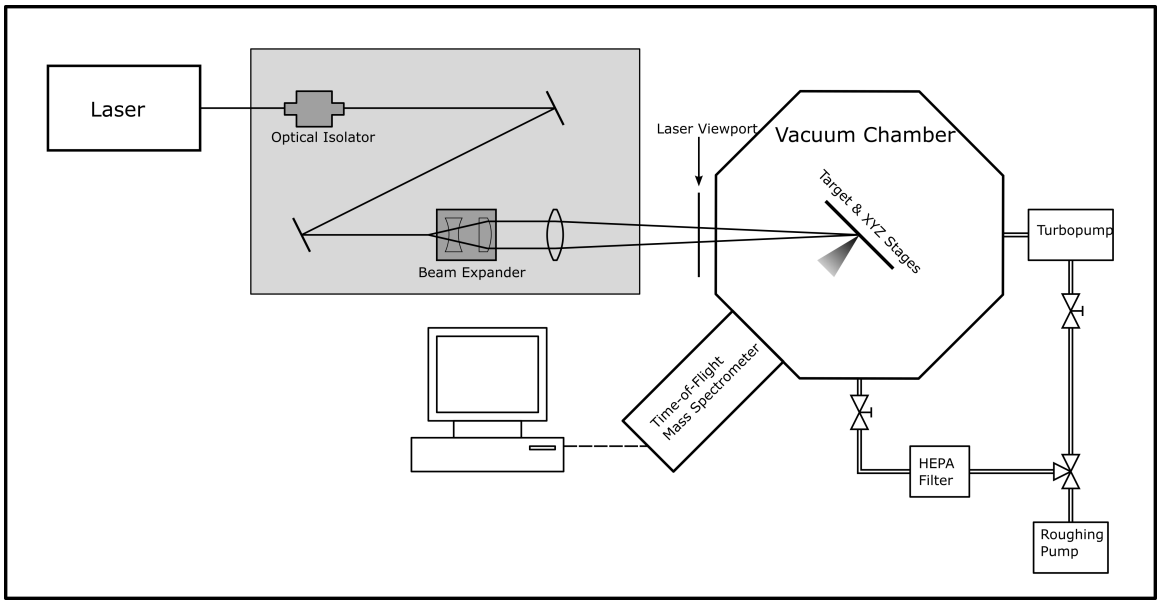

Figure 6.1: Schematic of laser ablation facility. Reproduced with permission from [98]: Sloane, J., Smith, E., and Sedwick, R., "Validation of a time-of-flight mass spectrometer using an ionic liquid ion source," *International Journal of Mass Spectrometry*, vol. 432, 2018, pp. 36-43. Copyright 2018, Elsevier.

6.5.2 Load Cell Assembly

For this experiment, a Novatech F329 Deci-Newton Loadcell and Novatec DSC USB load cell digitizer were used. Table 6.1 lists the load cell specifications. The laser pulse repetition frequency is 40 kHz, so there are 400 laser pulses between each data point.

Table 6.1: Load cell and digitizer specifications.

Range	0.1 N
Resolution	10 μN
Stiffness (k)	$1.3{\cdot}10^3$ N·m^{-1}
Maximum Torque	0.5 N·mm
Maximum Sample Mass	5 g
Natural Frequency	100 Hz
Sampling Rate	100 Hz

The load cell is mounted vertically to an aluminum back plate, with gravity in $-\hat{z}$, as shown in Figure 6.2. This plate is connected to translational stages, allowing for translation in the X, Y, and Z axes. The sample material to be ablated is attached to a screw, which is screwed into the force sensor. The laser's path is in the XY plane 45° to the sample surface, and the resulting ablation plume travels perpendicularly to the sample's surface (in the Y-axis). A guard plate is placed between the load cell and the sample to protect the load cell from the laser. Another aluminum plate is mounted flush to the sample surface and is used for alignment and focusing of the laser prior to force measurement experiments. The load cell measures force in the y-axis.

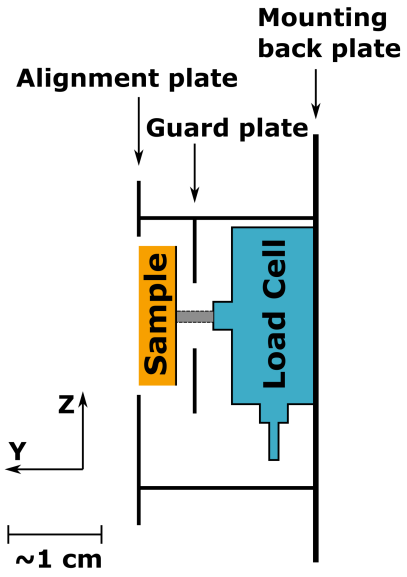

Figure 6.2: Load cell with sample material.

As part of the design of the experiments, we must determine that the load cell will not be damaged from heating, which can occur if the load cell exceeds 80 °C. For a simple, conservative model of the heat transfer, the pyroxene sample and screw are modeled using COMSOL Multiphysics. Both conduction and radiative cooling are modeled. The laser pulse is modeled as an instantaneous deposition of energy at the center of the surface of the sample. Firing the laser for one second results in heating the base of the screw from 21 °C (room temperature) to 55 °C. Based on this analysis, the laser is fired for 500 ms for the experiments, and the load cell is allowed to cool between experiments.

The raw load cell data are analyzed to determine how much time is required for the load cell to cool. The weight and resulting torque from the sample appears as a constant force offset. The laser fires for 500 ms, which is seen in the force vs. time figures as a spike in the force. Several seconds after the laser has fired, the measured

force starts to slowly decrease, and then slowly equilibrates to the pre-laser force. This long timescale change in the force is non-physical, and instead due to the heat from the laser propagating through the load cell. It is also easily distinguishable in the data from the force due to ablation. By requiring that the measured force equilibrates before firing the next laser pulse (∼10 min), we ensure heat does not build up on the load cell risking damage.

6.5.3 Samples

Force measurement experiments were conducted on five sample materials: aluminum, pyroxene, CM simulant, CR simulant, and CI simulant. 6061 aluminum with a mirror finish is used as a reference material. Aluminum is a commonly studied material in the literature [33, 102], and has been studied by the authors using TOF-MS [115]. Use of an elemental sample simplifies analysis of laser-material interaction [125]. In addition, the ions in the ablation plasma plume are all aluminum, so it is easier to identify the charge state of the ions. A thermal insulator (composed of pyroxene) is placed between the aluminum sample and the screw connecting the sample to the load cell.

Pyroxene is a common material found in asteroids, and is also found on Earth. It has been used previously in the literature as an asteroid analog [69]. For this study, a solid piece of augite pyroxene (Wards Science part #466472) is used. The sample was first cut to 3 mm thickness, with a length and width of 10 mm. The sample was then sanded, and cleaned with isopropyl alcohol. This material was also

analyzed using TOF-MS [109], so the direct force results can be compared to the TOF-MS results. The pyroxene and aluminum samples were attached to the screw using double sided carbon tape.

In response to the scientific community's need for high-fidelity lunar regolith simulants, NASA developed a Figure-of-Merit (FoM) to quantify how well the simulant matches with actual lunar regolith [126]. In 2015, NASA awarded Deep Space Industries (DSI) and the University of Central Florida (UCF) a contract to develop high fidelity asteroid regolith simulants [127]. A similar FoM has been developed for asteroid simulants, and an effort is ongoing to apply this FoM to the asteroid simulants. The simulants developed by UCF and DSI for CM, CR, and CI asteroids are used, and are respectively UCF/DSI-CM-2, UCF/DSI-CR-1, and UCF/DSI-CI-2 [128]. The samples were delivered as solid slabs with 6 mm thickness. The samples were quite brittle, and were able to be shaped to a 1 cm square by scoring. After shaping, the samples were sanded. Double sided tape did not stick to the simulant surfaces, so instead they were attached to the screw using a cyanoacrylate instant adhesive (Loctite model 495).

6.5.4 Laser Focusing

After installing the sample and load cell in the chamber, the laser focus must be aligned. To avoid overheating of the load cell, alignment was performed by firing on an aluminum plate flush with the sample surface. The position of the aluminum plate was adjusted for each sample to ensure it was flush with the surface, within

about 1 mm. Alignment is performed by finding the y-position (i.e. position normal to the sample surface) such that the minimum laser power is needed to achieve visible ablation. This is the optimal focusing, which corresponds to the maximum fluence achievable with this facility. Note that for some materials, C_m may be maximized using a lower fluence.

The sample position in the y-axis has a large effect on the laser intensity, as shown in Figure 6.3. Let us define $y = 0$ to be the sample position in the y-axis at optimal focusing. The laser is fired at the sample at a 45° angle with respect to the sample surface. The laser beam is Gaussian, and the e^{-2} radius R at the lens is 15 mm. The lens' focal length f is 0.5 m. The value of y corresponds to a distance along the laser path $\ell = y \cdot \cos(45°)$. The laser radius r is therefore

$$r = \frac{R}{f} \cdot \cos(45°) \cdot y = 42 \left[\frac{\mu m}{mm}\right] \cdot y \tag{6.6}$$

This is a good approximation for y > 0.5 mm with less than 10% error compared to the exact solution, and below which the radius flattens due to beam divergence. Note that the laser spot on the sample surface will actually be elliptical, with $r_z = r$, and $r_x = r/cos(45°)$.

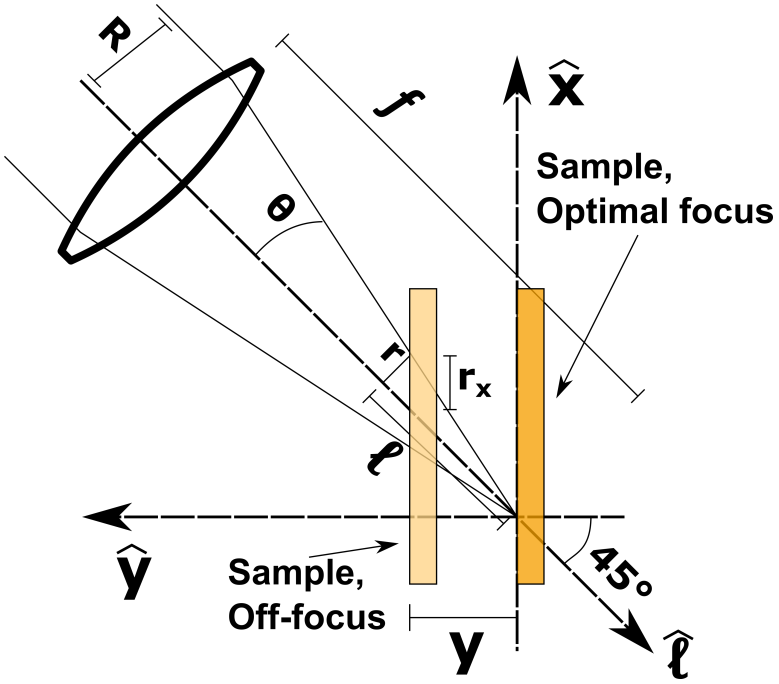

Figure 6.3: Top-down view of laser and sample. The intensity of the laser is strongly dependent on the sample position in the y-axis (relative to optimal focus).

The laser intensity is inversely proportional to the radius squared, so the intensity decreases significantly when the sample is out of focus, as shown in Figure 6.4. Due to the uncertainty in focus, we cannot reliably estimate the intensity of the laser during the ablation event. In addition, as the laser drills into a sample, the focus will change due to both the crater depth and the crater shape. The ablation response is strongly dependent on the laser fluence [33]. This presents the concern that the force experiments could be strongly affected by the y-position of the sample. To alleviate this concern, the force measurements were conducted across a range of y-positions, and the overall trends were analyzed.

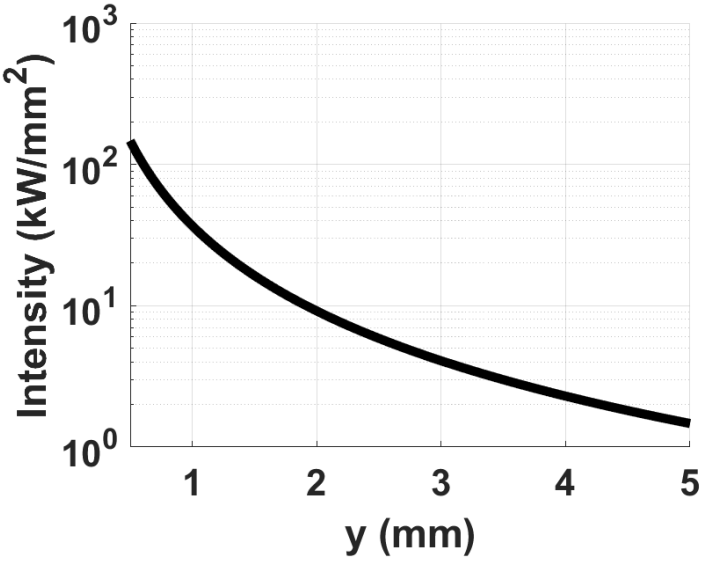

Figure 6.4: Laser intensity vs. sample offset from optimal focus in the y-axis.

6.6 Results and Discussion

6.6.1 Images of Samples During and After Ablation

Before performing an experiment, the sample was moved to a new ablation spot in the XZ plane. The sample was also moved to a desired position in the y-axis to adjust focusing. Since the laser was at a 45° angle from the sample, care was taken to ensure that the spot positions did not overlap between tests. The laser was then fired for 500 ms, and the force was measured using the load cell. The ablation event was also recorded using a webcam, positioned at a viewport outside of the vacuum chamber.

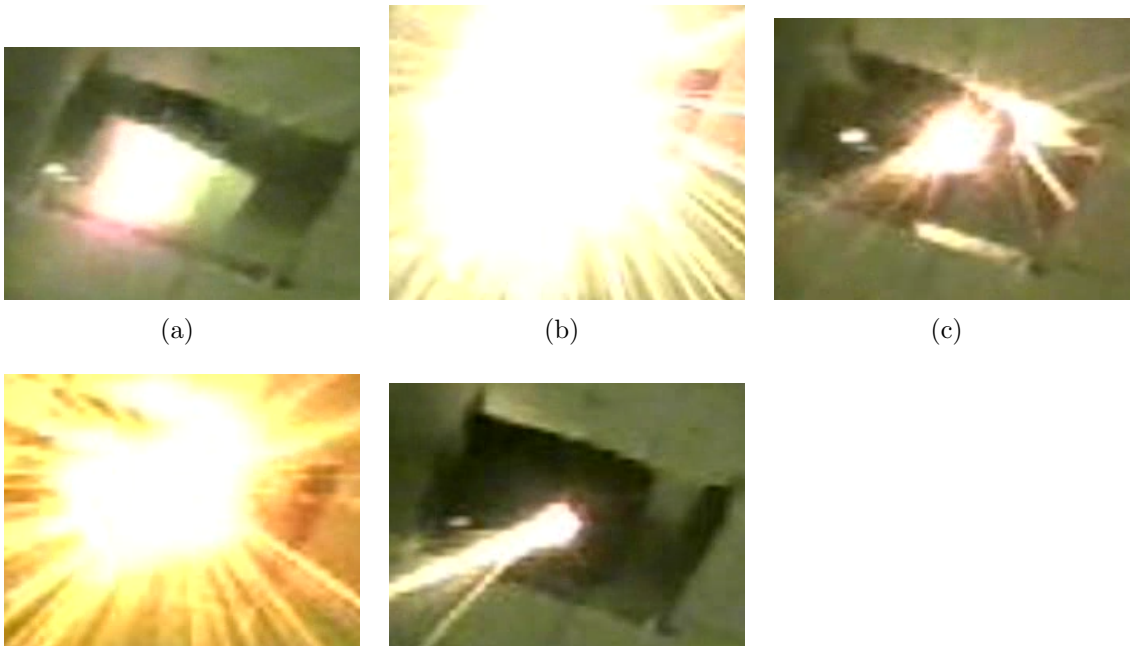

Figure 6.5: Frame from video taken during laser ablation direct force experiments. Samples are (a) aluminum; (b) pyroxene; (c) CM simulant; (d) CR simulant; (e) CI simulant.

Figure 6.5 shows an image frame taken in the middle of ablation experiments for each of the sample materials. Based on these images, aluminum has the weakest ablation. Although not seen here, ablation of aluminum was in some occasions seen to have a directed plume. The pyroxene and CR ablation event is very bright, and if the plasma plume is directed, it cannot be seen here. The CM and CI plasma plumes are strong, and clearly directed. Since the load cell measures the force component in the y-axis, the total force will likely be greater than what is reported in this paper. If the ablation plume is directed along the laser beam path, the measured force will be underestimated by a factor of $\sqrt{2}$.

The ablation plume from the first laser pulse has been observed to have a $cos^n(\theta)$ dependence, where θ is the angle with respect to the normal of the surface,

and n is dependent on the material and laser [116]. Angular spreading results in an efficiency loss. As the laser drills into the sample, it creates a hole that redirects the plume and may have nozzle-like effects. This can be seen clearly in the CM and CI plumes. The ablation plume can damage the spacecraft hosting the laser, especially its solar panels and laser optical components [129].

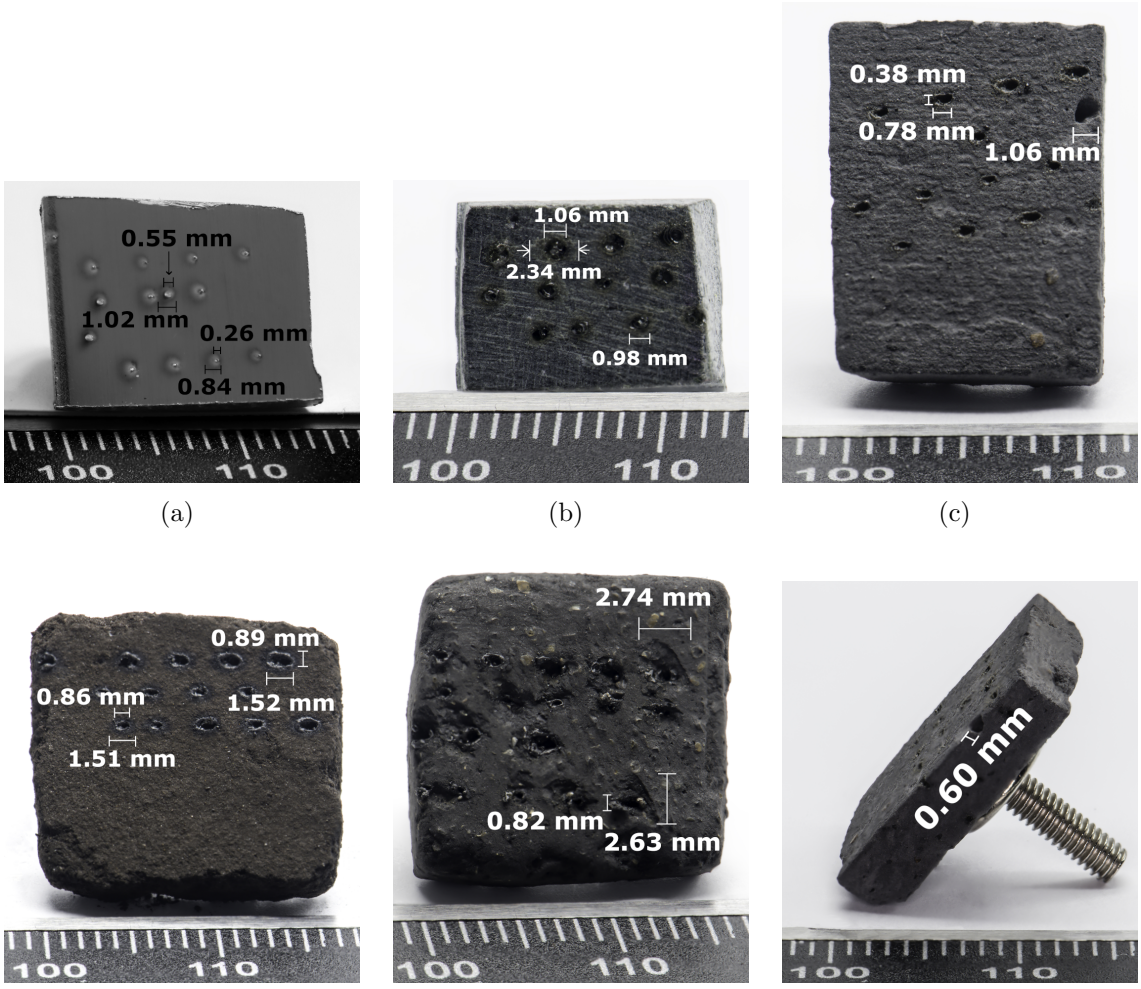

(a) (b) (c)

(d) (e) (f)

Figure 6.6: Samples after completion of laser ablation direct force experiments. Samples are (a) aluminum; (b) pyroxene; (c) CM simulant; (d) CR simulant; (e) CI simulant.

Figure 6.6 shows the samples after the experiments were completed. Recall

that each experiment was conducted at a range of distances from the laser focus, so the laser spot size was different at each ablation site. Surface absorbers, such as metals, have significantly less material removed from ablation per unit impulse, and correspondingly have a higher I_{sp}, compared to volume absorbers [33]. This explains the smaller craters in the aluminum sample. The CM simulant shows very little melting, relative to the other samples. Fortuitously, one of the laser spots (which has a 1.06 mm diameter) is on the edge of the sample. Looking at a side view of the CM simulant, we see the depth is at least 0.6 mm. The CR simulant had some discoloration around the crater. In addition, the width of the crater along the x-axis is larger than the width in the z-direction, as expected due to the 45° angle of the laser.

For all rock and simulant samples, the crater radius is significantly larger than the laser e^{-2} radius predicted by Equation 6.6, even accounting for several millimeters offset from optimal focusing. This suggests that misalignment with focusing may be less of a concern than previously anticipated. One possibility is that the ablation threshold for these materials is significantly lower than the fluence of the laser. Since the laser spot intensity is Gaussian distributed, the diameter of the portion of the laser large enough to cause ablation may be significantly larger than the typically reported beam radius (e^{-2}). Other possible contributions are heating, surface plasma, and repeated ablation of the same site. The larger crater size in the CM/CR/CI simulants compared to pyroxene is likely because the simulants are composed of powders that are loosely bound to each other, compared to the solid pyroxene rock. Therefore, the energy needed to remove material from the surface is

decreased. This would likely yield a higher thrust due to the higher mass flow rate. If some mass is removed without being accelerated significantly, that may show up as a loss mechanism.

6.6.2 Data Processing

In this section, an example of the data processing technique is shown for a single experiment case. The case used here is an aluminum sample, at optimal focusing position. To process the data, the time is offset such that the laser firing begins at $t = 0$. Then, the force is offset so the average force from -1000 ms to -50 ms is zero. The average force over 100 ms time ranges after $t = 0$ is calculated, as well as the average over 0-500 ms. These values are used in later summary plots. The standard error (SE) is also calculated, defined as the standard deviation divided by the square root of the number of data points used to calculate the average.

Repeated ablation of aluminum at the same spot is stable over approximately the first 40 pulses, after which a crater begins to form. The formation of a crater results in the degradation of the ablation strength [89]. Since 400 laser pulses occur between each data point, in aluminum the first 1-3 data points are typically significantly higher than the following points, and the confidence in these data points is lower. This was also seen to a lesser extent with the other samples. In addition, the force degrades most quickly over the first 100 ms for most samples. Because of this, the average force over the first 100 ms has a larger standard error than the other time ranges.

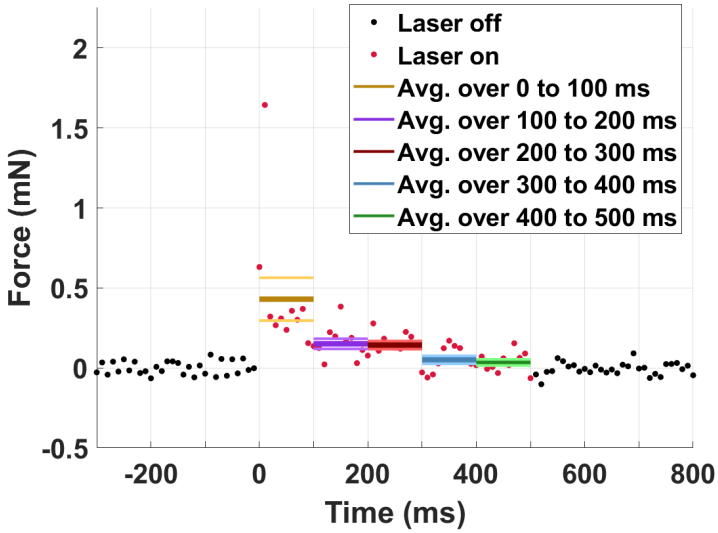

Figure 6.7: Processing of load cell data. Aluminum, optimal focus. Standard error shown in thinner, lighter colors.

Figure 6.7 shows the processing of the load cell data when the laser was fired. For comparison, Figure 6.8 shows a plot of the force vs. time of the CI simulant. This experiment case was performed with the simulant 1 mm offset from the optimal focus position in the y-axis. When the laser starts firing, the force instantaneously jumps up. It then degrades over 100 ms, and levels off. After 500 ms, the laser stops firing, and the force degrades over 50 ms back to zero.

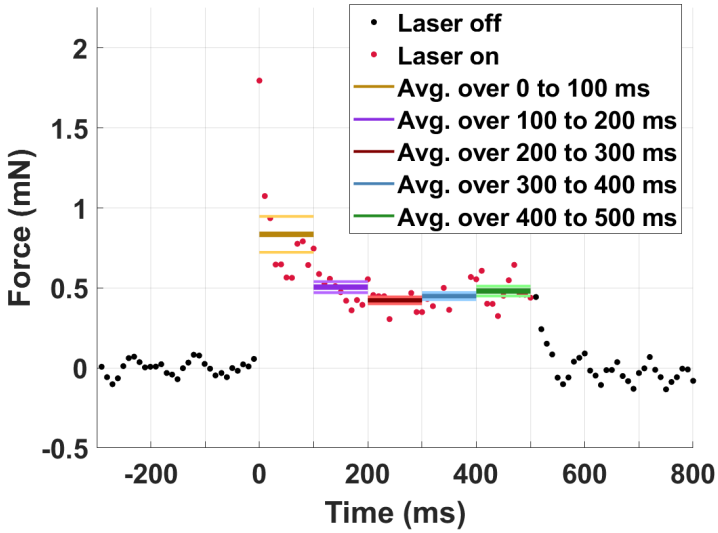

Figure 6.8: Example force vs. time of the CI simulant. Standard error shown in thinner, lighter colors.

6.6.3 Force vs. Y-Axis Position

To summarize the force vs. time data from all of the experiment cases, the average force is plotted vs. the y-axis position in Figure 6.9. Recall that the optimal focus is at $y = 0$, the position that maximizes fluence. Since C_m is a function of fluence, we expect the optimal fluence to correspond to either a maximum or a minimum for C_m. For aluminum, there is a clear trend where moving the sample off-focus results in a degraded force response. This is also seen in pyroxene, although it appears that the optimal focus was not perfectly aligned, and actually occurred at 1 mm. For the CM/CR/CI simulants, however, there is no apparent trend of focusing effecting the force. For a comparison of all materials on a single plot, see Figure 6.10.

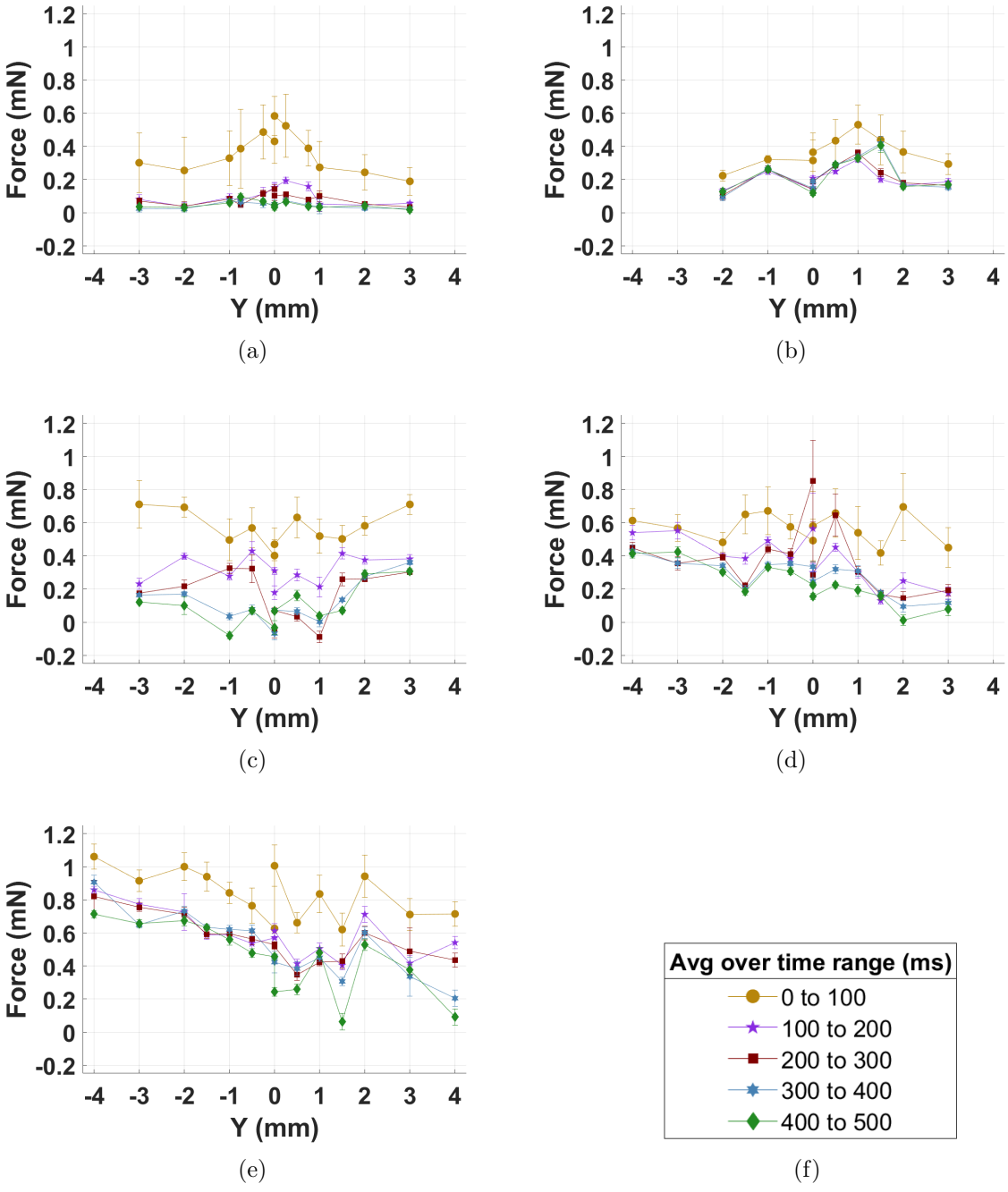

Figure 6.9: Average force vs. y-axis position. (a) Aluminum; (b) pyroxene; (c) CM simulant; (d) CR simulant; (e) CI simulant; (f) legend.

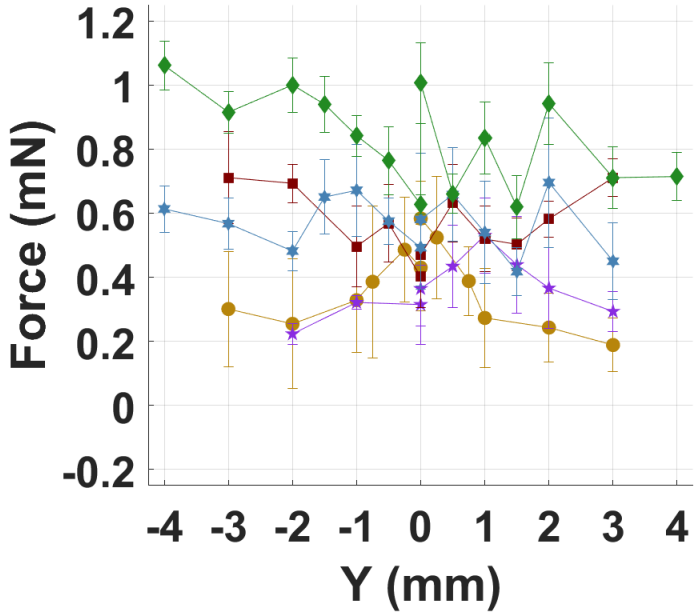

(a)

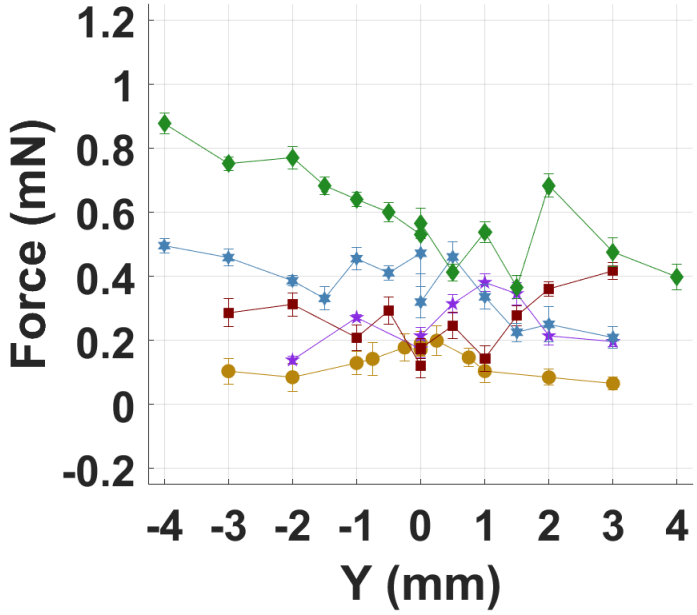

(b)

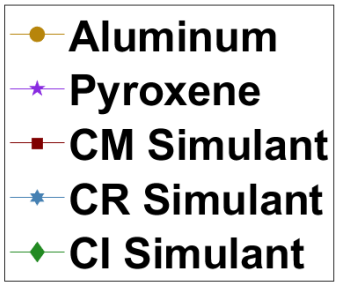

(c)

Figure 6.10: Average force vs. y-axis position. (a) Average over 0-100 ms. (b) Average over 0-500 ms. (c) Legend.

From these results, we see that the non-aluminum materials studied have a moderately higher C_m. In addition, the force ramps down more quickly for aluminum, as shown by Figure 6.9. Therefore, ablation of an asteroid at the same ablation spot can be sustained for longer than aluminum. This increases the fraction of the asteroid surface that can be used as propellant.

6.6.4 Momentum Coupling Coefficient

For each material, the maximum force from Figure 6.10 is identified, along with the standard error for that data point. This average was then divided by the average laser power (33 W) to calculate C_m, as summarized in Table 6.2. The CI simulant has the largest force response. The CR/CM/CI simulants have a larger force than pyroxene, and aluminum has the weakest force response when averaged over 500 ms.

Table 6.2: Momentum coupling coefficient.

Sample	C_m, $mN \cdot kW^{-1}$ *(Avg. over 0 - 100 ms)*	C_m, $mN \cdot kW^{-1}$ *(Avg. over 0 - 500 ms)*
Aluminum	17.8 ±3.6	6.0 ±1.4
Pyroxene	16.1 ±3.6	11.5 ±0.8
CM Simulant	21.5 ±4.4	12.6 ±0.8
CR Simulant	21.1 ±6.1	15.0 ±0.7
CI Simulant	32.1 ±2.3	26.6 ±1.0

6.6.5 Mass Removal Rate

To determine $\dot{m}$ for the CM/CR/CI asteroid simulants, a new set of samples was prepared. These samples were weighed using an Optima Scale (OPD-E204), which has an accuracy of 0.1 mg. Each sample was attached to a mounting plate, which in turn was attached to the XYZ translational stages in the vacuum chamber. Since the samples are not attached to the load cell, there is no concern about overheating, and less wait time was required between laser firings. The laser was fired at each sample for 500 ms per firing, for a total number of 18, 9, and 7 times for the CM, CR, and CI samples respectively. The number of laser firings used for each sample was limited by the available surface area of each simulant, as well as the crater size associated with each simulant. The ablation spots are spaced out to prevent overlapping craters, and all of the laser pulses are near the optimal focus. The samples are then weighed again post-ablation. The change in mass, divided by the total time that the laser was fired at the sample, is used to calculate $\dot{m}$. The values are summarized in Table 6.3, where $\dot{m}$ is normalized by the laser power.

The mass removal rates for ablation of aluminum and pyroxene were found to be significantly lower than for the asteroid simulants. Because of this, a slightly different approach was taken, to make sure enough mass is removed to be measurable. The laser is fired at a 20 x 20 x 4 mm slab of aluminum and pyroxene for 521 and 442 s respectively. During this time, the sample is moved in a raster motion, with the horizontal speed at 2 mm/s. Although this is different from the direct force measurements described earlier where the samples are stationary, the mass removal

rate should be comparable. The sample was weighed before and after the ablation experiment to determine the change in mass. Figure 6.11 shows the pyroxene sample post-ablation. The sample appears to show a significant amount of melting, and the ablated surface is raised slightly.

Figure 6.11: Pyroxene sample used for mass removal rate experiment.

6.6.6 Propulsion Parameters and Polydispersive Efficiency

With C_m and $\dot{m}$ known, η and I_{sp} are calculated using Equations 6.4 and 6.5. The C_m in this table uses the average value over 500 ms from Table 6.2. This is to be consistent with the mass removal measurements for the asteroid simulants, which used a 500 ms laser firing time. For a comparison to other electric propulsion technologies, consider the PPS-1350 Hall thruster. This has a nominal I_{sp} of 1700 s, η of 50%, power of 1.5 kW, and thrust-to-power ratio of 59 mN·kW^{-1} [130]. This corresponds to an $\left(\frac{\dot{m}}{P}\right)$ of 3.5·10^{-3} g·s^{-1}·kW^{-1}.

Table 6.3: Propulsion parameters.

Sample	C_m, $mN \cdot kW^{-1}$ *(Avg. over 0 - 500 ms)*	$\left(\frac{\dot{m}}{P}\right)$, g·s^{-1}·kW^{-1}	η	I_{sp}, s
Aluminum	6.0	$1.42 \cdot 10^{-4}$	12.85%	$4.3 \cdot 10^{3}$
Pyroxene	11.5	$1.24 \cdot 10^{-2}$	0.536%	95
CM Simulant	12.6	0.178	0.045%	7.3
CR Simulant	15.0	0.126	0.089%	12.1
CI Simulant	26.6	0.410	0.086%	6.6

The mass removal rate of aluminum is much lower than the other materials. Because of this, its I_{sp} is comparable to other electric propulsion technologies. For the other materials, the overall efficiency and I_{sp} are quite low. For practical applications, C_m is the driving consideration for performance of laser ablation of asteroids. A low I_{sp} corresponds to consuming a relatively large amount of propellant mass. However, since the asteroid itself is used as the propellant, there is a virtually limitless supply. In addition, only a small amount of Δv is required to deflect an asteroid from impacting Earth. In order to deflect an asteroid by one Earth radius, a Δv of only 1 cm·s^{-1} applied 10 years before impact is needed [13]. Assuming an I_{sp} of 10 s, only 0.01% of the asteroid mass is used. Even so, it is worth analyzing the cause of these low values, as it can be used to motivate improvements.

The ions generated from ablation are much faster than the heavier particles. This is a well-known phenomenon [84], and was a motivating factor for performing direct force measurements. The polydispersive efficiency is the propulsive efficiency

loss due to particles moving at different speeds, and has been studied for ionic liquid ion thrusters [90,96]. We will consider that effect here. For simplicity, consider that the ablation plume is composed of two groups: ions and non-ions. The non-ions include neutrals, nanoparticles, and macro-particles. The subscript i is used for ions, and n for non-ions. We will assume that all particles in each group are traveling at the same speed. However, it is likely that a large fraction of the mass is dislodged from the surface but not accelerated, which would act as a mass loss mechanism. Upon the completion of the experiments, several large grains (about 0.1-1 mm) were observed in the vacuum chamber, supporting that idea.

Let f_i be the fraction of $\dot{m}$ composed by the ions. The total C_m from Equation 6.1 equals the sum of the C_m from the two particle groups. The weighted average exhaust velocity v_e is therefore

$$v_e = f_i \, v_i + (1 - f_i) \, v_n \tag{6.7}$$

Since the ions are moving faster than v_e, the non-ions must therefore be moving slower. The polydispersive efficiency is the effective plume power divided by the weighted average plume power

$$\eta_p = \frac{\frac{1}{2}\dot{m} v_e^2}{\frac{1}{2}\dot{m} \left(f_i v_i^2 + (1 - f_i) \, v_n^2 \right)} \tag{6.8}$$

Let $\tilde{v} = v_n / v_i$. Substituting Equation 6.7 into Equation 6.8 and simplifying gives

$$\eta_p = \frac{\left[f_i + (1 - f_i)\,\tilde{v}\right]^2}{f_i + (1 - f_i)\,\tilde{v}^2} \tag{6.9}$$

Since η is the overall ablation efficiency, we can define η_o to be the efficiency due to all other causes, so

$$\eta = \eta_p \cdot \eta_o \tag{6.10}$$

Other sources of efficiency loss include heating the surrounding sample material, angular spreading of the plume, and energy required for phase change.

Let us consider the ablation of pyroxene. Using the TOF-MS described in [98], the I_{sp} of the pyroxene ablation ions was found to be 6920 s ($v_i = 67.9$ km·s^{-1}) [109]. This is much larger than the overall I_{sp} in Table 6.3. Equation 6.7 is used to get v_n in terms of f_i. Figure 6.12 shows several variables of interest as a function of f_i for pyroxene.

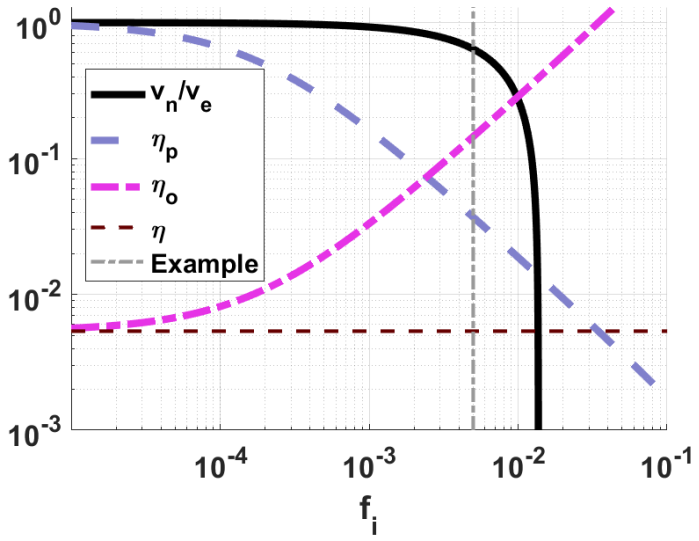

Figure 6.12: Polydispersive Efficiency for Ablation of Pyroxene.

η_p must be greater than η, and v_n must be greater than zero. This constrains f_i to be less than $1.4{\cdot}10^{-2}$ for pyroxene. For an example calculation, let us consider $f_i = 5{\cdot}10^{-3}$, which is marked in the figure. This gives $\eta_p = 3.7\%$, and $\eta_o = 15\%$. In addition, the ions contribute 37% of the thrust, but contain 98.5% of the kinetic energy. This supports the hypothesis that η_p may be the driver of the efficiency loss. For another extreme example, consider v_n=0, where the non-ions are dislodged from the sample but do not have any significant velocity. In this case, the ions contribute all of the thrust and contain all of the kinetic energy, and $\eta_p = f_i$ (from Equation 6.9). This can alternatively be thought of as an efficiency loss associated with extra mass removal that does not contribute thrust.

The polydispersive efficiency can be improved by either decreasing the speed of the ions, or increasing the speed of the non-ions. As shown in Equation 6.4, the high I_{sp} of the ions comes at a cost of low C_m. An electrostatic deceleration stage could be used to slow the ions, and the recovered energy would then be available for additional ablation. However, this would add significant operational complexity, since the spacecraft would need to land on the asteroid. Increasing the speed of the non-ions would improve the polydispersive efficiency, and therefore increase both I_{sp} and C_m significantly. These particles could be ionized and fed into an electrostatic thruster, but this would have similar issues as an ion deceleration stage. Before considering these concepts, future work should instead study the effect of laser parameters (pulse width and fluence) on the propulsion parameters. Specifically, the threshold fluence should be determined experimentally, as the optimal fluence for maximizing thrust is on that order. Other methods, such as using a second laser

pulse in rapid succession to the first to further ionize or heat the plasma plume, can also be considered.

6.7 Conclusion

Ablation of asteroids can be used to deflect an asteroid on an Earth threatening trajectory. In this paper, direct force measurements of laser ablation of asteroid simulants has been presented. A commercial off-the-shelf (COTS) deci-Newton load cell was used to make the force measurements. Although the load cell is unable to resolve the impulse from individual laser pulses, it measures the transient force-response resulting from surface heating and crater development. Force measurements were conducted at a range of laser focusing conditions, to quantify the effect of de-focusing on the thrust generated. In addition, the mass removal rate per power was found.

The asteroid analog materials include monolithic pyroxene rock and high-fidelity CM/CR/CI asteroid simulants. In addition, 6061 aluminum was measured to provide an example of a more commonly studied material. The momentum coupling coefficient, averaged over the 500 ms of ablation, was found to be between 6 and 27 $\mathrm{mN{\cdot}kW^{-1}}$ for all of the materials tested.

To determine the mass removal rate due to ablation, the samples were weighed before and after ablating for a known amount of time. The mass removal rate per power of the CM/CR/CI simulants were 0.178, 0.126, and 0.410 $\mathrm{g{\cdot}s^{-1}{\cdot}kW^{-1}}$, respectively. This is much higher than the mass removal rate per power for aluminum

and pyroxene, which were $1.42{\cdot}10^{-4}$ and $1.24{\cdot}10^{-2}$ $g{\cdot}s^{-1}{\cdot}kW^{-1}$ respectively. The higher mass removal rate for the simulants contributes to their higher momentum coupling coefficient, as well as the lower efficiency. Polydispersive efficiency was found to be a likely driver of the overall efficiency, i.e. that the average particle speed is orders of magnitude slower than the ion speed. The higher mass removal rate for the asteroid simulants is not a major concern by itself for asteroid mitigation or redirection, since there is a virtually unlimited amount of propellant available from the asteroid itself, although it does offer insight into how the performance can be improved. Therefore, based on these experiments asteroid materials are a good propellant material for laser ablation propulsion, especially if propellant mass is not a concern (such as ablation of asteroids for asteroid redirection). Future work can include optimizing laser parameters, and improving the utilization of the non-ionized and slower moving particles.

The thrust-to-power ratio of laser ablation is somewhat lower than other electric propulsion thrusters, such as the PPS-1350 Hall thruster. However, laser ablation has other benefits, chiefly being that it does not need to bring propellant for the asteroid redirection (aside from maneuvering the spacecraft itself), and it can impart force on the asteroid without physically contacting it.

6.8 Acknowledgments

The authors would like to thank Deep Space Industries and the University of Central Florida for providing the high fidelity meteorite simulants. This material is

based upon work supported by the National Science Foundation Graduate Research Fellowship Program under Grant No. DGE 1322106. This research is also supported by the Air Force Office of Scientific Research (AFOSR) under Federal Award No. FA9550-16-1-0193.

Chapter 7: System Level Analysis of Asteroid Mitigation Mission

7.1 Overview

System level analysis for asteroid mitigation has been conducted in the literature. These analyses typically focus on trajectory design, as well as the required thrust. For example, [118] analyzed deflection of asteroids 2007 VK_{184} and 2011 AG_5, which have diameters of 130 m and 140 m respectively. In both cases, applying 1 N of constant tangential force for two years, starting ten years before impact, was found to deflect the asteroids by more than two Earth radii. This analysis also compared the total impulse per spacecraft mass between the ion beam shepherd concept and the gravity tractor concept, and found that the ion beam shepherd performed significantly better.

In [14], orbit maneuver optimization was performed, and found that the required Δv for an asteroid deflection maneuver is lower when performed at perihelion. [16] considered maneuver optimization for both impulsive and continuous deflection.

The analysis required for asteroid mitigation is similar regardless of what deflection technology is considered, since much of the work is on the required thrust and orbit, as opposed to how the thrust is generated. Each technology does have

unique aspects that must be accounted for in the optimization design. For some technologies, such as solar concentrators and ALP, additional spacecraft propellant is not needed for the deflection maneuver. Therefore, force can be applied for a longer time with minimal additional cost. Analysis for asteroid mitigation using ALP has been conducted by [15, 112, 131].

In this chapter, the performance of ALP is considered. Because similar analysis has been conducted in the literature using high-fidelity models on specific asteroid cases, this analysis will use approximations in order to be more general and allow for a quick comparison of technologies. For spacecraft optimization, the main difference between ALP and other electric propulsion technologies is that ALP of asteroids has a lower thrust-to-power ratio, but does not consume propellant. In this chapter, the required spacecraft mass of ALP based on propulsion parameters from chapter 6 is compared to a Hall thruster in more detail. For simplicity and generality, only the mass of the solar panels, and the propellant mass (for the Hall thruster) are considered. Additional considerations, including the mass of the thruster, the laser's efficiency, and the need for a second thruster of equal force to maintain the spacecraft position for the ion beam shepherd method, are not taken into account. In this chapter, let C_m refer to the thrust-to-power ratio for both ALP and the Hall thruster. For laser ablation, this is called the momentum coupling coefficient. Table 7.1 shows performance parameters for ALP of asteroids, and the PPS 1350 Hall thruster from [130]. The C_m value used for ALP here is conservative, and the values from chapter 6 are as much as three times larger, depending on the material.

Table 7.1: Performance parameters.

	Thrust-to-power ratio (C_m), $mN \cdot kW^{-1}$	Propellant mass consumption rate per power ($\dot{m}_{prop}/P$), $mg \cdot s^{-1} \cdot kW^{-1}$
Laser Ablation	10	0
PPS 1350-G Hall Thruster	59	3.5

7.2 Required Force and Time To Deflect an Asteroid

As discussed in chapter 2, there is a 3x amplification factor in asteroid deflection when thrust is applied along the velocity vector. This approximation is generalized for low-thrust here. The total deflection of an asteroid can be approximated by

$$\int \frac{1}{3}\frac{F}{m_a} t \cdot dt = \Delta x \tag{7.1}$$

where t is the time before impact, F is the thrust, m_a is the asteroid mass, and Δx is the total deflection. Recall that $F = C_m \cdot P$. For a constant thrust applied between times t_0 and t_f, the deflection per power is

$$\frac{1}{6}\frac{C_m}{m_a}\left(t_0^2 - t_f^2\right) = \frac{\Delta x}{P} \tag{7.2}$$

Figure 7.1 shows the asteroid diameter that will be deflected by one Earth radius as a function of force and t_0. This assumes a spherical asteroid with 2 $g \cdot cm^{-3}$ density.

Figure 7.1(a) considers the force applied continuously up to impact, and Figure 7.1(b) considers the force applied for the first two years. For comparison, the solar panels on the Dawn spacecraft generate 10 kW at 1 AU [132], and the International Space Station's solar panels generate up to 120 kW [133]. Also, the Dawn spacecraft has 747.1 kg dry mass (including 126 kg solar panels), 425 kg xenon propellant, and 45.6 kg hydrazine propellant [132].

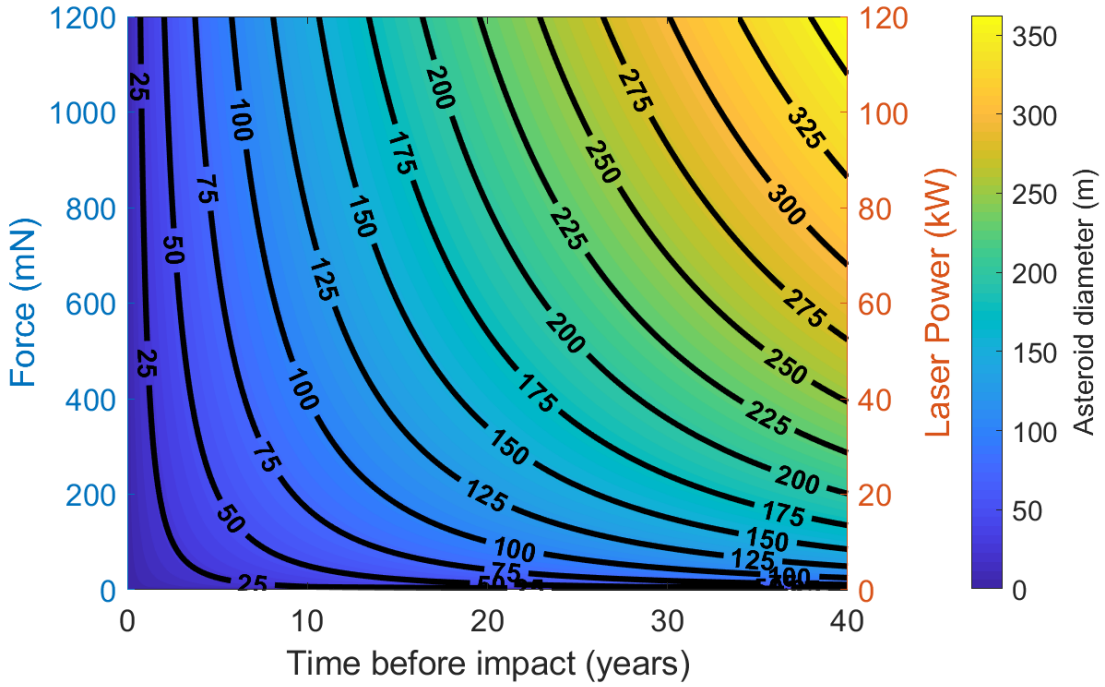

(a)

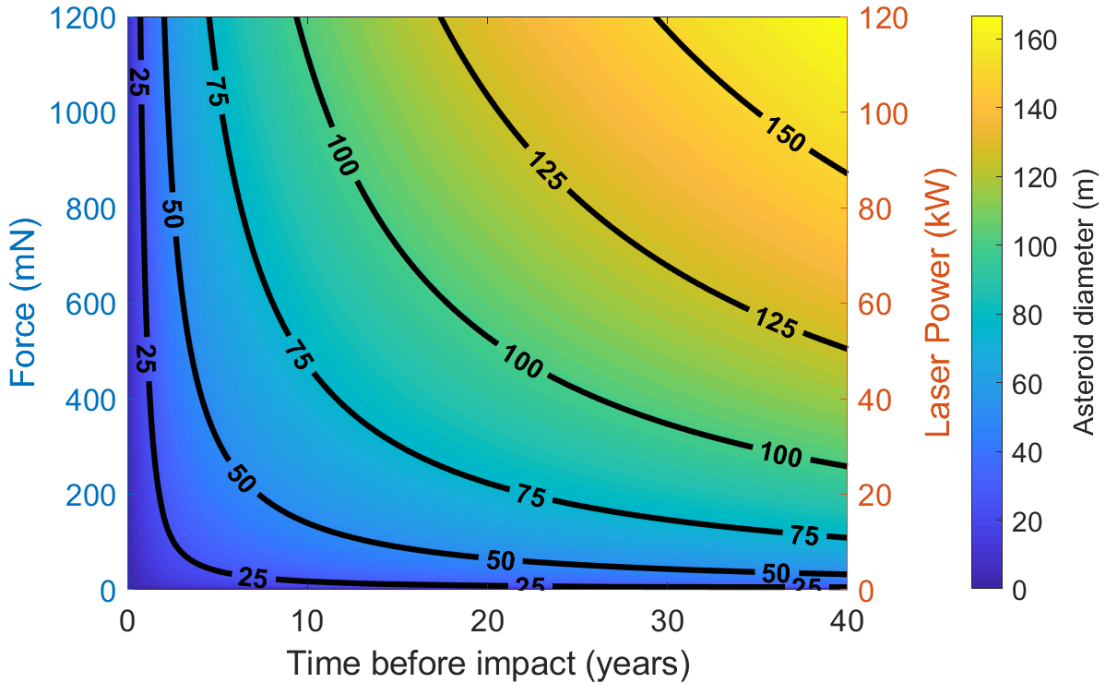

(b)

Figure 7.1: Asteroid diameter deflected by $R_{\oplus}$. Spherical asteroid with 2 $kg \cdot cm^{-3}$. The laser power required to generate this thrust is shown, given $C_m = 10\ mN \cdot kW^{-1}$. Force is applied: (a) continuously until impact; (b) for the first two years.

7.3 Comparing ALP to Hall Thruster

According to [134], the state-of-the-art specific power for solar arrays $P_{sp,solar}$ at 1 AU at beginning of life are 80 $W \cdot kg^{-1}$ and 150 $W \cdot kg^{-1}$ for deployable rigid arrays, and flexible arrays respectively. In this chapter, we will use $P_{sp,solar} = 80\ W \cdot kg^{-1}$. The required solar panel mass per thrust F is

$$\frac{m_{solar}}{F} = (C_m \cdot P_{sp,solar})^{-1} \tag{7.3}$$

For a thrust applied for a total time τ, the required propellant mass per thrust is

$$\frac{m_{prop}}{F} = \left(\frac{\dot{m}}{P}\right) \cdot \left(\frac{1}{C_m}\right) \cdot \tau \tag{7.4}$$

The total mass of interest per thrust is therefore

$$\frac{m_{total}}{F} = \frac{m_{solar}}{F} + \frac{m_{prop}}{F} \tag{7.5}$$

Equations 7.3 and 7.4 are combined to give the total mass of interest per thrust (m_{total}/F). Since ALP does not consume propellant mass on board the spacecraft during the maneuver, note that $m_{prop,laser}$ is zero, and $m_{total,laser}$ is not dependent on τ. Figure 7.2 shows the ratio of the total mass for laser ablation and for a Hall thruster as a function of τ, for both thrusters generating equal force. When the total thrust time is greater than 0.55 years, the laser ablation thruster has lower total mass than the Hall thruster. For τ of two years (as in 7.1(b)), the laser total

mass is 30% of Hall thruster's mass, and by five years it is an order of magnitude smaller.

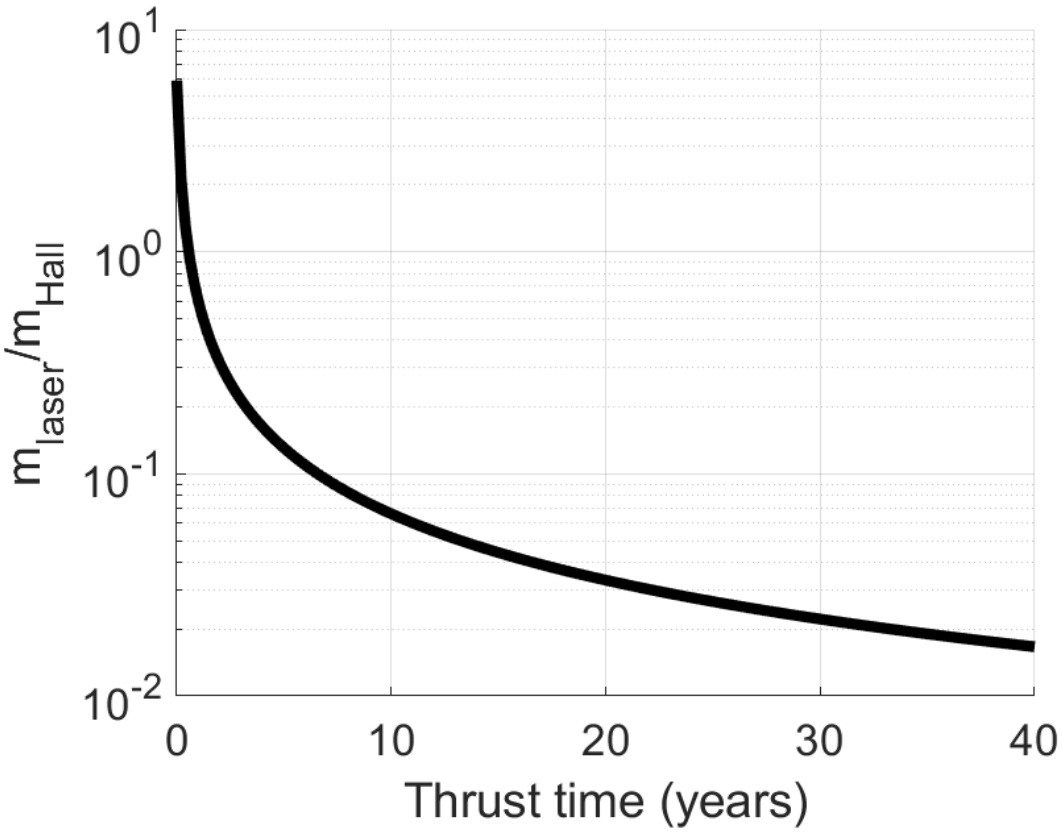

Figure 7.2: Ratio of total mass (solar panel + propellant) for a laser ablation thruster of asteroids to the PPS 1350 Hall thruster. This considers both thrusters generating equal thrust.

Chapter 8: Conclusions and Future Work

8.1 Summary of Results and Contributions

In this thesis, ablative laser propulsion (ALP) of asteroid analogs is studied. A 1064 nm laser with a 0.7 ns pulse width, 827 μJ per pulse, 33 W average power, and 40 kHz pulse repetition frequency is used.

In chapters 3-4, the design of a time-of-flight mass spectrometer (TOF-MS) is introduced. This spectrometer is equipped with orthogonal acceleration energy gates. The gates are a modified Herzog shunt design, to ensure that the electric field is uniform along the charged particle's trajectory. The energy gates select particles with an energy-per-charge of -3.48x the voltage on the gates. By sweeping through the energy gate voltage during an experiment campaign, the two-dimensional distribution as a function of mass-per-charge and speed can be found for ions in an ablation plume. This design has several differences and advantages to to the popular reflectron mass spectrometer design. A reflectron spectrometer must fully decelerate the charged particles, so the maximum particle energy per charge is equal to the maximum voltage applied. In addition, the reflectron can more accurately measure the mass-per-charge distribution, but at a cost of not measuring the particle speed. The speed distribution is of greater interest than the mass-per-charge distribution

in this thesis, since we are interested in the specific impulse of the plume. The mass spectrometer design is validated using an ionic liquid ion source, which generates ions of known energy-per-charge.

In chapter 5, the TOF-MS is used to analyze the plasma plume resulting from ablation of pyroxene. The 1D distribution vs. energy-per-charge is first found, and the peak occurs near 500 kV. Then, the 2D distribution vs. mass-per-charge and speed is found for the positive ions. Several bands of mass-per-charge in the distribution are identified as possible ions from pyroxene. The peak in the 2D distribution occurs near a mass-per-charge of 4 $amu \cdot Z^{-1}$ and speed of 90 $km \cdot s^{-1}$. The average ion speed, weighted by the mass-per-charge, is calculated. From this, the specific impulse of the positive ions is found to be 6920 s. Since this only considers the high-energy ions, it is an over-approximation of the overall specific impulse of the ablation plume.

In chapter 6, the force from ablation is measured using a load cell. The load cell has a 10 μN sensitivity, 100 Hz natural frequency, and 100 Hz sampling rate. The laser is fired for 500 ms at a 40 kHz pulse repetition frequency. The laser was not fired for longer, to avoid damaging the load cell by overheating. These experiments were conducted on aluminum, pyroxene, and simulants for CM, CR, and CI meteorites. The high-fidelity simulants for the CM, CR, and CI meteorites are UCF/DSI-CM-2, UCF/DSI-CR-1, UCF/DSI-CI2, respectively. The force vs. time for aluminum degraded quickly, as expected from the literature. This was seen to a much lesser extent with the asteroid analogs, and in some experiments the force leveled off. This shows that there is less need to maintain a fresh ablation spot

when ablating asteroid materials compared to aluminum, which will make asteroid deflection maneuvers easier to implement. The laser focusing was varied, and by that the effect of the laser fluence on the force generated was found. For aluminum and pyroxene, the force is maximized when the laser is the most tightly focused. This trend was not seen with the simulants. The momentum coupling coefficient C_m (force-per-power) averaged over the first 500 ms of ablation was then calculated. The mass removal rate per power was then found by weighing the samples before and after ablating for a known amount of time. These two propulsion parameters were used to calculate the ablation efficiency η and the specific impulse I_{sp}. The table summarizing these propulsion parameters is shown here. The overall I_{sp} for pyroxene found from the direct force measurements is much lower than the I_{sp} for the high-energy ions found with the TOF-MS. This is likely due to slow moving large particles, or mass that is dislodged without being accelerated.

Table 8.1: Propulsion parameters. Reproduced from [Table 6.3; Sloane, J., and Sedwick, R., "Direct force measurements of pulsed laser ablation of asteroid simulants," *preprint*, 2019].

Sample	C_m, $mN \cdot kW^{-1}$ *(Avg. over 0 - 500 ms)*	$\frac{\dot{m}}{P}$, $g \cdot s^{-1} \cdot kW^{-1}$	η	I_{sp}, s
Aluminum	6.0	$1.42 \cdot 10^{-4}$	12.85 %	$4.3 \cdot 10^{3}$
Pyroxene	11.5	$1.24 \cdot 10^{-2}$	0.536 %	95
CM Simulant	12.6	0.178	0.045 %	7.3
CR Simulant	15.0	0.126	0.089 %	12.1
CI Simulant	26.6	0.410	0.086 %	6.6

In chapter 7, Table 6.3 (reproduced in Table 8.1) is used to conduct trade studies and system level analysis. Although the I_{sp} for ALP of the asteroid simulants is very low, only a small Δv is needed for an asteroid mitigation maneuver. In order to deflect an asteroid by one Earth radius, a Δv of only 1 $cm \cdot s^{-1}$ applied 10 years before impact is needed. Assuming an I_{sp} of 10 s, this uses only 0.01% of the asteroid mass. ALP with a representative C_m of 10 $mN \cdot kW^{-1}$ is considered. A trade study of applied force vs. time before impact is conducted. For example, a 5.5 kW laser thrusting continuously starting 10 years before impact would deflect a 50 m diameter asteroid by one Earth radius. ALP is then compared to the PPS 1350-G Hall thruster, which has a thrust-to-power ratio of 59 $mN \cdot kW^{-1}$, and a propellant mass consumption rate per power of 3.5 $mg \cdot s^{-1} \cdot kW^{-1}$. The total mass (solar panel + propellant) is compared for the two thrusters generating equal thrust. Since ALP does not require spacecraft propellant, it has an advantage for longer thrust times. When the total thrust time is greater than 0.55 years, the required mass for ALP is smaller, and by five years it is an order of magnitude smaller. Therefore, for certain mission designs, ALP can have a dramatic mass savings.

8.2 Recommended Future Work

8.2.1 Improving Propulsion Parameters

In the direct force measurements conducted in this thesis, the laser fluence was varied somewhat, since the fluence could not be set or measured with high precision. In future work, the effect of fluence on C_m should be studied in more detail. The

threshold fluence, which is the minimum fluence required to generate ablation, can be found for each asteroid simulant. This likely occurs at a significantly lower fluence than what was used in this thesis. C_m is maximized near the threshold fluence, so this might lead to improved performance.

Another source of improvement is with the low specific impulse from laser ablation of the simulants, due to slow moving neutrals/macro-particles. A different laser pulse width may help alleviate this issue. A longer pulse width would continue heating the plume after the plasma has generated, which may include heating and accelerating the slower moving particles. A shorter pulse width may have a higher ionization fraction, so there will be more fast-moving particles.

For a real asteroid deflection mission, it may be desirable to fire at the same spot on the asteroid surface for an extended period of time. The force measurements in this thesis were only conducted with the laser firing for 500 ms to avoid damaging the load cell, and for some samples the force leveled off. It would be insightful to know if the force will begin to degrade after several seconds of firing at the same spot. It may be the case that the force will stay constant, although the focus would need to be corrected as the laser drills into the asteroid. If that is the case, the concept of operations will be simpler, since there will be less need to fire at a fresh ablation spot. In addition to the force response, there is also the question of if the mass removal rate is constant. Especially with the powdery meteorite simulants, it may be the case that a large amount of material is dislodged quickly (without being accelerated significantly), and then afterwards the mass removal rate settles to a smaller value. If that is the case, then the specific impulse can be improved by

firing at the same spot on the surface for an extended period of time.

The difference between the specific impulse of the ions and of the overall plasma plume shows that the ion distribution found with the TOF-MS does not give a complete picture of the overall ablation plume. An ionization stage can be added in front of the TOF-MS, which would allow for the characterization of the smaller neutrals. To study the macro-particle distribution, the ablation plume can impinge on a metal or glass collecting plate. This plate can then be analyzed using a scanning electron microscope (SEM). Based on this, the size distribution can be found for the larger particles. This can then be used to determine the fraction of the total mass composed of macro-particles.

8.2.2 Required Technology Development

The work presented in this thesis, as well as previous work in the literature, has demonstrated that ALP is a promising technology for asteroid mitigation. The largest argument against ALP compared to other low-thrust electric propulsion concepts is that it is at a comparatively lower technology readiness level. One key component missing is a space-rated, low mass, high efficiency, high power (1-10 kW) laser. Fortunately, this is already an active area of interest for several fields, such as missile defense, and *in-situ* manufacturing in space. As laser technology matures, ALP will begin to look even more promising, for asteroid mitigation and other space propulsion applications.

8.2.3 Additional Applications

This thesis has focused on using ALP for asteroid mitigation. However, the research has additional applications which can be researched further. ALP can be used to move an asteroid to a closer orbit to Earth for easier access to conduct experiments or mining. With *in-situ* resource utilization, asteroid material is mined for space applications. Water is a valuable resource, as it can be used for manned missions, or converted to propellant. ALP can use virtually any solid as a propellant, which increases the amount of useful material which can be mined. Further research is needed to determine how best to harvest and propellant for ALP. It may be beneficial to grind asteroid rock into a powder, and use a binding glue to form a pellet of a consistent shape, to better integrate into an ALP system. If such a propellant is manufactured, additional experiments are needed to measure the propulsion parameters from ALP of that propellant.

The laser ablation facility used in this thesis can be used for research outside of ALP. Research using this facility is currently underway to use laser ablation as a plasma source. The effect of impingement of this plasma on various materials can then be analyzed, to simulate the effects of space weathering on spacecraft materials such as solar panel cover glass. Since virtually any solid can be ablated, this facility can generate plasma using a larger variety of materials than typical plasma sources. For example, pyroxene rock can be ablated, so the plasma plume can simulate the micrometeorite environment. The laser can also be fired directly at the spacecraft material to simulate micrometeorite impacts, as described in section 2.4.

Appendix A: Heat Transfer in the Load Cell

In this appendix, the heat transfer model of the load cell referenced in chapter 6 is discussed in more detail. Limiting the total time spent ablating is critical to avoid damaging the load cell. The load cell is calibrated to operate below 323 K, and is safe below 353 K. A 2d-axisymmetric model of the heat transfer using COMSOL Multiphysics v4.4 is used. The sample material is pyroxene, and all other materials are modeled as aluminum. Table A.1 shows the material properties used in the model.

Table A.1: Material properties used in COMSOL model.

	Thermal conductivity (k), $W \cdot m^{-1}K^{-1}$	Density (ρ), $kg \cdot m^3$	Heat capacity at constant pressure (C_p), $J \cdot kg^{-1}K^{-1}$	Surface emissivity (ϵ_{rad}), dim
Aluminum	160	2700	900	0.05
Pyroxene	2	3300	1000	0.9

The laser is conservatively modeled to output 40 W average power (the actual power is 33 W). This power is all applied to a point on the surface of the target. Radiation to a background of 293 K is the only mechanism of energy loss modeled.

This is conservative, since much of the energy goes into the ablation plume.

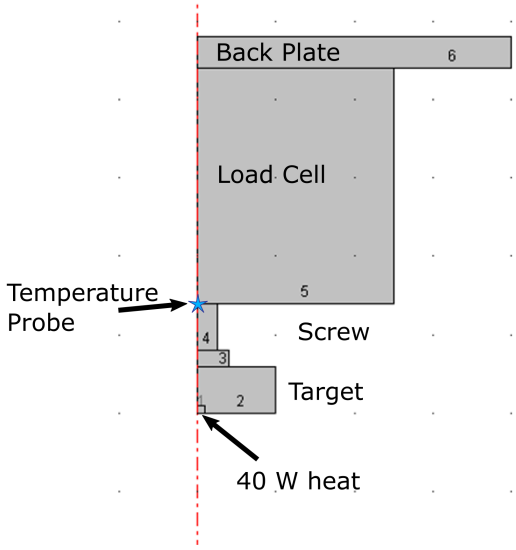

Figure A.1: COMSOL heat transfer model.

The heat transfer model is shown in Figure A.1. The internal structure of the load cell was not provided by the manufacturer, so it is represented as a solid piece of aluminum. The simulation begins with the materials at 293 K and the input power on. After a set amount of time, the power is turned off, and the system temperature decreases towards equilibrium. Figure A.2 shows the temperature at the screw vs. time. We see from Figure A.2(b) that after 50 seconds of ablation, the temperature is 327 K, slightly above the maximum calibrated operating temperature. We also see that the temperature is slow to equilibrate back to ambient temperature.

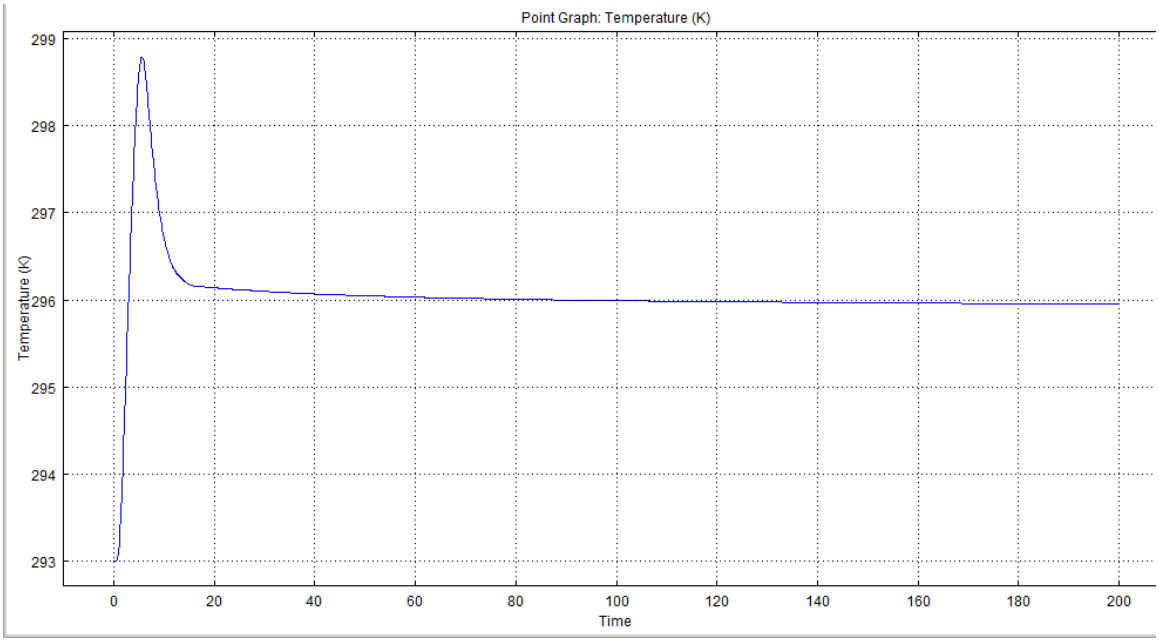

(a)

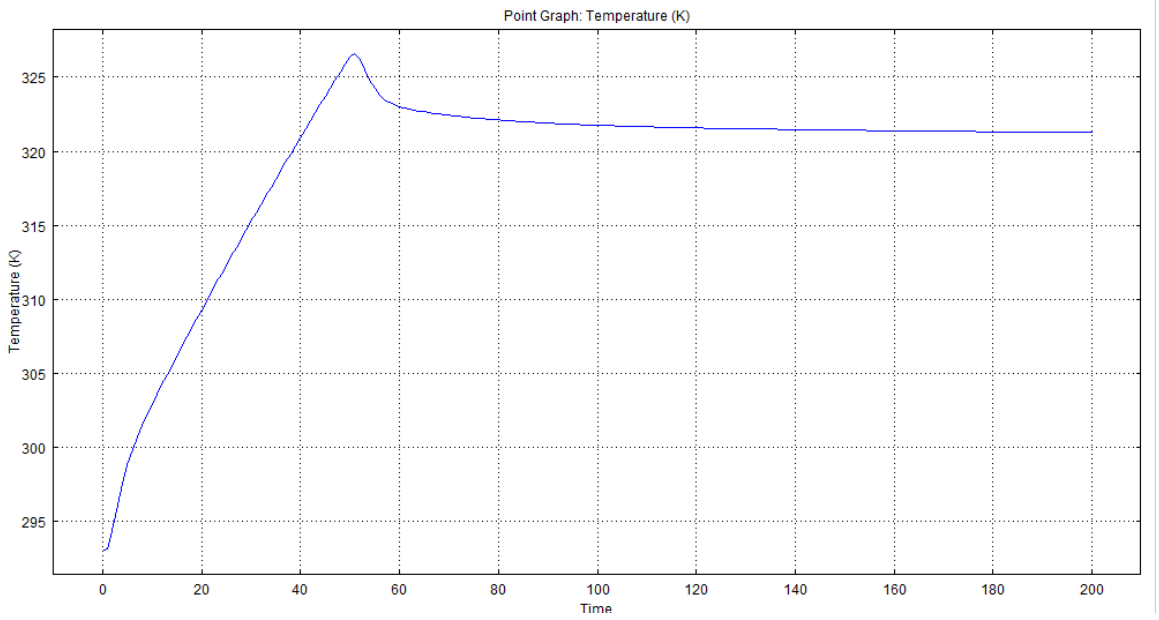

(b)

Figure A.2: Temperature at the screw vs time. The load cell is included in this model. Heating time of: (a) 4 s; and (b) 50 s.

Figure A.3 shows snapshots of the heat transfer resulting from 4 s of ablation.

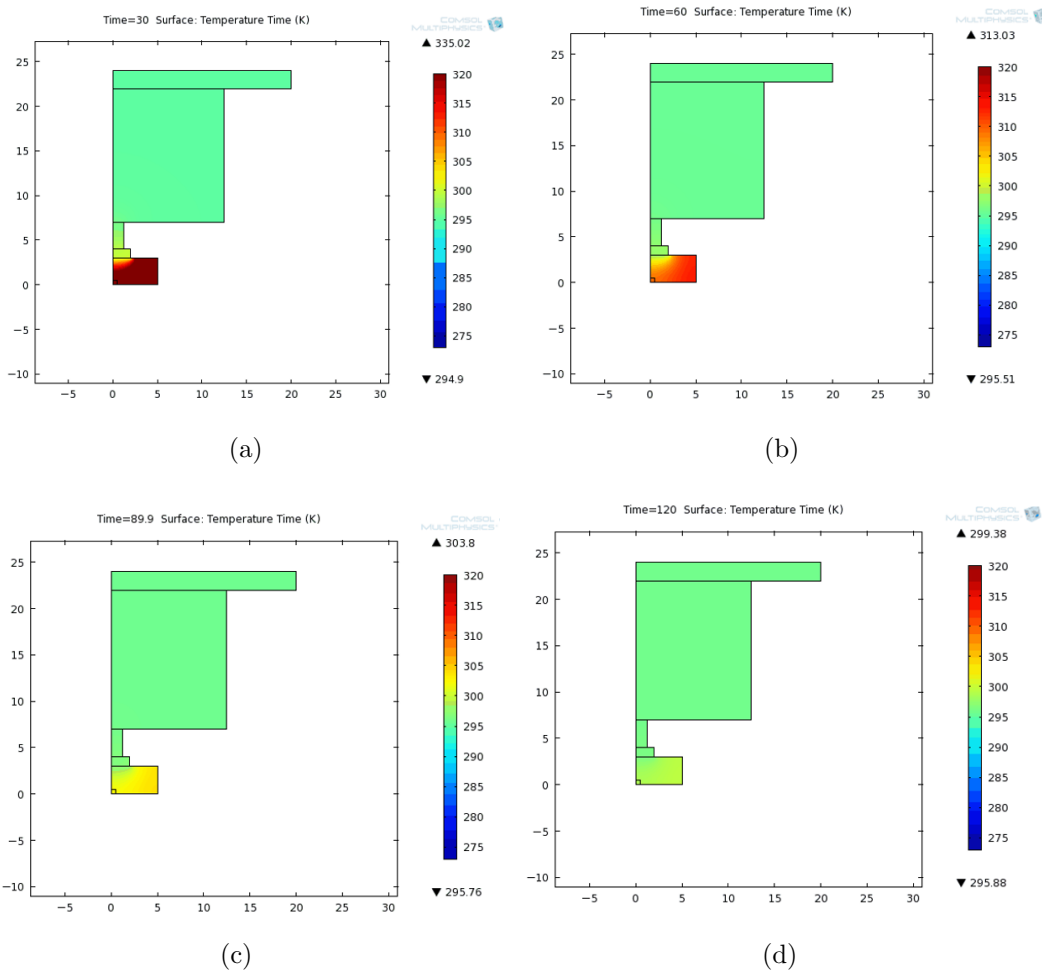

Figure A.3: Snapshot of the load cell temperature resulting from 4 s of heating. The load cell is included in this model. Snapshot taken after: (a) 30 s; (b) 60 s; (c) 90 s; and (d) 120 s.

For a more conservative simulation, only the target and screw are modeled. This decreases the total heat capacity modeled. Since the internal structure of the load cell was not provided by the manufacturer, this conservative model will be used for safety. Since the pyroxene is insulating, it still does a good job of slowing down the heat transfer, dispersing it, and giving it time to radiate. This prevents the temperature of the screw from getting close to the peak temperature of the

pyroxene. The results of this simulation are shown in Figure A.4. This result shows that 1s of ablation will reach the maximum operating temperature of the load cell.

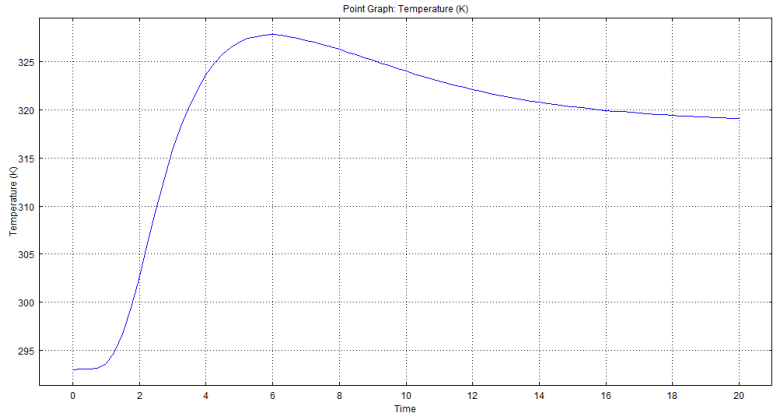

(a)

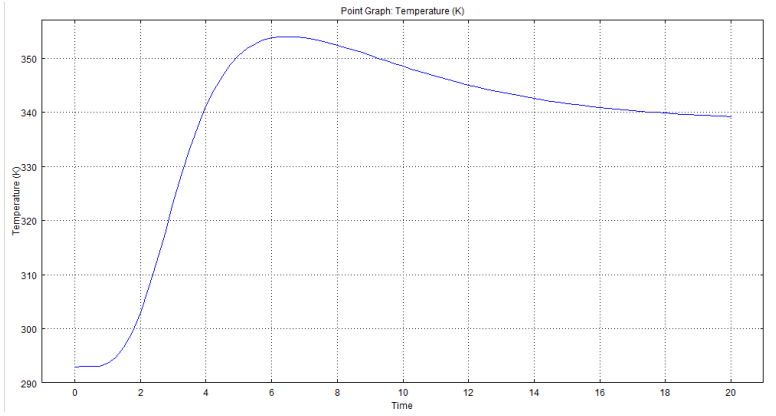

(b)

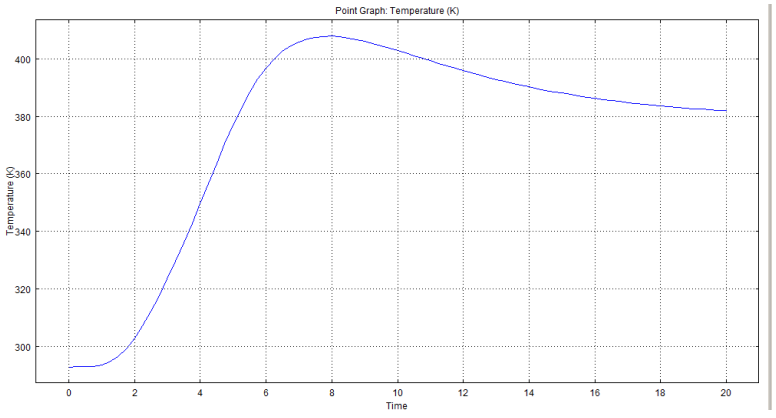

(c)

Figure A.4: Temperature at the screw vs time, only modeling screw and pyroxene. Heating time of: (a) 1 s; (b) 2 s; and (c) 5 s.

Based on these COMSOL models, the laser can safely be fired at the target for up to 1 s at a time. In between firings, the temperature must equilibrate. A.4(a) shows that it should reach equilibrium in about 2 minutes, although it may take longer than predicted by that model because the load cell is not actually a solid piece of aluminum. We may find that after several minutes, the load cell reaches an equilibrium temperature significantly higher than the ambient temperature. If this is the case, after some number of force experiments we may need to wait longer for the load cell to reach ambient temperature before starting back up with more tests. From chapter 6, it was found experimentally that 10 min was a sufficient amount of time for the load cell to return to room temperature.

Appendix B: Laser Ablation Facility Standard Operating Procedures

This appendix contains checklists and standard operating procedures for running the laser ablation facility in the University of Maryland Space Power and Propulsion Laboratory (UMD SPPL).

B.1 Vacuum Chamber Pump-down Checklist

- ☐ Monitor Pressure
  - ☐ Power up the DATAQ data acquisition system, and pressure sensor
  - ☐ Confirm that the DATAQ is plugged into the computer
  - ☐ Open the DATAQ instruments hardware manager
  - ☐ Start LabView. Run the program "Dataq pressure transducer v4.lvproj"
  - ☐ Click the run arrow in LabView. Then, click "channel 1".
- ☐ Confirm that the chamber is sealed
  - ☐ Chamber door
  - ☐ Chamber extension door
  - ☐ Up-to-air valve
  - ☐ The laser interlock LED will be green when the chamber and laser optics enclosure is sealed
- ☐ **Close ball valve between turbopump and roughing pump**
  - Handle is perpendicular to direction of airflow to be closed
- ☐ **Open ball valve between chamber and HEPA filter**
  - Handle is in-line with direction of airflow to be open
  - Note that this configuration causes air to flow through the HEPA filter, which filters out nanoparticles during the initial pump-down
- ☐ Confirm that the pump Display and Operating Unit (DCU) is plugged into the wall
- ☐ Set power switch on the back of the DCU to ON
- ☐ Confirm that roughing pump power switch is ON
- ☐ Disable the turbopump
  - ☐ Navigate to "023: Motorpump" on the DCU menu

- ☐ Press ◀▶ simultaneously to edit the menu option
- ☐ Set to OFF
- ☐ Press ◀▶ to accept

☐ Confirm "012: Enable vent" is set to ON
☐ Confirm "027: Gas mode" is set to 0
☐ Confirm "030: Vent mode" is set to 0

- Setting vent mode to 1 will prevent the chamber from automatically venting through the turbopump, even when the station is not powered. This can be used to keep the chamber at roughing pump base pressure without needing the pumps running. However, this is not recommended, so consult with the manufacturer or the manual before using this option.

☐ Confirm "308: Rotation speed" is set to 1500 Hz
☐ Press ⏻ to turn on the roughing pump. The turbopump should be disabled.
☐ Wait for the pressure to drop below 1 mbar (∼10 min)
☐ **Close the ball valve between the chamber and the HEPA filter**
☐ **Open the ball valve between the turbopump and the roughing pump**
☐ Turn on the turbopump, by setting "023: Motorpump" to ON
☐ Navigate to "309: Actual speed" to watch the turbopump spin up. The turbopump's target frequency is 1500 Hz. If the actual speed is not 1200 Hz by 8 minutes, it will shut off automatically.
☐ Wait for the base pressure ($\sim 1 \times 10^{-5}$ mbar) to be reached (∼ 1-4 h)
☐ Once the chamber has reached base pressure, the turbopump drive current should be between 0.2-0.5 A. It if is significantly above this, or if the base pressure does not drop sufficiently low, there may be a small leak.

B.2 Vacuum Pump Shutdown Checklist

☐ Press ⏻ to turn off the pumping station

- After several minutes (once the pump is below 200 Hz), the turbopump will open a valve and begin venting atmosphere into the chamber

☐ Wait for pressure to raise to 1 mbar (∼ 5 min), **and for the turbopump to stop spinning** (see menu item 309)
☐ **Close ball valve between turbopump and roughing pump**
☐ **Open ball valve between chamber and HEPA filter**
☐ Open the gas ballast if closed. (Typically, this is left open)
☐ Turn off the turbopump ("023: Motorpump")
☐ (Optional) Run air through the HEPA filter to remove nanoparticles
- ☐ Press ⏻ to turn on the roughing pump
- ☐ Open the up-to-air valve about 20%
- ☐ Run roughing pump for ∼5 min, then turn off the roughing pump

☐ Open the up-to-air valve, and wait for the chamber to reach atmospheric pressure

☐ Wait 10 minutes after the chamber is at atmosphere before opening, to give the nanoparticles time to settle

B.3 Laser Startup Checklist

- Turn on chiller
  - ☐ Plug chiller into the wall power
  - ☐ Turn on (on/off button)
  - ☐ Desired temperature is 24 °C
  - ☐ Desired flow rate is 14 L/min
- Seal vacuum chamber
  - ☐ Seal chamber door, and chamber extension door
  - ☐ Confirm that the key setting on the laser controller is OFF, and the laser key is not in the lock
- (If preparing facility for Class I operation) - Set up interlock
  - ☐ Attach interlock to the back of the laser controller
  - ☐ Power the interlock control circuit. (This is the same power supply input that powers the pressure gauge)
  - ☐ Confirm that the interlock is shorted. The interlock control circuit will light the green LED if shorted, and red if not shorted.
- (If preparing facility for Class IV operation) - Set up interlock jumper, and additional safety operations
  - ☐ Remove reflective jewelry from hands and wrists
  - ☐ Make sure that the only people in the lab are authorized to use the laser
  - ☐ Inform everyone in the office that beam alignment will be taking place and access to the lab will not be allowed at that time
  - ☐ Hang up the warning sign for beam alignment outside the main lab door and the side lab door
  - ☐ Each person in the room should have laser safety goggles. Check that each pair of goggles is rated for at least OD 6+ for 1064 nm
  - ☐ Inspect goggles for damage to the glass
  - ☐ Put on laser safety goggles (everyone in the lab). Anyone working in the optics enclosure should preferably wear the goggles that completely cover the eyes
  - ☐ Attach the interlock jumper to the back of the laser controller. This allows the laser to fire without an interlock
- Arming the Laser
  - ☐ Confirm that the chiller has reached required temperature and flow rate (may take a couple minutes)

- ☐ Confirm that the key setting on the laser controller is OFF, and the laser key is not in the lock
- ☐ Confirm that the switch in the rear of the laser controller is OFF
- ☐ Plug in the laser power cord to the laser controller
- ☐ Plug in the laser controller to the wall
- ☐ Plug laser controller into wall power. The laser controller is connected to a power strip, so you can use the power strip switch to enable power. You will hear a beep, but will not see the screen on the laser controller turn on. If needed, confirm that the rear switch on the laser controller is on.
- ☐ Wait 10 minutes for the laser and laser controller to warm up
- ☐ Turn on the laser controller (switch on the front of the controller). The controller will beep, all of the lights will turn on momentarily, and the screen will turn on.
- ☐ Confirm that the shutter is off. If the shutter LED is flashing on/off, the interlock is not connected
- ☐ Confirm the following settings on the controller are correct
  - ☐ freq: 40 kHz - Int (internal)
    - Maximum permissible range is 40-90 kHz. Do not set outside this range, or it can damage the laser.
    - If using a different frequency, change PC Window 2. See the laser manual for calibration values to use for PC Window 2 based on the selected frequency.
  - ☐ Diode Temperature (Ta) = 23.5 °C. This should not exceed ∼32 °C while the laser is running
  - ☐ In the diode settings menu, set diode current (Is) to < 1 A using the wheel. Do not use the buttons to adjust Is
  - ☐ In the pulse settings menu, Set the laser control power (PEC) to $<$ 1%.
  - ☐ Q-Switch should be ON
  - ☐ Put the ken in the laser controller, and turn the key ON. The laser is now considered armed.
  - ☐ Press the LDD button to turn it ON

- Turn on laser
  - ☐ Warm up the diode. Slowly increase Is.
    - Navigate to diode settings
    - Select Is
    - Using the wheel, slowly increase the value of Is
    - Make sure Ia is keeping up with the increase in value (within about 2A)
    - Set Is to 52 A. Note that the laser will not let you set past 53 A (which is safe to use), but the laser has been calibrated for 52 A.
  - ☐ Wait 10 minutes for the laser diode to warm up

- ☐ The laser is ready to fire. Set PEC to desired power, and use the shutter button to fire the laser.
- ☐ If the laser is unstable, fire the laser for up to 30 minutes. Consider tweaking PC-Window 2.

B.4 Laser Shutdown Checklist

- ☐ Confirm that laser shutter is set to CLOSED (off)
- ☐ Set PEC power $< 1\%$
- ☐ Turn off laser diode
  - Slowly ratchet down laser diode current (Is) on the laser controller. Use the knob, not the buttons. Make sure the actual diode current (Ia) is keeping up (within 3 A).
  - Set Is to 0.8 A
- ☐ Set LDD to OFF (no light)
- ☐ Turn laser key to OFF, and remove the key
- ☐ Turn off the power to the laser controller
- ☐ Power switch on the front of the laser controller
- ☐ Turn off power switch on the back of the laser controller
- ☐ (Class IV operation) Disconnect interlock jumper from the back of the laser controller
- ☐ If needed, put the lid on the enclosure
- ☐ Wait 10 minutes for the laser to cool down, and for power to dissipate from the diode before laser is considered cool/safe
- ☐ Turn off chiller
- ☐ Unplug chiller from wall power
- ☐ (Class IV operation) Remove warning sign from lab door

B.5 Enable External Gating of Laser (to control with Arduino)

- ☐ Laser should currently be at INT trigger
- ☐ Confirm that first pulse suppression (FPS) is enabled.
- ☐ Confirm that shutter is off
- ☐ Consider using the Picoscope to monitor the light sensitive diode in the optics enclosure, to monitor when the laser fires
- ☐ If needed, upload the desired Arduino code
  - pulse_laser.ino → Fire 1 or 5 pulses
  - pulse_laser_specifyNumPulses.ino → Fire requested number of pulses
  - pulse_laser_specifyTime.ino → Fire for the requested time
- ☐ Power on optics isolator circuit (above the laser controller box)
- ☐ Confirm that the optics isolator circuit does not have a red LED illuminated. If it is, change the batteries for the circuit.

- ☐ Connect laser gate BNC wire between isolator circuit and laser controller box
- ☐ Set up external gating
- ☐ Open shutter. Now, the laser will fire when the command to the Arduino is sent.

B.6 Disable External Gating of Laser

- ☐ Close laser shutter
- ☐ Set laser PEC power to $< 1\%$
- ☐ Set laser gating to "internal"
- ☐ Disconnect laser gate BNC wire between isolator circuit and laser controller box
- ☐ Power off isolator circuit
- ☐ Disconnect Arduino from computer

B.7 Optics Alignment

The alignment of the optics in the optics enclosure should be checked periodically. Typically check every 6 months, or if an issue is seen with the laser output.

- ☐ Remove optics enclosure lid
- ☐ Consider moving beam dump to block beam path
- ☐ Turn on laser (see laser startup checklist). Recall that this is Class IV operation, since the enclosure is open.
- ☐ Set PEC between 0.5-2% during most of the laser alignment. Take care if setting above 2%
- ☐ Use the laser "Zap-It" paper to check that the laser can be seen when firing. At $\sim$5% PEC, the paper can catch fire if the laser is fired at the same spot, but you can move the paper quickly to prevent this. Do not use the laser paper above 5% PEC.
- ☐ Monitoring laser power
  - ☐ Connect the PM100 laser power meter to the computer
  - ☐ Take care not to exceed the maximum power or the maximum intensity (power/area) of the sensor
  - ☐ Install the power meter at the location of interest in the enclosure. If placing the meter before the optics enclosure, it should be at a slight angle, so reflected laser light does not go back directly towards the laser.
  - ☐ Confirm that the laser is hitting the center of white part of the power meter
  - ☐ Run the PM100 software
  - ☐ Set wavelength in the PM100 software to 1064 nm
- ☐ Aligning optics isolator
  The optics isolator rotates laser polarization by 45°. Reflected light that goes back through the isolator is blocked from going through.
  - ☐ Confirm that the laser enters at the center of the isolator

- ☐ Confirm that the laser exits at the center of the isolator, at similar intensity visually
- ☐ If the optics isolator appears to be aligned, consider skipping the remaining optics isolator alignment procedures
- ☐ Use the power meter to record the laser power in front of the isolator. Note the measured power, and the PEC used.
- ☐ Record the laser power after the isolator. The power should be $> 95\%$ of what it was in front of the isolator when well aligned.
- ☐ Tweak the position and orientation of the the isolator to maximize the power meter reading, turning the shutter OFF and ON as needed, or monitoring power while making adjustments
- ☐ Tweak the input and output polarization to maximize the power meter reading (while keeping it approximately in the desired orientation).

☐ Check alignment of the laser at the front of the beam expander. The laser will be slightly larger due to dispersion over the course of the laser path, so you may need to increase the PEC by a percent or two.

☐ The mirrors can be used to assist with alignment. Use a hex key to loosen the knobs on top of the mirrors, making them adjustable.

B.8 Laser Software and First Pulse Suppression

☐ Connect the laser to CPU using RS232 wire. The wire must be straight-through, not a modem wire.

☐ Run "Photonics Laser Control" (PIlaserCom) software

☐ For advanced controls such as first pulse suppression (FPS) (where you can set the PEC power custom for the first 10 pulses), click on system settings wrench, and enter code "pii"

☐ The FPS is currently set to have pulse numbers 2, 3, 8-10 disabled. Pulses 1, 4-7 have been calibrated accordingly to match the average output with 100% PEC power. This has been set up so the Arduino external gating software can more easily select a specific number of pulses. If FPS is disabled, the first pulse will have more energy than the following pulses.

B.9 Aligning the Laser, XYZ Translation Stages, Laser Spot, and Time-of-Flight Mass Spectrometer

- Aligning mid (focusing) stage for optimal ablation
  - ☐ Locate some stage position where you can see ablation at any power
  - ☐ Find minimum power where ablation is still visible
  - ☐ Move middle stage, and find minimum power again
  - ☐ Repeat until you find the smallest laser power which still produces visible ablation. Typically, ablation at optimal focus is visible at PEC power below 7%. Optimal focusing stage position can be found to within about

±0.5 mm. Consider turning off light in the vacuum chamber, to see better.

- ☐ (Optional) Consider plotting minimum visible PEC power vs. focusing stage position. Fitting a parabola will give an accurate optimal stage position.

- Align the mass spectrometer
  - ☐ Install the laser alignment aluminum target to the translation stages. This target has a countersunk hole at a known distance from the edges, with an LED behind it.
  - ☐ Fire the laser at the target, taking care not to hit the LED
  - ☐ Find the stage positions such that the ablation spot is at the edge of the target. Using this, calculate the stage position that will put the LED at the ablation spot.
  - ☐ Turn off the laser completely
  - ☐ Move the stages such that the LED is at the ablation spot, and turn on the LED. The LED is powered by 5 V over a 100 Ω resistor
  - ☐ Use large "Z" shaped metal hook to remove Mu-Shield caps as needed
  - ☐ Align the spectrometer as well as possible with the aperture in the front Mu-Shield cap
  - ☐ With the front Mu-Shield cap installed, confirm that the TOF-MS gate 1 entry aperture is illuminated by the LED through the Mu-Shield cap aperture. You may need to adjust the Mu-Shield.
  - ☐ The LED light will go through the gate 1 entry aperture, and hit the gate 1 exit aperture plate. Note that the aperture is a thin slot. This can be seen on the exit aperture plate, looking through the hole in the side of the Mu-Shield for that lets wires through.
  - ☐ There is a small hole in the gate 1 exit aperture plate for alignment. This hole should be in the center of the slot of light from the LED. Adjust the TOF-MS until this is aligned properly.

B.10 Using the Time-of-Flight Mass Spectrometer (TOF-MS)

- Initial Hardware Setup
  (See other checklists for more information about these steps)
  - ☐ Vacuum chamber must be below ∼ 5e-5 mbar, otherwise the photomultiplier and other high voltage components might short
  - ☐ Power on laser
  - ☐ Monitor chamber pressure
  - ☐ Plug in the Picoscope (oscilloscope)
  - ☐ Plug in sourcemeter
  - ☐ Plug in Zaber XYZ translation stages
  - ☐ Turn on webcam
  - ☐ Turn on LEDs in the vacuum chamber

- ☐ Connect multimeter(s) to Acopian high voltage power supply(s)
  - Connect to "SIG GND" and "E MONTR"
  - 10,000:1 voltage for measured value
  - 100 mV measured → 1 kV supplied

- Confirm Initial Wiring is Correct
  - ☐ Detector and Accelerator grid → High Voltage (Acopian)
  - ☐ Scintillator bias → High voltage or ground
  - ☐ Laser light sensitive diode circuit box → +5V
  - ☐ Photomultiplier (PMT) power → Not plugged in yet. Power control knob turned off.
  - ☐ Completely disconnect EMCO high voltage for now
  - ☐ Picoscope
    - A: Laser light sensitive diode circuit output (984 Ω resistor, 5 V reverse bias)
    - B: PMT output (Measured over 2.505 kΩ resistor)
    - C: Aperture current (front aperture plate grounded over 9.77 kΩ resistor)
  - ☐ Other misc. wires → Ground

- Turn on Laser
  - ☐ (For some of these steps, refer to previous checklists for more information)
  - ☐ Turn on laser
  - ☐ Align laser focusing
  - ☐ Turn on external gating with the Arduino
  - ☐ Turn on bench power supply, and supply the laser light sensitive diode box +5 V
  - ☐ Set PEC power to 100%
  - ☐ Fire laser test pulses. On the Picoscope, confirm that the laser is firing, and that current is reaching the front aperture plate.

- Turn on photomultiplier (PMT)
  - ☐ **(High voltage ON starting now, so take extra care)**
  - ☐ Confirm that the knob on the PMT power circuit is OFF
  - ☐ Plug in +18V and +5V to the PMT power circuit at the required banana plug inputs
  - ☐ Slowly turn on the knob on the PMT power circuit. This will supply the PMT with $\sim$ 1 kV

- Turn on high voltage, and test TOF-MS
  - ☐ Use a dedicated power strip as a switch for the Acopian high voltage power supplies
  - ☐ Monitor voltage(s) of Acopian supply(s) with a multimeter

- ☐ Slowly use the Acopian supply to set detector and accelerator grid to desired voltage (typically ±5 kV)
- ☐ Use sourcemeter to set the gate to the desired voltage for an initial test (typically ±200 V, at the same polarity as the detector)
- ☐ Fire a laser pulse, and confirm on the Picoscope that a TOF signal is measured

- Set up C# Automation
  - ☐ Open "AblationSystem.sln"
  - ☐ Consider deleting old data in the debug folder
  - ☐ Update desired focusing (mid) stage position(s) based on focusing
  - ☐ Update StagePosition (stageInitial for the current stage position, and stageFirst for the first position to use during data collection)
  - ☐ Update header notes
  - ☐ Close Zaber console if needed
  - ☐ Run Main.cs, and confirm items in the command prompt
  - ☐ Make sure to note and update the stagePositions after each run

- TOF-MS Shutdown
  - ☐ Slowly turn down Acopian power supply(s), then use the switch on the power strip to turn off, then unplug. Confirm with the multimeter that the voltage is zero.
  - ☐ Slowly turn down the PMT knob, then turn off bench power supply, and unplug power to the circuit
  - ☐ If needed, turn off EMCO power supplies
  - ☐ Turn of sourcemeter
  - ☐ **Confirm all high voltage is OFF**
  - ☐ Disable external gating
  - ☐ Turn off laser
  - ☐ Unplug Zaber stages
  - ☐ Use TortoiseHG version control software to commit the AblationSystem folder. Then, copy the folder to to today's experiment notes folder. Note that the TOF-MS data is in the "debug" sub-folder. (Optional) Rename the folder.
  - ☐ Confirm that the bench power supply is off, and unplug power to the laser diode circuit and PMT power circuit
  - ☐ Turn off pumps
  - ☐ Unplug Picoscope
  - ☐ Return multimeters
  - ☐ Unplug DAC, DATAQ, power to interlock circuit, and chamber LEDs
  - ☐ Put away extension cords (if needed)
  - ☐ Confirm that everything is off

B.11 Changing Laser Chiller Water and Filter

- ☐ Drain water from drain valve at the bottom of the chiller
- ☐ Remove pump bleed red plunger to complete draining the water. You need to push the black piece of plastic in while pulling the red plunger out. This will allow air in.
- ☐ Replace filter in the back if needed (this should be done every 6 months)
- ☐ If needed, order replacement filters. Check laser manual for requirements for particle size filtered, or see model number of new filter.
- ☐ Add distilled (not de-ionized) water back in
- ☐ Add 2 drops of anti-fungal liquid
- ☐ It's recommended to run with new water for 15 min. Then, drain and replace water (including anti-fungal liquid), and let run for 15 min again.
- ☐ Tips to try when debugging
    - Fill water in filter container
    - Drain red and blue water tubes
    - Disable automatic shutoff (either for flow or water level) to give it time to start up
    - Admin code for chiller password: 0020
    - Water level → Level Monitor → Disable. Make sure to re-enable when done de-bugging.
    - Drain filter, and unplug and drained both hoses
    - Pulling on the tubes in the back works to get them off (after unscrewing tie-downs). Twisting and wedging was not as helpful
- ☐ Add to log that the chiller water and filter was changed

B.12 Hornet Pressure Gauge

- The Hornet pressure gauge is a backup, and can be used to confirm the pressure reading.
- The Hornet high pressure gauge is always on when powered. The low pressure (ion) gauge must be manually turned on and off.
- Verify that the high pressure gauge reads < 1e-3 Torr
- click menu, then select "setup unit" > "FP operate" > "unit on/off"
- Make sure to turn back off before turning off pressure gauge or pumps

B.13 EMCO High Voltage Power Supply

The EMCO high voltage power supplies are controlled with a voltage regulator circuit. The circuit can be wired such that either positive or negative polarity voltage is output. Multiple power supplies are available, up to 10 kV.

- ☐ (For positive polarity) Connect thick red wire (+HV) from EMCO power supply to the right screw terminal on the voltage regulator circuit
- ☐ (For negative polarity) Connect the thick white wire (-HV) from EMCO power supply to the right screw terminal
- ☐ Confirm that the right screw terminal is also connected to the large resistor on the 2038:1 voltage divider
- ☐ Connect the other thick wire (±HV) from the EMCO power supply to the left screw terminal
- ☐ Confirm that the left screw terminal is connected to ground, and to the small resistor on the voltage divider
- ☐ Connect the wire coming from the center of the voltage divider to $V_{feedback,in}$ on the perfboard. In addition, probe this wire directly using a multimeter (noting that 0.49 V measured corresponds to 1 kV output).
- ☐ Turn off the knob for the voltage regulator circuit
- ☐ Plug in the bench power supply to the labeled input on the voltage regulator circuit (+12 V), and turn on
- ☐ Slowly increase voltage, making sure to never exceed the following values (to avoid shorting):
    - Only apply high voltage when the vacuum chamber is at $< \sim 5 \times 10^{-5}$ mbar. Applying high voltage at atmosphere may be safe, but take extra care. Do not apply high voltage at low vacuum, since this is the worst case for shorting.
    - Maximum scintillator bias: ±8 kV
    - Maximum scintillator bias relative to the detector: ±5 kV
    - Consider the order that you set high voltages to different items, to avoid exceeding relative bias requirement

B.14 New Student Training

Requirements for new students being trained to operate the laser ablation facility

- Complete all ESS required general lab safety training
- Complete ESS laser safety training
- Undergraduates are not authorized to operate high voltages without a trained graduate student present, without additional approval

- For all procedures (e.g. checklists in this appendix), undergraduates must first observe the procedures done by a trained graduate student, and be trained on how to perform them. Then, the undergraduate must perform these procedures under supervision. After this, the graduate student can authorize an undergraduate to perform this procedure independently.
- Be aware of the location of the manuals for the laser, laser chiller, and vacuum pumps. These are located in a box under the lab computer, and some are also saved on the lab computer.
- Trained graduate students
  - Joshua Sloane
  - Eric Smith
- Trained undergraduate students
  - Bernadette Canon (graduated)
  - Nuŕia Such Cueves (graduated)
  - Skylar Trythall (graduated)
  - Evan Kramer

Appendix C: Direct Force Measurement Data

In chapter 6, the force vs. time due to laser ablation of asteroid materials is measured. This appendix includes the load cell force vs. time data for each experiment case. It also includes an example of the raw load cell data, taken over several minutes.

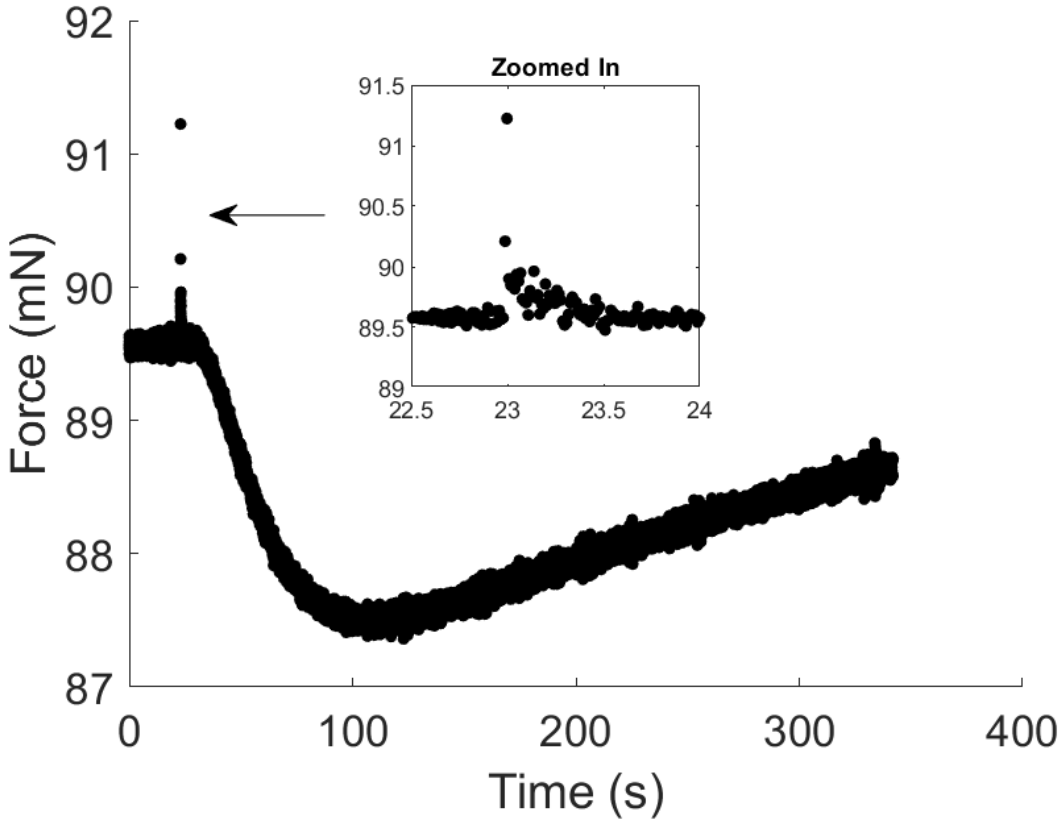

Figure C.1: Raw load cell force vs. time for Aluminum, at optimal focus. The ablation event occurs 23 s after data capture begins, and is seen as a spike in the force. The laser fires for 500 ms, and the force decreases during this time, and then flattens once the laser stops firing. Several seconds after the firing occurs, the raw force appears to slowly decrease, and then equilibrate. This is an artifact due to heating of the load cell, and is clearly distinguished from the actual ablation event.

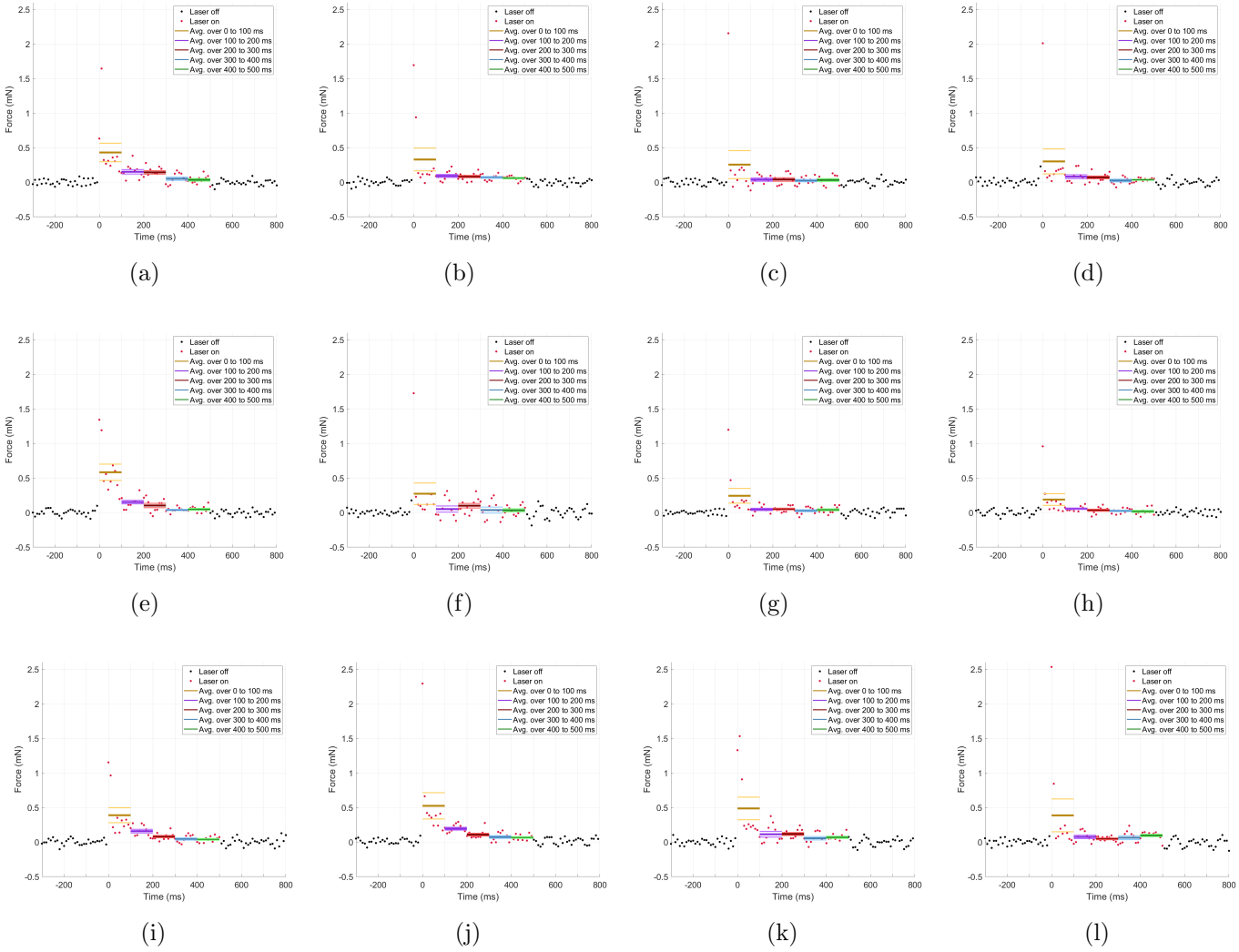

Figure C.2: Load cell force vs. time data for Aluminum. Y-axis position (relative to optimal focus) are: (a) 0.0 mm; (b) -1.0 mm; (c) -2.0 mm; (d) -3.0 mm; (e) 0.0 mm; (f) 1.0 mm; (g) 2.0 mm; (h) 3.0 mm; (i) 0.8 mm; (j) 0.3 mm; (k) -0.3 mm; (l) -0.8 mm;

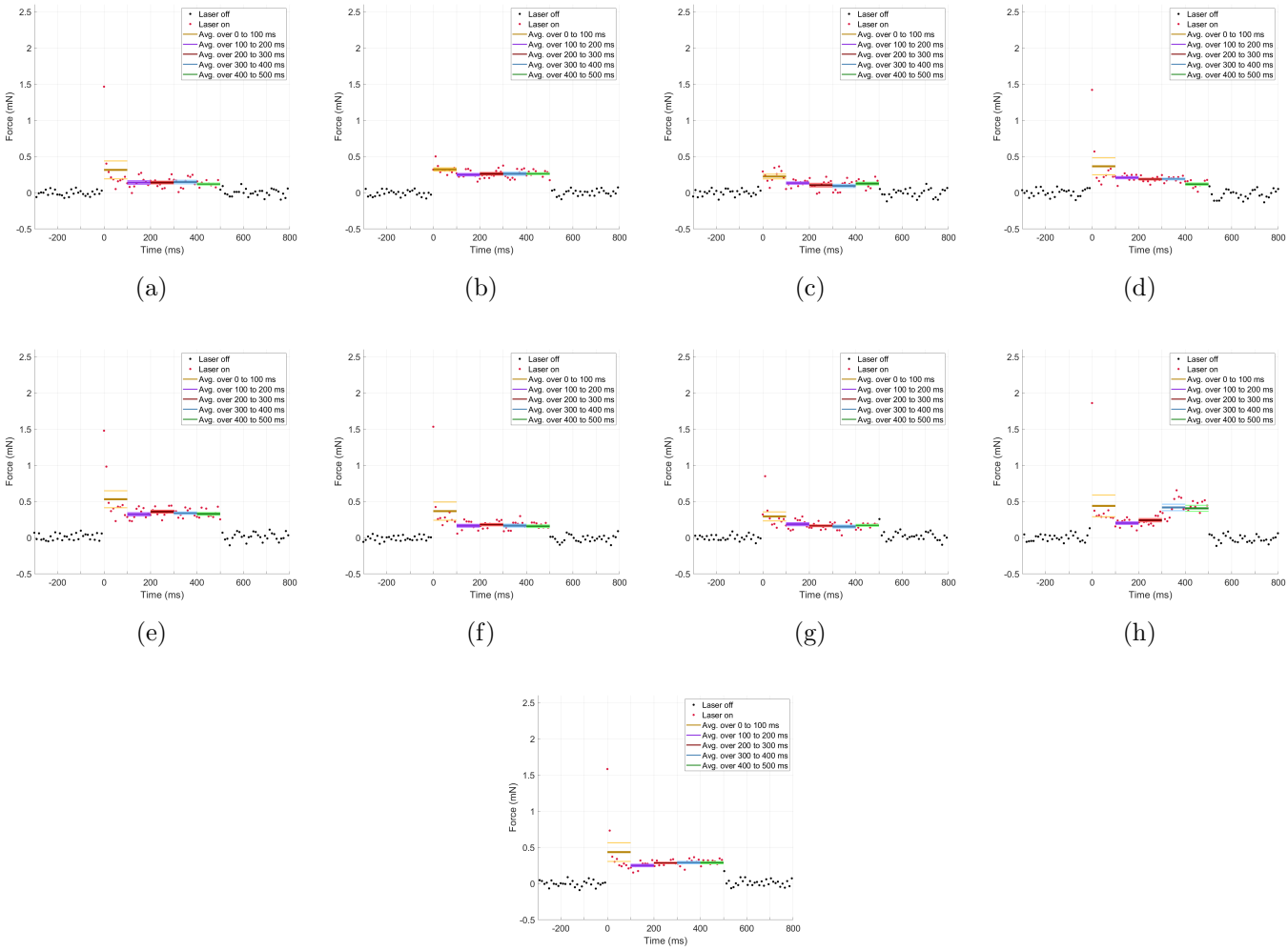

Figure C.3: Load cell force vs. time data for Pyroxene. Y-axis position (relative to optimal focus) are: (a) 0.0 mm; (b) -1.0 mm; (c) -2.0 mm; (d) 0.0 mm; (e) 1.0 mm; (f) 2.0 mm; (g) 3.0 mm; (h) 1.5 mm; (i) 0.5 mm;

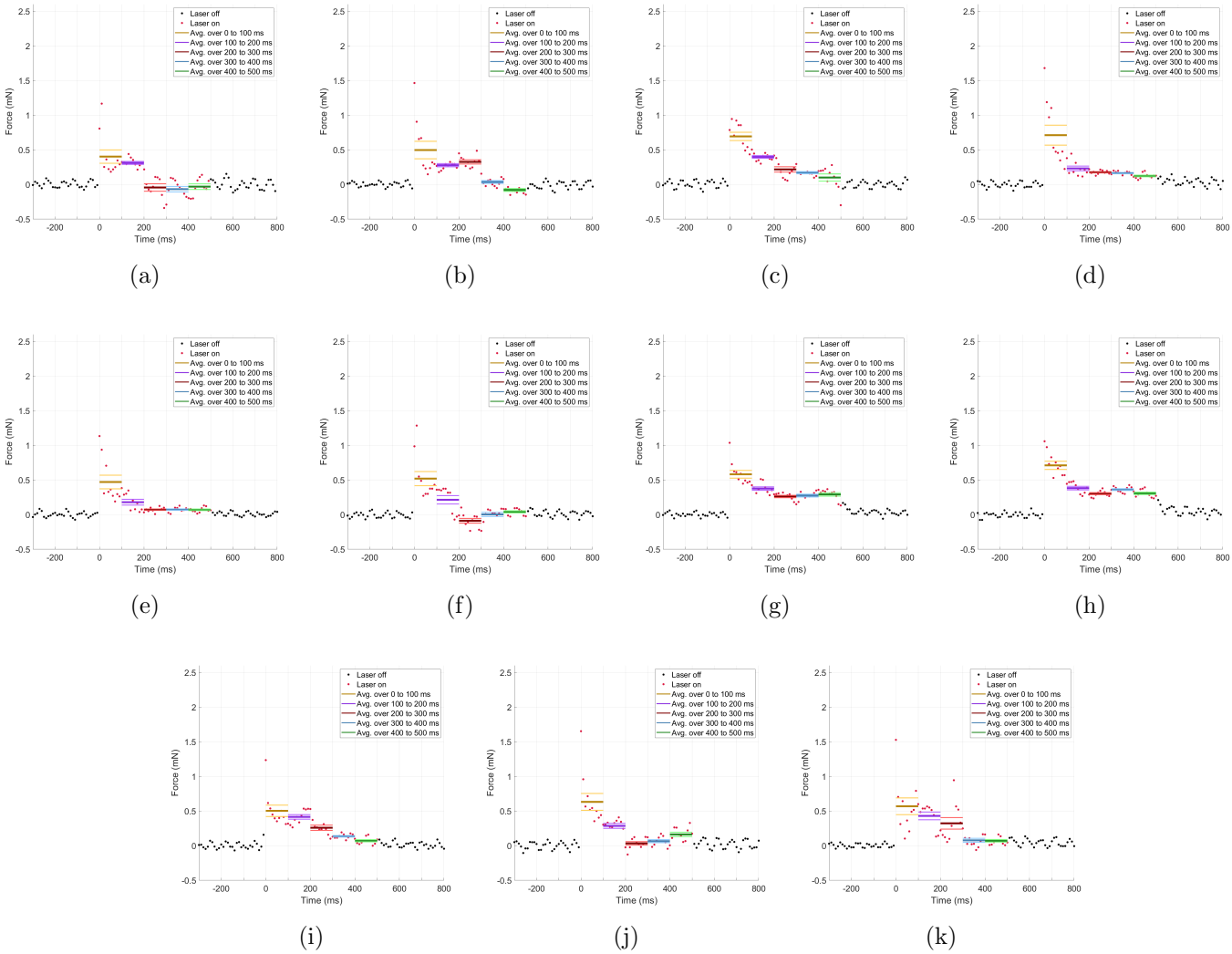

Figure C.4: Load cell force vs. time data for CM Simulant. Y-axis position (relative to optimal focus) are: (a) 0.0 mm; (b) -1.0 mm; (c) -2.0 mm; (d) -3.0 mm; (e) 0.0 mm; (f) 1.0 mm; (g) 2.0 mm; (h) 3.0 mm; (i) 1.5 mm; (j) 0.5 mm; (k) -0.5 mm;

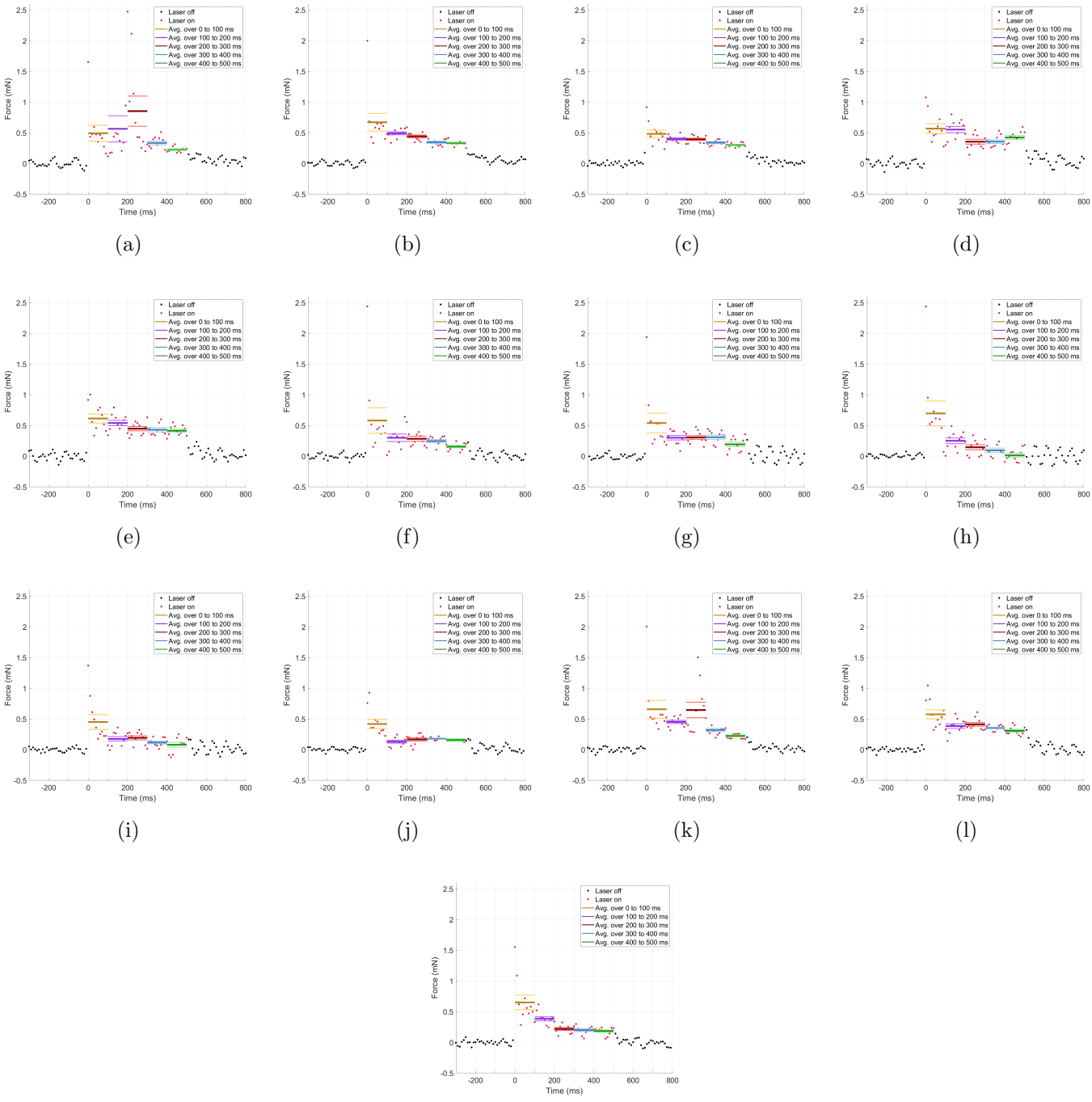

Figure C.5: Load cell force vs. time data for CR Simulant. Y-axis position (relative to optimal focus) are: (a) 0.0 mm; (b) -1.0 mm; (c) -2.0 mm; (d) -3.0 mm; (e) -4.0 mm; (f) 0.0 mm; (g) 1.0 mm; (h) 2.0 mm; (i) 3.0 mm; (j) 1.5 mm; (k) 0.5 mm; (l) -0.5 mm; (m) -1.5 mm;

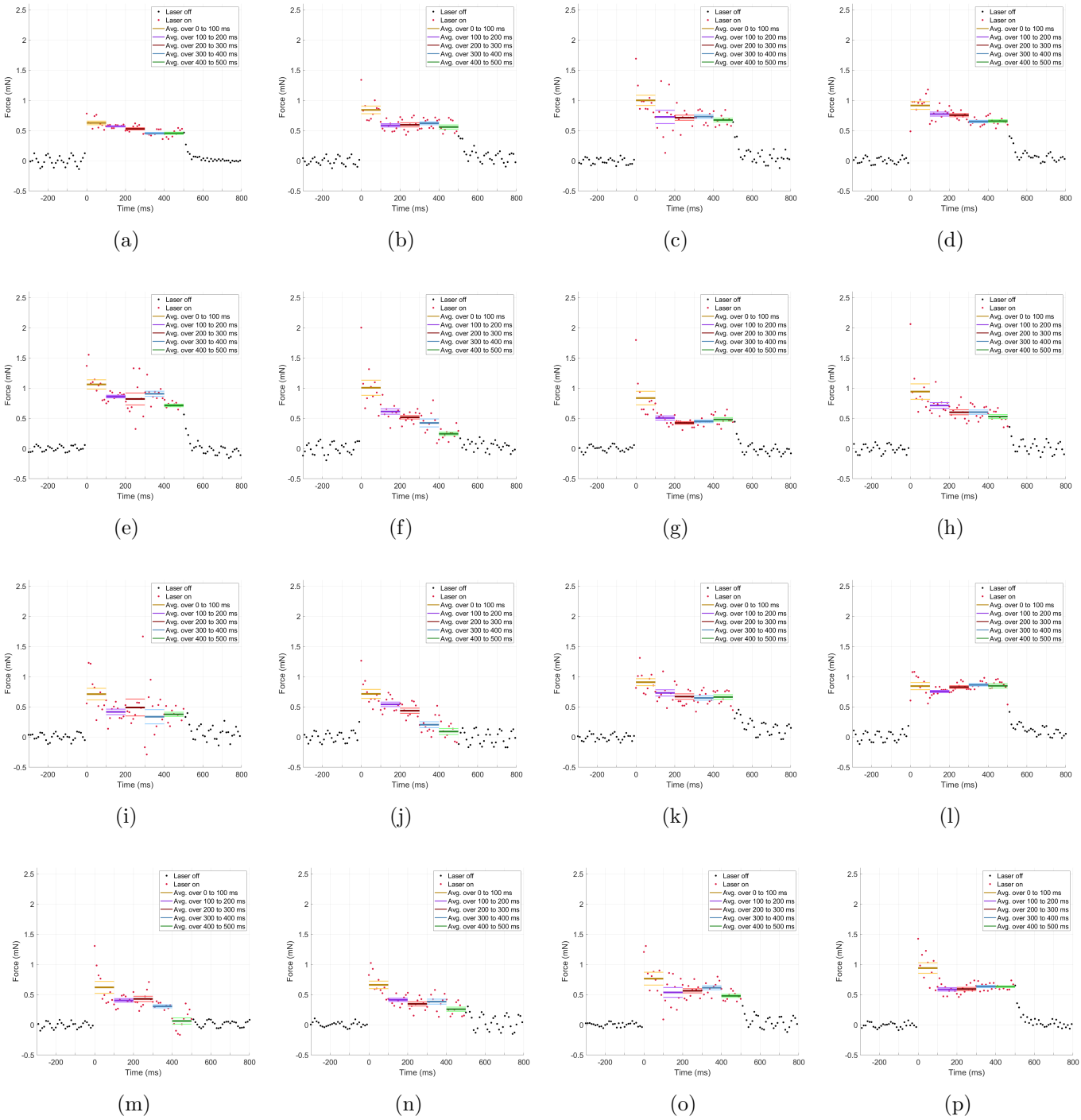

Figure C.6: Load cell force vs. time data for CI Simulant. Y-axis position (relative to optimal focus) are: (a) 0.0 mm; (b) -1.0 mm; (c) -2.0 mm; (d) -3.0 mm; (e) -4.0 mm; (f) 0.0 mm; (g) 1.0 mm; (h) 2.0 mm; (i) 3.0 mm; (j) 4.0 mm; (k) -6.0 mm; (l) -8.0 mm; (m) 1.5 mm; (n) 0.5 mm; (o) -0.5 mm; (p) -1.5 mm;

Appendix D: Additional Figures and Analysis

D.1 Hardware

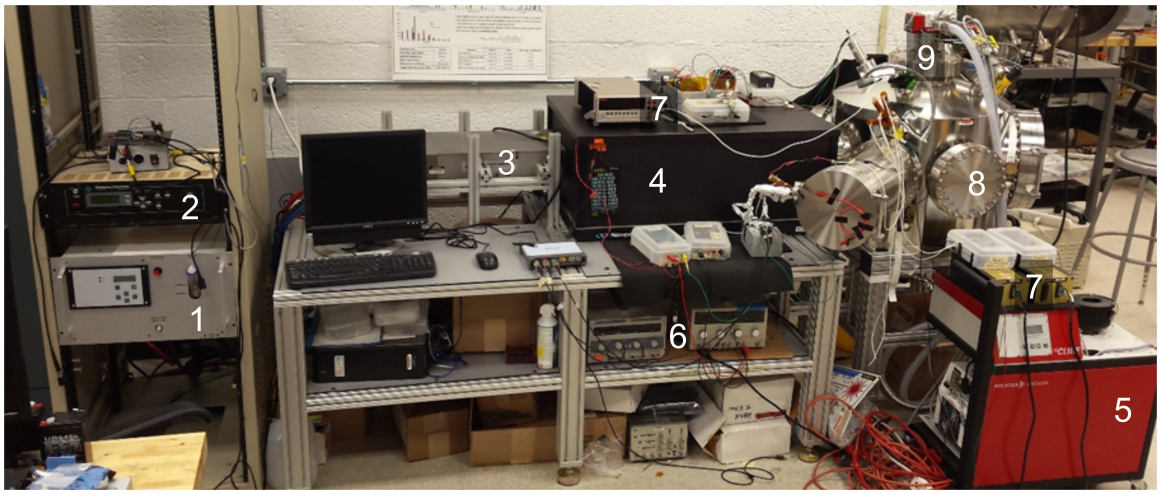

Figure D.1: Laser Ablation Facility. (1) Laser chiller; (2) laser controller; (3) laser; (4) optics enclosure; (5) rouging pump; (6) bench power supplies; (7) high-voltage power supplies; (8) vacuum chamber; (9) turbo-pump.

Figure D.2: Time of flight mass spectrometer hardware.

D.2 Effect of Ablation Sample Speed on Plume Direction

For impingement tests, we wish to use the laser ablation facility to generate a strong, consistent ablation plume. Ablation can be conducted on almost any solid, so there is a large range in the ablation plume which can be generated. This plume then impinges on a material, such as solar panel components, and the damage due to impingement is later analyzed. To maintain a fresh ablation spot while the laser is firing at 40 kHz, the sample to be ablated is moved in a raster motion in the horizontal x-axis. For a single laser pulse at a fresh spot, the plume is directed normal to the surface.

Preliminary analysis was conducted on ablation of an aluminum sample. We found that the speed of the sample effects both the direction and the strength of the ablation, while the laser was firing at 40 kHz. The ablation plume was weak and inconsistent (flickering on and off) when the sample was moving less than 0.25 mm/s. The plume strength increased as the speed increases up to 4 mm/s, after which moving the sample faster did not appear visually to significantly increase the plume strength. A faster speed consumes the sample more quickly, which must be traded with the improved plume strength when deciding what speed to use during impingement tests. Knowledge of the plume direction is also important to determine proper placement of samples to be impinged to ensure that they are in the center of the plume.

(a)

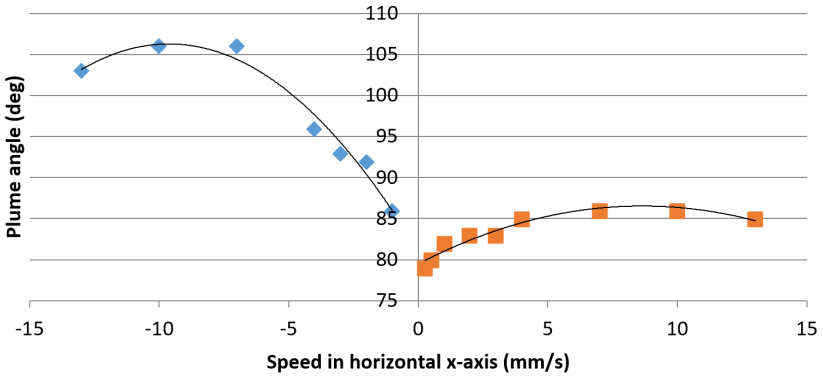

(b)

Figure D.3: Effect of ablation sample speed on plume direction.
(a) A webcam is used to measure the ablation, mounted at an angle. The angle of the ablation plume is measured referenced to the normal of the surface. A correction is made for parallax associated with the webcam position. This figure shows an example with the sample moving at 13 mm/s.
(b) A plot of the plume direction vs. speed is shown, with 90° being normal to the target surface. The laser hits the sample at a 45° angle in the X-Y plane, which is why the direction of motion effects the angle of the plume.

D.3 Ablation Strength vs. Pulse Number

For many experiments in this thesis, the laser is fired at the same ablation spot multiple times. In this section, the effect of pulse number on the ablation strength is analyzed.

The laser is fired at 6061 aluminum. This sample was previously cleaned, but did not have a mirror finish as was used in chapter 6. The laser is fired at 40 kHz. The ablation plume first must pass through an aperture in the mu-shield before reaching the TOF-MS. Most of the ablation plume which goes through the mu-shield aperture hits the entry aperture plate on the TOF-MS, and does not pass through the gate 1 entry aperture. Current on the gate 1 entry aperture plate flows over a 9830 Ω resistor to ground. This current is integrated to get the total charge which hits the plate, which corresponds to the strength of the ablation event. The laser strength varies between pulses, and was measured with a fast light-sensitive diode which detects stray laser light in the optics enclosure. The diode current was measured over a 984 Ω resistor, which was integrated to give the laser energy in arbitrary units. The current at the gate 1 aperture plate is divided by this laser energy measurement to correct for variations in the laser strength.

Figure D.4 shows the corrected charge on the gate 1 entry aperture plate. The ablation strength increases over the first couple pulses. This is likely either due to heating of the surface, or forming a nozzle like shape which better directs the plume. The signal strength begins to degrade by pulse 20. By pulse 50, the pulse has leveled off. Six sweeps of pulse number are shown in the figure.

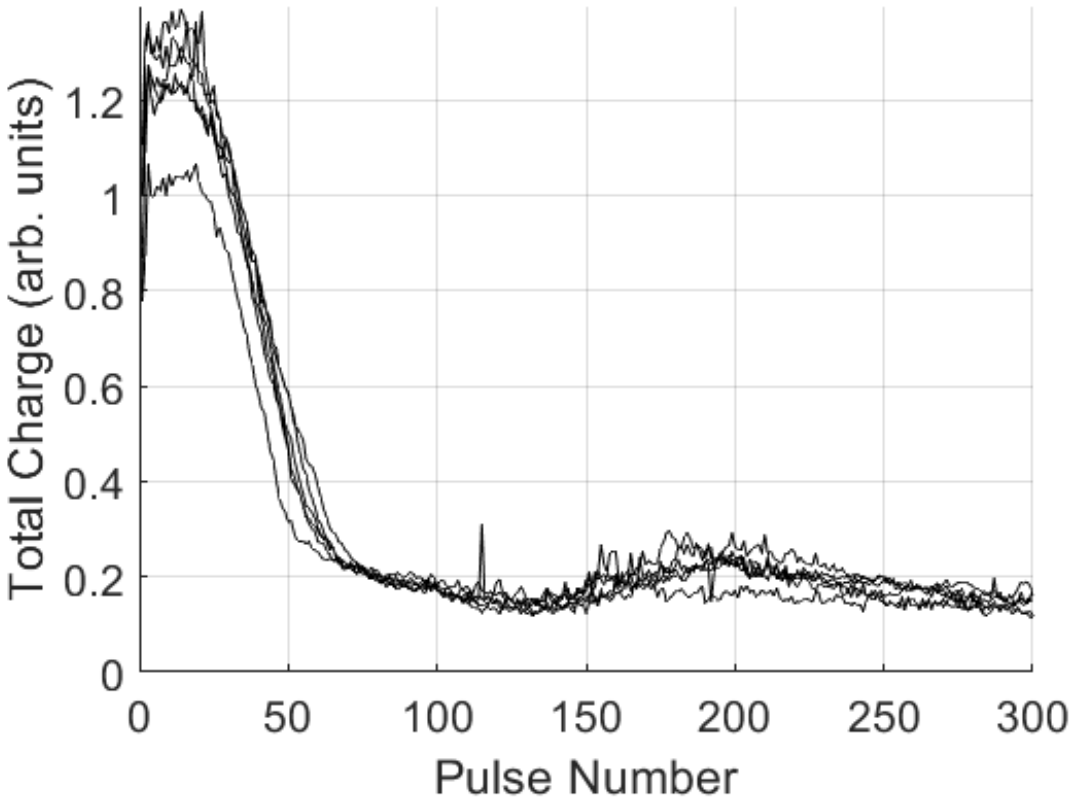

Figure D.4: Ablation strength vs. pulse number for aluminum.

Similar analysis was conducted for ablation of pyroxene, using some of the data discussed in chapter 5. For these experiments, there was approximately 0.25 s between each laser pulse. Figure D.5 shows the charge on the gate 1 entry aperture plate, normalized by the laser energy. The ablation strength is not affected by pulse number for the first 200 pulses.

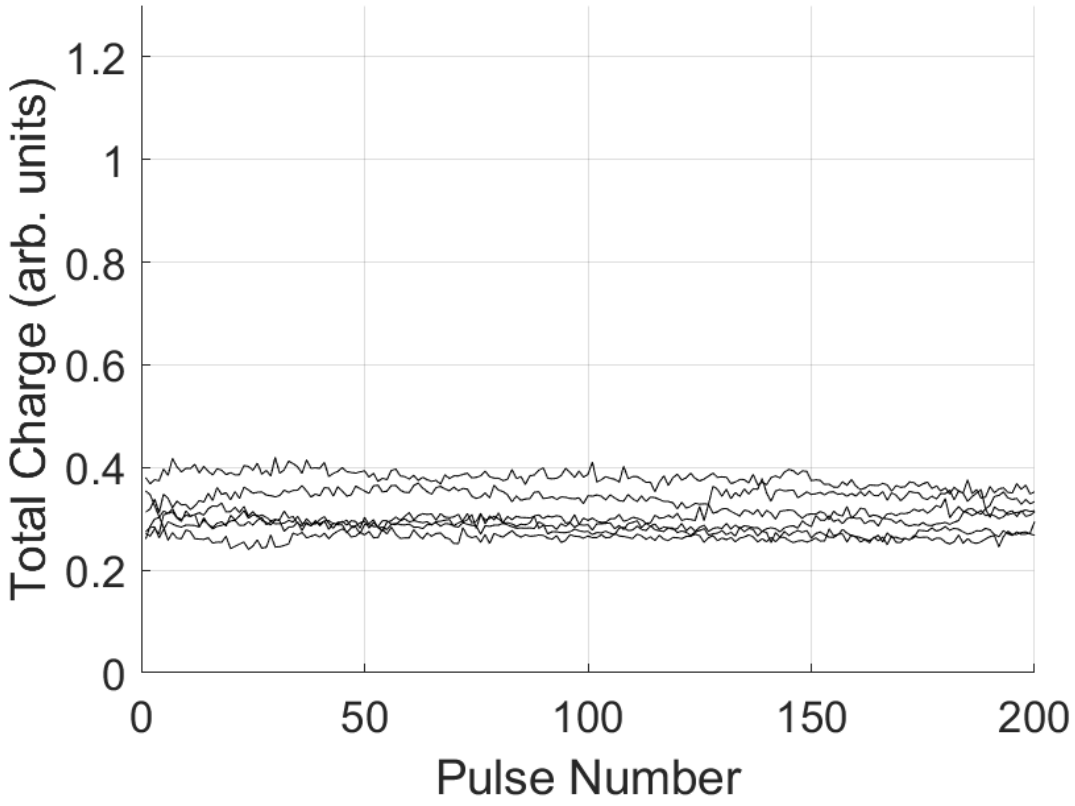

Figure D.5: Ablation strength vs. pulse number for pyroxene.

D.4 Load Cell Setup

Figure D.6: Shaping of CM simulant (UCF/DSI-CM-2) to the desired dimensions. Note how the simulant is brittle, and can be shaped by scoring with the side of a flathead screwdriver.

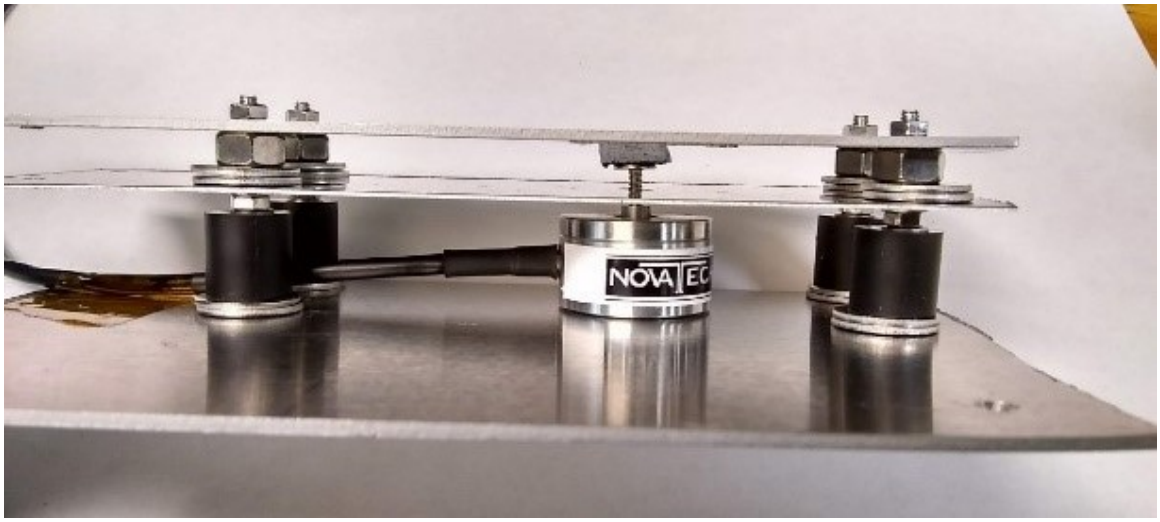

Figure D.7: Load cell, mounting bracket, and pyroxene sample.

Bibliography

[1] NEOShield. Threat from NEO. http://www.neoshield.eu/protecting-earth-asteroids-comets-neos/asteroid-neo-impact-threat-earth/%0A, 2018.

[2] Joseph Scott Stuart and Richard P Binzel. Bias-corrected population, size distribution, and impact hazard for the near-Earth objects. *Icarus*, 170(2):295–311, 2004.

[3] Hector Javier Durand-Manterola and Guadalupe Cordero-Tercero. Assessments of the energy, mass and size of the Chicxulub Impactor. *arXiv preprint arXiv:1403.6391*, 2014.

[4] Peter Schulte, Laia Alegret, Ignacio Arenillas, José A Arz, Penny J Barton, Paul R Bown, Timothy J Bralower, Gail L Christeson, Philippe Claeys, Charles S Cockell, and Others. The Chicxulub asteroid impact and mass extinction at the Cretaceous-Paleogene boundary. *Science*, 327(5970):1214–1218, 2010.

[5] Richard P Binzel. The Torino impact hazard scale. *Planetary and Space Science*, 48(4):297–303, 2000.

[6] Steven R Chesley, Paul W Chodas, Andrea Milani, Giovanni B Valsecchi, and Donald K Yeomans. Quantifying the Risk Posed by Potential Earth Impacts. *Icarus*, 159(2):423–432, 2002.

[7] NASA. Near-Earth Object Survey and Deflection Analysis of Alternatives - Report to Congress. Technical report, NASA, 2007.

[8] NASA JPL Center for Near Earth Object Studies. NEO Search Program. https://cneos.jpl.nasa.gov/about/search_program.html, 2019.

[9] Alan W. Harris and Germano D'Abramo. The population of near-Earth asteroids. *Icarus*, 257:302–312, 2015.

[10] Jet Propulsion Laboratory. NEOCam: Finding asteroids before they find us. https://neocam.ipac.caltech.edu/page/Instrument, 2019.

[11] Don Yeomans. Near-Earth Asteroid 2004 MN4 reaches highest score To date on hazard scale. https://cneos.jpl.nasa.gov/news/news146.html, 2004.

[12] NASA Jet Propulsion Laboratory. NASA Rules Out Earth Impact in 2036 for Asteroid Apophis. https://www.jpl.nasa.gov/news/news.php?release=2013-017, 2013.

[13] Thomas J Ahrens and Alan W Harris. Deflection and fragmentation of near-Earth asteroids. *Nature*, 360(6403):429, 1992.

[14] Sang-Young Park and I Michael Ross. Two-body optimization for deflecting Earth-crossing asteroids. *Journal of Guidance, Control, and Dynamics*, 22(3):415–420, 1999.

[15] Sang-Young Park. Deflection of earth-crossing asteroids/comets using rendezvous spacecraft and laser ablation. In *2004 Planetary Defense Conference: Protecting Earth from Asteroids*, pages 1–12, Orange County, California, 2004.

[16] D Izzo, J Olympio, and C Yam. Asteroid deflection theory: fundamentals of orbital mechanics and optimal control. In *1st IAA Planetary Defense Conference*, 2009.

[17] Paul W Chodas and Donald K Yeomans. Predicting Close Approaches and Estimating Impact Probabilities for Near-Earth Objects. *Advances in Astronautical Sciences*, 1999.

[18] National Research Council. *Defending planet earth: Near-Earth-Object surveys and hazard mitigation strategies*. National Academies Press, 2010.

[19] NASA. 2006 Near-Earth Object Survey and Deflection Study. Technical report, NASA, 2006.

[20] Planetary Defense Conference. Planetary Defense Conference exercise - 2015. https://cneos.jpl.nasa.gov/pd/cs/pdc15/, 2015.

[21] Jesse D. Koenig and Christopher F. Chyba. Impact Deflection of Potentially Hazardous Asteroids Using Current Launch Vehicles. *Science & Global Security*, 15(1):57–83, 2007.

[22] NASA. Deep Impact Comet Encounter (Press Kit). Technical report, NASA, 2005.

[23] B Kantsiper, A Cheng, and C Reed. The Double Asteroid Redirection Test mission. In *2016 IEEE Aerospace Conference*, pages 1–7, mar 2016.

[24] Donald Gennery. Deflecting asteroids by means of standoff nuclear explosions. In *2004 Planetary Defense Conference: Protecting Earth from Asteroids*, AIAA SPACE Forum. American Institute of Aeronautics and Astronautics, feb 2004.

[25] Matthew L Marcus, Joshua B Sloane, Oliver B Ortiz, Brent W Barbee, Nasa Goddard, and Space Flight. Planetary defense mission using guided collision of Near-Earth Objects. *Journal of Spacecraft and Rockets*, 54(5), 2017.

[26] Defense Threat Reduction Agency. Project TRINITY. http://www.dtra.mil/Portals/61/Documents/NTPR/1-Fact_Sheets/6_TRINITY.pdf, 2019.

[27] Phipps. Lasers can play an important role in the planetary defense. In *Proceedings of the Planetary Defense Workshop*, Livermore, California, 1995.

[28] D.C. Hyland, H.A. Altwaijry, H. Kim, N. Satak, and S. Ge. NEA mitigation via the Yarkovsky effect. In *Advances in the Astronautical Sciences*, volume 150, 2013.

[29] Daniel D Mazanek, David M Reeves, Joshua B Hopkins, Darren W Wade, Marco Tantardini, and Haijun Shen. Enhanced gravity tractor technique for planetary defense. In *4th IAA Planetary Defense Conference - PDC 2015*, Frascati, Roma; Italy, 2015.

[30] John Brophy, Nathan Strange, Dan Goebela, Shawn Johnson, Dan Mazanek, and David Reeves. Characteristics of a high-power ion beam deflection system necessary to deflect the hypothetical asteroid 2017 PDC. *The Journal of Space Safety Engineering*, 5(1):34–45, 2018.

[31] Alison Gibbings, Massimiliano Vasile, John-Mark Hopkins, David Burns, and Ian Watson. Experimental characterization of the thrust induced by laser ablation onto an asteroid. In *Planetary Defense Conference 2013*, 2013.

[32] Arthur Kantrowitz. Propulsion to orbit by ground-based lasers. *Aeronautics and Astronautics*, 10:74–76, 1972.

[33] Claude R. Phipps, Mitat Birkan, Willy Bohn, Hans-Albert Eckel, Hideyuki Horisawa, Thomas Lippert, Max Michaelis, Yuri Rezunkov, Akihiro Sasoh, Wolfgang Schall, Stefan Scharring, John E. Sinko, Mitat Birkan, Willy Bohn, Hans-Albert Eckel, Hideyuki Horisawa, Thomas Lippert, Max Michaelis, Yuri Rezunkov, Akihiro Sasoh, Wolfgang Schall, Stefan Scharring, and John E. Sinko. Review: Laser-ablation propulsion. *Journal of Propulsion and Power*, 26(4):609–637, 2010.

[34] Gennady G. Gladush and Igor Smurov. *Physics of Laser Materials Processing*, volume 146. Springer Science; Business Media, 2015.

[35] S. Amoruso, R. Bruzzese, X. Wang, G. Ausanio, and L. Lanotte. Laser-induced modification of the size distribution of nanoparticles produced during ultrashort laser ablation of solid targets in vacuum. *Journal of Physics B: Atomic, Molecular and Optical Physics*, 40(6):1253–1258, 2007.

[36] B. N. Chichkov, C. Momma, S. Nolte, F. von Alvensleben, and A. Tunnermann. Femtosecond, picosecond and nanosecond laser ablation of solids. *Applied Physics A: Materials Science & Processing*, 63(2):109–115, 1996.

[37] Annemie Bogaerts and Zhaoyang Chen. Effect of laser parameters on laser ablation and laser-induced plasma formation: A numerical modeling investigation. *Spectrochimica Acta - Part B Atomic Spectroscopy*, 60(9-10):1280–1307, 2005.

[38] John E Sinko and Claude R Phipps. Modeling CO2 laser ablation impulse of polymers in vapor and plasma regimes. *Applied Physics Letters*, 95(13):131105, 2009.

[39] S Amoruso, R Bruzzese, N Spinelli, and R Velotta. Characterization of laser-ablation plasmas. *Journal of Physics B: Atomic, Molecular and Optical Physics*, 32(14):R131, 1999.

[40] C Phipps. Micropropulsion using a laser ablation jet. *Journal of Propulsion and Power*, 20(6), 2004.

[41] Claude R. Phipps, James R. Luke, and Wesley D Helgeson. 3ks specific impulse with a ns-pulse laser microthruster. *Proceedings of the International Electric Propulsion Conference 2005 (IEPC05)*, 298(0704):1–10, 2005.

[42] Claude R. Phipps, James R. Luke, Wesley D Helgeson, and Richard Johnson. Performance test results for the laser-powered microthruster. *AIP Conference Proceedings*, 830:224–234, 2006.

[43] Tadaki Shinohara, Hideyuki Horisawa, Msahumi Baba, and Kazuyoku Tei. A pulsed laser-electromagnetic hybrid accelerator for space propulsion application. In *AIP Conference Proceedings*, pages 338–348, 2010.

[44] Hideyuki Horisawa, Yuki Mashima, and Osamu Yamada. Acceleration mechanism of pulsed laser-electromagnetic hybrid thruster. *AIP Conference Proceedings*, 1402:391–401, 2011.

[45] Eric S. Smith, Raymond J. Sedwick, John F. Merk, and Justin McClellan. Assessing the potential of a laser-ablation-propelled tug to remove large space debris. *Journal of Spacecraft and Rockets*, 50(6):1268–1276, 2013.

[46] Akihiro Sasoh, Shingo Suzuki, and Atsushi Matsuda. Wall-propelled, in-tube propulsion with repetitive-pulse laser ablation. *Journal of Propulsion and Power*, 25(2):540–542, 2009.

[47] Ten-see Wang, Yen-Sen Chen, Jiwen Liu, Leik N. Myrabo, and Franklin B. Mead Jr. Advanced performance modeling of experimental laser lightcraft. *Journal of Propulsion and Power*, 18(6), 2002.

[48] Sean D. Knecht, Franklin B. Mead Jr., Michael M. Micci, and C. William Larson. Trajectory simulations, qualitative analyses and parametric studies of a laser-launched micro-satellite using OTIS. *AIP Conference Proceedings*, 830(0704):522–533, 2006.

[49] Jonathan W. Campbell. Project ORION: orbital debris removal using ground-based sensors and lasers. *Second European Conference on Space Debris*, 1997.

[50] Claude R. Phipps. A laser-optical system to re-enter or lower low Earth orbit space debris. *Acta Astronautica*, 93:418–429, 2014.

[51] Philip Lubin, Gary B. Hughes, Johanna Bible, Jesse Bublitz, Josh Arriola, Caio Motta, Jonathan Suen, Isabella Johansson, Jordan Riley, Nilou Sarvian, Deborah Clayton-Warwick, Jane Wu, Andrew Milich, Mitch Oleson, Mark Pryor, Peter Krogen, Miikka Kangas, and Hugh O'Neill. Directed energy planetary defense. *Optical Engineering*, 53(2), 2014.

[52] Philip Lubin. A roadmap to interstellar flight. *arXiv preprint arXiv:1604.01356*, 2016.

[53] James O McSpadden and John C Mankins. Space solar power programs and microwave wireless power transmission technology. *IEEE microwave magazine*, 3(4):46–57, 2002.

[54] Duncan Graham-Rowe. Solar-powered lasers. *Nature Photonics*, 4:64, feb 2010.

[55] H J Melosh, I V Nemchinov, and Yu. I Zetzer. Non-nuclear strategies for deflecting comets and asteroids, 1994.

[56] Massimo Vetrisano, Jo?o Branco, Joan Pau Sanchez Cuartielles, Daniel Garci Yarnoz, and Massimiliano L Vasile. Deflecting small asteroids using laser ablation: Deep space navigation and asteroid orbit control for LightTouch2 mission. In *AIAA Guidance, Navigation, and Control (GNC) Conference*, Guidance, Navigation, and Control and Co-located Conferences. American Institute of Aeronautics and Astronautics, aug 2013.

[57] Jonathan W. Campbell. *Using Lasers in Space*. DIANE Publishing, 2000.

[58] Alison Gibbings, John-Mark Hopkins, David Burns, and Massimiliano Vasile. On testing laser ablation processes for asteroid deflection. *Planetary Defense Conference*, 2011.

[59] Alison Lorraine Gibbings. *Laser ablation for the deflection, exploration and exploitation of Near Earth Asteroids*. PhD thesis, University of Glasgow, 2013.

[60] Travis Brashears, Philip Lubin, Gary B. Hughes, Peter Meinhold, Jonathan Suen, Payton Batliner, Caio Motta, Janelle Griswold, Miikka Kangas, Isabella Johansson, Yusuf Alnawakhtha, Alex Lang, and Jonathan Madajian. Directed Energy Deflection Laboratory Measurements. In *Nanophotonics and Macrophotonics for Space Environments IX*, 2015.

[61] Chris J Bennett, Claire Pirim, and Thomas M Orlando. Space-weathering of solar system bodies: A laboratory perspective. *Chemical reviews*, 113(12):9086–9150, 2013.

[62] Thomas Gold. The lunar surface. *Monthly Notices of the Royal Astronomical Society*, 115:585–604, 1956.

[63] Bruce Hapke. Darkening of silicate rock powders by solar wind sputtering. *The Moon*, 7(April):342–355, 1973.

[64] Bruce Hapke. Space weathering from Mercury to the asteroid belt. *Journal of Geophysical Research: Planets*, 106:10039–10073, 2001.

[65] G G Managadze, V T Cherepin, Y G Shkuratov, V N Kolesnik, and A E Chumikov. Simulating OH/H2O formation by solar wind at the lunar surface. *Icarus*, 215(1):449–451, 2011.

[66] M J Loeffler, R A Baragiola, and M Murayama. Laboratory simulations of redeposition of impact ejecta on mineral surfaces. *Icarus*, 196:285–292, 2008.

[67] Jan Filip, Daniel Britt, Todd Bradley, Roman Skála, Tomáš Kohout, and C Jan. Space weathering simulations through controlled growth of iron nanoparticles on olivine. *Icarus*, 237:75–83, 2014.

[68] Maho Yamada, Sho Sasaki, Hiroko Nagahara, Akira Fujiwara, Sunao Hasegawa, and Hajime Yano. Simulation of space weathering of planet-forming materials: Nanosecond pulse laser irradiation and proton implantation on olivine and pyroxene samples. *Earth, planets and space*, 51:1255–1265, 1999.

[69] R Brunetto, F Romano, A Blanco, S Fonti, M Martino, V Orofino, and C Verrienti. Space weathering of silicates simulated by nanosecond pulse UV excimer laser. *Icarus*, 180(2):546–554, 2006.

[70] Laurence Lemelle, Luc Beaunier, Stephan Borensztajn, Michel Fialin, and François Guyot. Destabilization of olivine by 30-keV electron irradiation : A possible mechanism of space weathering affecting interplanetary dust particles and planetary surfaces. *Geochimica et cosmochimica acta*, 67(10):1901–1910, 2003.

[71] D L Simms. Archimedes and the burning mirrors of Syracuse. *Technology and Culture*, 18(1):1–24, 1977.

[72] Naval Surface Warfare Center Dahlgren Div VA. Directed energy: Applications across land, air, and sea. *Leading Edge*, 7(4), 2012.

[73] William J Broad. Nuclear Pulse (I): Awakening to the Chaos Factor. *Science*, 212(4498):1009–1012, 1981.

[74] David Smalley. Historic leap: Navy shipboard laser operates in Arabian Gulf. https://www.navy.mil/submit/display.asp?story_id=84805, 2014.

[75] GlobalSecurity.org. Space Based Laser. https://www.globalsecurity.org/space/systems/sbl-components.htm, 2011.

[76] Brad Lendon. Navy: New laser weapon works, ready for action. https://www.cnn.com/2014/12/11/tech/innovation/navy-laser-weapon, 2014.

[77] James Laporta. Navy orders laser weapon systems from Lockheed Martin. http://www.spacedaily.com/reports/Navy_orders_laser_weapon_systems_from_Lockheed_Martin_999.html, 2018.

[78] Ulrich Boesl. Time-of-flight mass spectrometry: introduction to the basics. *Mass spectrometry reviews*, 36(1):86–109, 2017.

[79] M Guilhaus, D Selby, and V Mlynski. Orthogonal acceleration time-of-flight mass spectrometry. *Mass spectrometry reviews*, 19(2):65–107, 2000.

[80] N R Daly. Scintillation type mass spectrometer ion detector. *Review of Scientific Instruments*, 31(3):264–267, 1960.

[81] William B Brinckerhoff, G G Managadze, Richard Mcentire, and Andrew Cheng. Laser time-of-flight mass spectrometry for space. *Review of Scientific Instruments*, 71(March):536–545, 2000.

[82] S. Amoruso, G. Ausanio, A C Barone, R. Bruzzese, L. Gragnaniello, M. Vitiello, and X. Wang. Ultrashort laser ablation of solid matter in vacuum: a comparison between the picosecond and femtosecond regimes. *Journal of Physics B: Atomic, Molecular and Optical Physics*, 38(20):L329–L338, 2005.

[83] Kohei Anju, Keisuke Sawada, Akihiro Sasoh, Koichi Mori, and Eugene Zaretsky. Time-Resolved Measurements of Impulse Generation in Pulsed Laser-Ablative Propulsion. *Journal of Propulsion and Power*, 24(2):322–329, 2008.

[84] Andrew V. Pakhomov, M. Shane Thompson, W. Swift, and Don A Gregory. Ablative laser propulsion - Specific impulse and thrust derived from force measurements. *AIAA Journal*, 40(11):2305–2311, 2002.

[85] James E. Polk, Anthony Pancotti, Thomas Haag, Scott King, Mitchell Walker, Joseph Blakely, and John Ziemer. Recommended practice for thrust measurement in electric propulsion testing. *Journal of Propulsion and Power*, 33(3):539–555, 2017.

[86] Claude R. Phipps and James R. Luke. Diode laser-driven microthrusters: A new departure for micropropulsion. *AIAA Journal*, 40(2):310–318, 2002.

[87] Don Pettit. The tyranny of the rocket equation. http://www.nasa.gov/mission_pages/station/expeditions/expedition30/tryanny.html, 2012.

[88] Jarred A Young and Raymond J Sedwick. High Energy Plume Impingement on Spacecraft Systems. *52nd Aerospace Sciences Meeting*, pages 1–10, 2014.

[89] Andrew V. Pakhomov, Don A Gregory, and Michael Shane Thompson. Specific impulse and other characteristics of elementary propellants for ablative laser propulsion. *AIAA Journal*, 40(5):947–952, 2002.

[90] Catherine E Miller and Paulo C Lozano. The effects of metastable solvated ions on electrospray ion thruster efficiency. *34th International Electric Propulsion Conference*, pages 1–14, 2015.

[91] a. W. Bailey, a. Modak, L. F. Curtiss, a. V. Astin, a. Brockhinke, P. Andresen, G. Grunefeld, and V. Beushausen. Numerical simulation of laser ablation with cavity reflections. *Journal of Thermophysics and Heat Transfer*, 3(1):42–45, 1989.

[92] M. Guilhaus. Principles and instrumentation in time-of-flight mass spectrometry: Physical and instrumental concepts. *Journal of Mass Spectrometry*, 30(11):1519–1532, 1995.

[93] Von Richard Herzog. Ionen-und elektronenoptische Zylinderlinsen und Prismen. I. *Zeitschrift Physik*, 89:447–473, 1934.

[94] Helmut Liebl. *Applied charged particle optics*. Springer, 2008.

[95] H Wollnik and H Ewald. The influence of magnetic and electric fringing fields on the trajectories of charged particles. *Nuclear Instruments and Methods*, 36:93–104, 1965.

[96] Catherine Miller. *On the stability of complex ions in ionic liquid ion sources*. Master of science, Massachusetts Institute of Technology, 2015.

[97] Paulo Lozano and Manuel Martínez-Sánchez. Ionic liquid ion sources: Characterization of externally wetted emitters. *Journal of Colloid and Interface Science*, 282(2):415–421, 2005.

[98] Joshua Sloane, Eric Smith, and Raymond Sedwick. Validation of a time-of-flight mass spectrometer using an ionic liquid ion source. *International Journal of Mass Spectrometry*, 432:36–43, 2018.

[99] R A Ganeev, U Chakravarty, P A Naik, H Srivastava, C Mukherjee, M K Tiwari, R V Nandedkar, and P D Gupta. Pulsed laser deposition of metal films and nanoparticles in vacuum using subnanosecond laser pulses. *Appl. Opt.*, 46(8):1205–1210, mar 2007.

[100] N Batina, J C Alonso, R Diamant, P Castillo, and M C Acosta Garcı. Applied surface science thin films of silver nanoparticles deposited in vacuum by pulsed laser ablation using a YAG:Nd laser. *Applied Surface Science*, 255:4933–4937, 2009.

[101] Manuel J Manard. A design for a compact time-of-flight mass spectrometer. *The Review of scientific instruments*, 83(10):105111, 2012.

[102] Md Haider A. Shaim and Hani E. Elsayed-Ali. Characterization of laser-generated aluminum plasma using ion time-of-flight and optical emission spectroscopy. *Journal of Applied Physics*, 122(20), 2017.

[103] Claude R. Phipps and Mike Lander. What's New for Laser Orbital Debris Removal. In *AIP Conference Proceedings-American Institute of Physics*, page 339, 2011.

[104] Alison Gibbings, Massimiliano Vasile, John-Mark Hopkins, David Burns, and Ian Watson. Potential of laser-induced ablation for future space applications. *Space Policy*, 28(3):149–153, 2012.

[105] K N Marsh, J A Boxall, and R Lichtenthaler. Room temperature ionic liquids and their mixtures—a review. *Fluid Phase Equilibria*, 219(1):93–98, 2004.

[106] S W Miller, B D Prince, and R J Bemish. Orthogonal time-of-flight mass spectrometry of an ion beam with a broad kinetic energy profile. *Review of Scientific Instruments*, 88(10):105111, 2017.

[107] W D Luedtke, Uzi Landman, Y-H Chiu, D J Levandier, R A Dressler, S Sok, and Mark S Gordon. Nanojets, electrospray, and ion field evaporation: molecular dynamics simulations and laboratory experiments. *The Journal of Physical Chemistry A*, 112(40):9628–9649, 2008.

[108] Geoffrey Taylor. Disintegration of water drops in an electric field. *Proceedings of the Royal Society of London. Series A. Mathematical and Physical Sciences*, 280(1382):383–397, 1964.

[109] Joshua Sloane, Eric Smith, and Raymond Sedwick. Time-of-flight mass spectrometry analysis of pulsed laser ablation of pyroxene. *AIP Advances*, 9:025019, 2019.

[110] Tricia Talbert. Five years after the Chelyabinsk meteor: NASA leads efforts in planetary defense. https://www.nasa.gov/feature/five-years-after-the-chelyabinsk-meteor-nasa-leads-efforts-in-planetary-defense, 2018.

[111] Brent W. Barbee and Wallace T Fowler. Spacecraft Mission Design for the Optimal Impulsive Deflection of Hazardous Near-Earth Objects (NEOs) using Nuclear Explosive Technology. *Planetary Defense Conference*, 2007.

[112] Nicolas Thiry and Massimiliano Vasile. Deflection of uncooperative targets using laser ablation. In *Proc. SPIE*, volume 9616, pages 96160X–96160X–16, 2015.

[113] R Z Sagdeev and A V Zakharov. A brief history of the expedition to Phobos. *Sov. Astron. Lett*, 16(2):125–128, 1990.

[114] Michael J Gaffey, Jeffrey F Bell, R.Hamilton Brown, Thomas H Burbine, Jennifer L Piatek, Kevin L Reed, and Damon A Chaky. Mineralogical Variations within the S-Type Asteroid Class. *Icarus*, 106(2):573–602, 1993.

[115] Eric Smith, Joshua Sloane, and Raymond Sedwick. A low complexity time-of-flight mass spectrometer with ion size measurement based on secondary particle yield. *International Journal of Mass Spectrometry*, 434:43–51, 2018.

[116] I Konomi, T Motohiro, and T Asaoka. Angular distribution of atoms ejected by laser ablation of different metals. *Journal of Applied Physics*, 106(1):13107, 2009.

[117] John W. Anthony, Richard A. Bideaux, Kenneth W. Bladh, and Monte C. Nichols. Augite. http://www.handbookofmineralogy.org/pdfs/augite.pdf, 2001.

[118] Claudio Bombardelli, Hodei Urrutxua, Mario Merino, Jesús Peláez, and Eduardo Ahedo. The ion beam shepherd: A new concept for asteroid deflection. *Acta Astronautica*, 90(1):98–102, 2013.

[119] Alison Gibbings, Massimiliano Vasile, Ian Watson, John-Mark Hopkins, and David Burns. Experimental analysis of laser ablated plumes for asteroid deflection and exploitation. *Acta Astronautica*, 90(1):85–97, 2013.

[120] Ricardo Torres and Margarita Martin. Laser ablation and time-of-flight mass-spectrometric study of SiO. *Applied Surface Science*, 193(1-4):149–155, 2002.

[121] L. Jiang and H. L. Tsai. Femtosecond Lasers Ablation : Challenges and Opportunities. *Aerospace Engineering*, 1(1):51–53, 2003.

[122] Claude R. Phipps. A ns-Pulse Laser Microthruster. *AIP Conference Proceedings*, 830:235–246, 2006.

[123] Hideyuki Horisawa, Sota Sumida, Hitoshi Yonamine, and Ikkoh Funaki. Thrust generation through low-power laser-metal interaction for space propulsion applications. *Vacuum*, 88(1):75–78, 2013.

[124] Brian C. D'Souza and Andrew D. Ketsdever. Direct Impulse Measurements of Ablation Processes from Laser-Surface Interactions. In *36th AIAA Plasmadynamics and Lasers Conference*, pages 1–9, Ontario Canada, 2005. AIAA.

[125] S. Preuss, A. Demchuk, and M. Stuke. Sub-picosecond UV laser ablation of metals. *Applied Physics A: Materials Science and Processing*, 61(1):33–37, 1995.

[126] Christian Schrader, Douglas Rickman, Carole McLemore, John Fikes, Douglas Stoeser, Susan Wentworth, and David McKay. Lunar regolith characterization for simulant design and evaluation using figure of merit algorithms. In *47th AIAA Aerospace Sciences Meeting including The New Horizons Forum and Aerospace Exposition*, page 755, 2009.

[127] P T Metzger, D T Britt, K M Cannon, C D Schultz, Z Landsman, M Peppin, and S D Covey. Measuring the Fidelity of Asteroid Regolith Simulants. In *49th Lunar and Planetary Science Conference*, Houston, 2018. Lunar and Planetary Institute.

[128] Center for Lunar & Asteroid Surface Science. Planetary Simulant Database. http://sciences.ucf.edu/class/planetary-simulant-database/, 2018.

[129] Massimiliano Vasile and Christie Alisa Maddock. Design of a formation of solar pumped lasers for asteroid deflection. *Advances in Space Research*, 50(7):891–905, 2012.

[130] Kevin D Diamant, Ty Lee, Ray Liang, Jonathan Noland, Vanessa Vial, and Nicolas Cornu. Performance and Plume Characterization of the PPS 1350-G Hall Thruster. In *52nd AIAA/SAE/ASEE Joint Propulsion Conference*, AIAA Propulsion and Energy Forum. American Institute of Aeronautics and Astronautics, jul 2016.

[131] Federico Zuiani, Massimiliano Vasile, and Alison Gibbings. Evidence-based robust design of deflection actions for near Earth objects. *Celestial Mechanics and Dynamical Astronomy*, 114(1-2):107–136, 2012.

[132] NASA. Dawn at Ceres (Press Kit). Technical report, NASA, 2015.

[133] NASA. International Space Station - About the Space Station Solar Arrays. https://www.nasa.gov/mission_pages/station/structure/elements/solar_arrays-about.html, 2017.

[134] Rao Surampudi, Julian Blosiu, Paul Stella, John Elliott, Julie Castillo, Thomas Yi, John Lynos, Mike Piszczor, Jeremiah McNatt, Chuck Taylor, Ed Gaddy, Simon Liu, Ed Plichta, Christopher Iannello, Patricia M. Beauchamp, and James A. Cutts. Solar power technologies for future planetary science missions (JPL D-101316). Technical report, NASA, 2017.